Università degli Studi di Catania

Dottorato di Ricerca in Fisica
XXIV Ciclo

Antonio Massimiliano Mio

Crystallization of Amorphous Chalcogenide Nano-Regions and Test-Structure Fabrication for Non-Volatile Memories

Tutor:	Prof. E. Rimini Prof.ssa M.G. Grimaldi
Supervisor:	Dr. Giuseppe D'Arrigo

Coordinatore: Prof. F. Riggi

Tesi per il conseguimento del titolo

Crystallization of Amorphous Chalcogenide Nano-Regions and
Test-Structure Fabrication for Non-Volatile Memories
Antonio Massimiliano Mio
Ph. D. Thesis – Università degli Studi di Catania
Printed in Catania, December 2011

to my family

Contents

Introduction

The modern semiconductor technology, following the road map based on the Moore's law, has pushed CMOS-based electronic devices towards smaller and smaller dimensions, until reaching the 22nm node, indicating the minimum half distance between two devices in a chip. The scaling of the device dimension has increased the system functionality (e.g., more GBytes for memories or higher clock velocity for CPUs) that can be delivered in the same size package. Actually these improvements are both a byproduct of, and the driving force for, the relentless march to smaller device dimensions predicted by Moore [1].

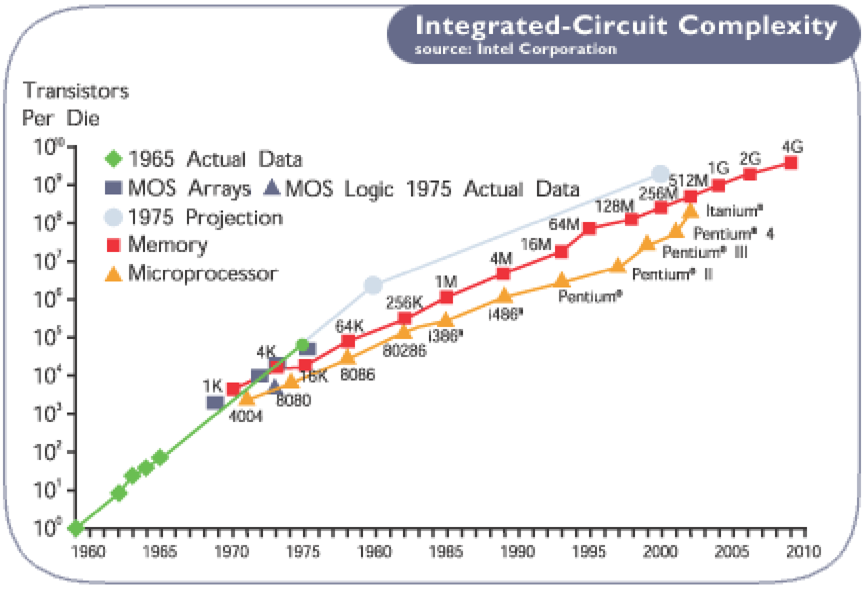

Figure 1 Moore's Law. The chart tracks the progress of transistor integration, for Intel's devices, from 1960 to 2010.

The history of the semiconductor industry has been dominated by this concept: higher densities at similar cost lead to more functionality, and thus more applications, which then spur investment for the additional research and development needed to implement the next size smaller device. Throughout this extensive history, extrapolation from the recent past has proven to be amazingly reliable for predicting near future developments.

In almost 60 years this history has been correlated to that of silicon, that has shown its predominant characteristics with respect to the other semiconductors, in terms of intrinsic features, integration with other materials, manipulation of its properties and scalability. From the beginning of silicon-based electronics, with the progression described by Moore, lithographic technological progress has permitted to decrease the typical feature size of order of magnitudes, from hundreds of microns to tens of nanometers. Nevertheless, this huge difference in dimension has not implied severe change in device layouts but essentially their rescaling, because the more relevant semiconductor properties are independent of the size until the submicron scale. Moreover, this is the main reason why, in the past century, the study of the material properties has been mainly addressed towards the bulk characteristics of the material itself, without particular concerning to its dimension.

However, as the dimension of the device becomes smaller than 22nm, the extrapolation of the properties obtained by the experimental data on bulk materials to nanosize structures, and then simple rescaling of the device layouts, is not, a priori, a correct procedure. As the size gets smaller the system is affected by several effects. First, the large extension of the crystal and its periodicity fall and so the Block theorem and the band model are not still valid to describe the system. Quantum size effects take place and discrete levels appear in the crystalline momentum corresponding to the shrunk directions. If the energy level distances are of the order or greater than kT, electrical and optical properties suffer this new state arrangement. Level distances and shift depend on the chemical characteristics of the crystal and on the strength of Coulomb interaction between almost free-electrons in the crystal and atomic potential.

In semiconductor, for instance, these effects are rather relevant with respect to the metals. Increasing the system size of a generic crystal, in fact, the number of levels increases at first in the center of the band and then at the edge.

As a consequence, in metals, where the Fermi level lies in the middle of a band, the relevant energy level spacing is still very small even in relatively small sizes (tens or hundreds of atoms) [2-4]. At temperatures above a few kelvin, the electrical and optical properties, therefore, more closely resemble those of a continuum. In semiconductors, instead, the Fermi level lies between two bands, so that the edges of the bands dominate the low-energy optical and electrical behavior.

Many works have demonstrated, both theoretically and experimentally, the relevance of the quantum size effects. Moreover, recent studies also take into account further properties emerging with scaling as absence of electron scattering in the so called mesoscopic-ballistic regime. Furthermore, while in the bulk materials transport is quite insensitive to the amount of carriers in the system, in nano structures, Coulomb Blockade shifts the energy levels as electrons are stored. These effects modify the behavior of the elemental components in a chip, requiring, at least, a further investigation about their global behavior in a combined layout.

Together with the scaling problem intrinsic of the shrinking of the silicon structures and then with the radical change in its electro-optical properties, other relevant problems regards the insulators involved in the CMOS (Complementary Metal Oxide Semiconductor) operation, especially memories. With scaling, in fact, the amount of electrons stored in the floating gate in a Flash memory reduces, until the signal to noise ratio becomes too small. Nevertheless, stress-induced leakage current (SILC) can occur across ultra-thin oxides CMOS-based memories by programming it with large voltages. Also one must to maintain coupling between the control and floating gates and to avoid the cell-to-cell parasitic interference between the stored charge in closely-packed cells[5-7].

The huge storage capacity the market requires could be provided by Silicon-based Multi-Level Cells (MLC), associating to the same cell different analogical states. However, since performance of MLC is worse than Single-Level Cell by means of programming speed, data retention and endurance, prototypal memories have not been commercialized in Flash-based SSD [8]. For these reasons, new kinds of memories, satisfying at the same time programming performance, endurance and, overall, scaling capability must be found.

New Non Volatile Memories (NVMs) candidate technologies are, at now, under consideration to substitute Flash Memories. Basically, there are two different kinds of approach. The first one consists of building memories that have a very simple integration with the consolidate CMOS technology; this is the case of ferroelectric and magnetic RAM. The other approach is to consider a completely new concept as in the case of racetrack memory and organic RAM. However, in the latest case, the research is still at beginning, mainly consisted by proofs of concept. Another class of memory considers something in-between with respect to these two concepts and this is the case of Phase Change Memories (PCM), resistance RAM, and solid-electrolyte memories [9].

Naturally, together with the performance requirements, they also need to be scalable for more than a decade, to justify the investments needed to develop a new technology.

Fortunately, Phase Change Random Access Memories (PCRAMs), in which the information bit is associated to the different resistivity of amorphous and crystalline phases, offer very good scalability perspective, both from preliminary studies on ultra-thin films (few nanometers) and from sub-lithographic prototypal devices. Good performance devices have been, in fact, recently demonstrated with a cross-section as small as 113 nm^2 [10] in isolated cell of about 3400 nm^3.

However, although many long terms issues have been predicted and solved, some others need a deeper research study, such as MLC with 4 bits per cell or the reduction of the RESET current, that represents the higher current experienced by a PCRAM, for technology node beyond 28nm (Figure 2).

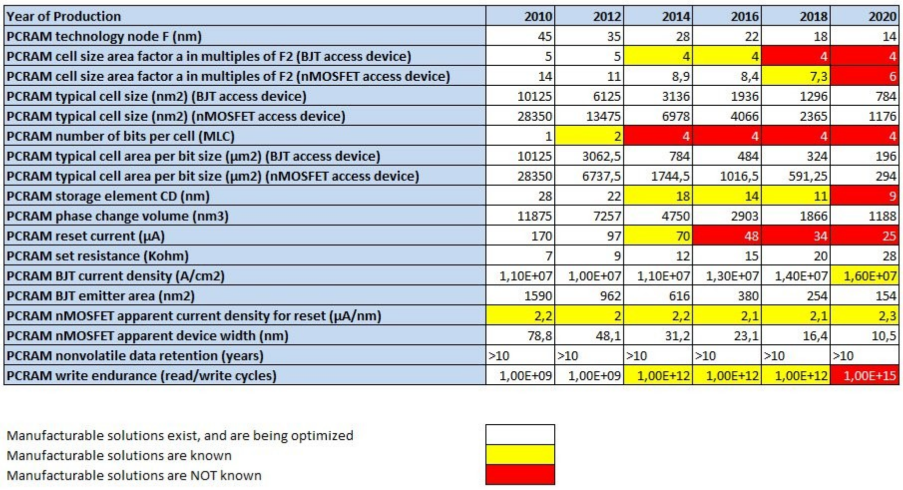

Year of Production	2010	2012	2014	2016	2018	2020
PCRAM technology node F (nm)	45	35	28	22	18	14
PCRAM cell size area factor a in multiples of F2 (BJT access device)	5	5	4	4	4	4
PCRAM cell size area factor a in multiples of F2 (nMOSFET access device)	14	11	8,9	8,4	7,3	6
PCRAM typical cell size (nm2) (BJT access device)	10125	6125	3136	1936	1296	784
PCRAM typical cell size (nm2) (nMOSFET access device)	28350	13475	6978	4066	2365	1176
PCRAM number of bits per cell (MLC)	1	2	4	4	4	4
PCRAM typical cell area per bit size (µm2) (BJT access device)	10125	3062,5	784	484	324	196
PCRAM typical cell area per bit size (µm2) (nMOSFET access device)	28350	6737,5	1744,5	1016,5	591,25	294
PCRAM storage element CD (nm)	28	22	18	14	11	9
PCRAM phase change volume (nm3)	11875	7257	4750	2903	1866	1188
PCRAM reset current (µA)	170	97	70	48	34	25
PCRAM set resistance (Kohm)	7	9	12	15	20	28
PCRAM BJT current density (A/cm2)	1,10E+07	1,00E+07	1,10E+07	1,30E+07	1,40E+07	1,60E+07
PCRAM BJT emitter area (nm2)	1590	962	616	380	254	154
PCRAM nMOSFET apparent current density for reset (µA/nm)	2,2	2	2,2	2,1	2,1	2,3
PCRAM nMOSFET apparent device width (nm)	78,8	48,1	31,2	23,1	16,4	10,5
PCRAM nonvolatile data retention (years)	>10	>10	>10	>10	>10	>10
PCRAM write endurance (read/write cycles)	1,00E+09	1,00E+09	1,00E+12	1,00E+12	1,00E+12	1,00E+15

Manufacturable solutions exist, and are being optimized ⬜
Manufacturable solutions are known 🟨
Manufacturable solutions are NOT known 🟥

Figure 2 PCRAM present and future requirements, as defined by the International Roadmap for Semiconductor 2010 [11]. According to the severity of the improvement a white, yellow or red box is used in correspondance of the proposed value.

The information bit, in these memories, is associated to the resistance of the crystalline and of the amorphous phases. In fact, a huge difference in resistivity (until to 6 order of magnitudes) between them occurs for chalcogenide. The material can easily be switched between these two state by current pulses of few hundreds µA with typical widths ranging from 10 to 100 ns.

Since their features strictly depends on the retention of the metastable disordered phase and on its characteristics, many studies have been conducted in amorphous thin films to investigate the crystallization kinetics [12-14].

However, as the dimension of the amorphous region gets smaller, the crystallization process, produced by the nucleation of crystalline grains followed by their growth, slows down since statistical occurrence of nucleation events drastically decreases. In addition, extrapolation of blanket properties data fails for different reasons. First, nucleation in chalcogenides is heavily influenced by surface, being in most cases heterogeneous. Second, amorphous active regions in devices are often surrounded by crystalline phase, reducing their stability, since no nucleation occurrence is required to start crystallization. Finally, amorphous formation, arising in device, comes with a great change in density (about the 6%) producing local stress in the memory cells. This compressive stress probably reduces the crystallization kinetics [15-16].

For these reasons, amorphous behavior in PCM must be studied in nano systems, in a closely condition with respect to the device active region.

Phase Change Material characteristics

As previously noted, market requires memory devices of smaller and smaller sizes. However, together with this main requisite, different prerequisites must be also satisfied. These prerequisite can be summarized in speed, SET-RESET contrast, endurance, ciclability and data retention. Assume a SLC system in which a memory element switches its state between only two possible levels: a reset state, also indicated by “0”, to a set state “1” and viceversa. Speed regards the velocity of switching between these two states; SET-RESET contrast concerns the difference between the read physical values in the two states: as large is this difference as fast it is possible to readout information upon the noise; endurance and ciclability regard how this difference is maintained with time/operations and how many set/reset cycles a cell can sustain before it fails; finally data retention concerns how much time bit information is maintained at a given temperature.

The way in which Phase Change Random Access Memories (PCRAMs) satisfy these requirements, strictly depends on the working principles they operate. Basically, the working principle of these devices is based on the substantial difference between the electrical properties of the amorphous and crystalline phases. Crystalline phase is a high conductivity state while the viceversa occurs in the amorphous state. Moreover, since these two phases present a relevant difference in reflectivity, chalcogenide are also largely used for high-density data storage in optical media (CD-RW, DVD-RAM, DVD-RW, Blu-ray Discs). The reflectivity contrast between these two states is about 30%, while the resistivity difference can reach up to six orders of magnitude (for instance in GeTe). Since these two conditions can be clearly distinguished (by a low power laser pulse for reflectivity or by a low power current pulse for resistivity) one can associate straightforwardly a bit information to it.

In Figure 3, time resolved measurements of sheet resistance and reflectivity have been reported for an amorphous GeTe film during its crystallization by *in situ* annealing at 167°C.

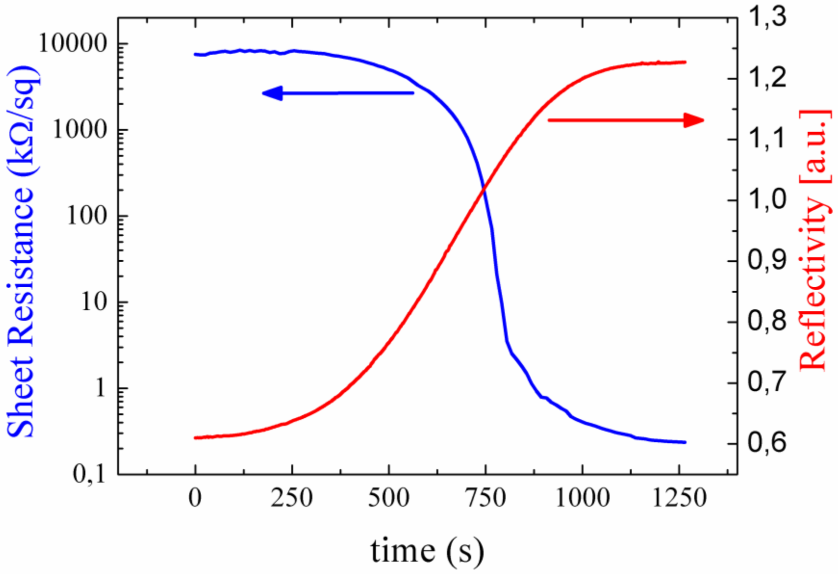

Figure 3 Time resolved measurements of sheet resistance and reflectivity for an as sputtered amorphous GeTe film (40 nm thick) during *in situ* annealing at 167°C. By crystallization the film resistivity decreases of several order of magnitudes and the reflectivity significantly enhances.

In Figure 4, the key points of phase change memory operation are summarized. Conventionally, the crystalline phase is related to the SET state and with SET operation we mean the process by which an amorphous bit of memory is transformed in a crystalline one. The viceversa occurs for RESET state and the involved RESET operation. In the optical recording system, reversible phase changes between crystalline and amorphous phase are achieved by short laser pulses with duration of tens of nanoseconds: the material is brought above the melting temperature and then, rapidly quenched by the surrounding environment (10^9 K/s).

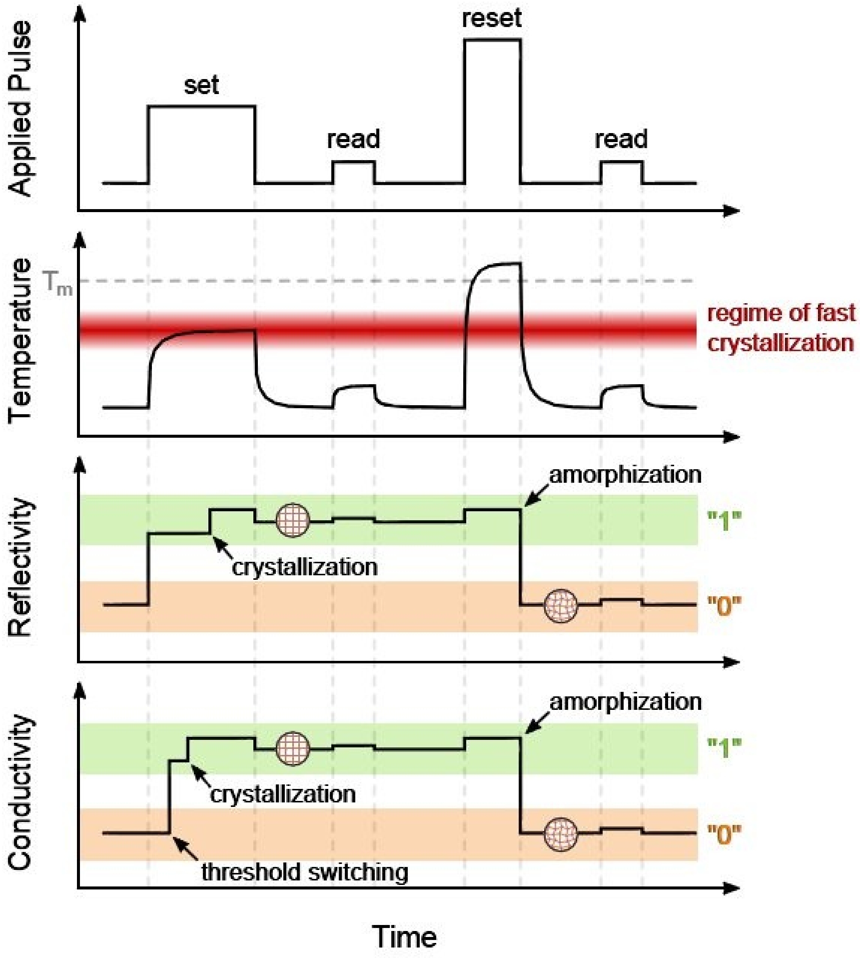

Figure 4 Operation involving phase change memories [17]. To set a device into the crystalline set state indicated by "1" (green) a (laser or current) pulse heats the system bringing it in the regime of fast crystallization (red). To reset the device, bringing it in the "0" amorphous state (orange), a pulse heats the system above the melting point. From the rapid quenching of the liquid, the system amorphizes. A low power pulse, small enough to

avoid material modification for the reset or set operation, is applied in order to read the reflectivity or the resistivity state.

The liquid phase, in this condition, has not enough time to rearrange in the crystalline phase and the liquid is frozen in the amorphous, disordered, phase. Current pulses of the same duration generate the phase switching in non-volatile electronic memories, following the same quenching mechanism. Crystallization occurs, instead, in solid phase by longer, less energetic, pulses since the transformation temperature is intermediate between those of glass formation and melting, in the so-called regime of fast crystallization. Hence, in the write and reset operations, the crystallization limits the operation frequency, usually about 10 MHz, and so the speed requirement.

The most frequently used chalcogenide alloy in NVM is certainly $Ge_2Sb_2Te_5$ (GST). Studies so far have shown that GST has one of the best combinations of electric and phase changing characteristics for PCRAM applications [18-20]. It is known that, in planar amorphous thin films, the phase transition of as-deposited amorphous Ge-Sb-Te alloys proceeds, during annealing, to the metastable face centered cubic (fcc) rock-salt phase (155°C) and to the stable hexagonal close packing (hcp) structure (350°C) by nucleation and growth of the different phases [13, 21, 22]. Figure 5 (a) and (b) indicates, respectively, these two crystalline phases. In particular, the rock-salt phase has been shown to be divided in two fcc sublattices. One fcc structure is occupied by Te atoms. The other fcc is randomly occupied by Ge and Sb atoms and vacancies (20% of the sublattice).

Chalcogenides, and in particular GST, represent a viable alternative to silicon in the non-volatile memory sector because they show good data retention, excellent switch velocity and miniaturization aptitude. The coexistence of these requirements is made possible by the particular amorphous structure they have, not so different to the crystalline state, that makes easier the switching between these two phases. Several models [23][24][25] have been proposed to describe this property. In particular, one pictorial phase-change mechanism, has been proposed by Kolobov et al. consisting of the so-called umbrella-flip in which Ge atoms change their symmetry from the amorphous tetrahedral configuration to the rocksalt-crystalline octahedral one (Figure 5c).

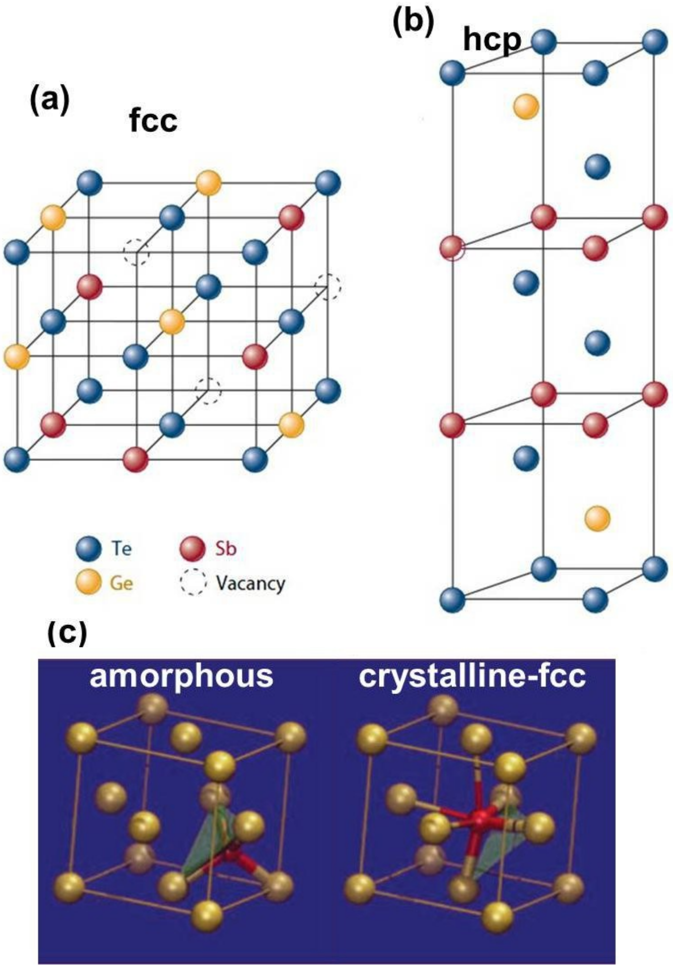

Figure 5 $Ge_2Sb_2Te_5$ in its crystalline phases: (a) fcc and (b) hcp [26]. In (c) it is shown a possible fcc-amorphous mechanism of transition, the umbrella flip, in which a Germanium atom (indicated in red) changes its symmetry from the amorphous tetrahedral configuration to the crystalline octahedral one [23].

Recently it has been pointed out [27], by ab-initio simulations and Raman spectroscopy, that amorphous phase in chalcogenides can be ascribed to a defective octahedra environment in which the crystalline sixfold coordination of Ge atoms in crystalline state is not fully established. By ab-initio simulations [25] it has been also shown the presence of a crucial structural motif of misaligned ABAB squares in amorphous GST (A=Ge,Sb for GST, and A=Ge for GeTe; and B=Te), which can straightforward rearrange to the crystalline configuration.

In spite of the straightforward mechanism involving phase transition in chalcogenide, amorphous structure must exhibit good stability (high data retention) connected to high glass temperature and, at the same time, low programming power (and current) connected to a low melting point. Matching these two requirements is not trivial: many research attempts in chalcogenide materials are focused to modify the alloy composition toward this direction [28]. On the other hand an important open quest in chalcogenides regards the crystallization thermodynamics and kinetics from the metastable amorphous phase, varying the dimension of the system. Another important subject in devices regards the presence of the crystalline phase around the active region of the devices that can compromise the amorphous stability. Almost all PCM layouts present this configuration, apart from some particularly prototypal device [10] in which the active region is isolated.

As sizes get smaller, the number of the surface atoms plays a relevant role with respect with the total number of atoms. In any material, surface atoms make a distinct contribution to the free energy, and the large changes in thermodynamic properties of nanocrystals (melting temperature decreasing , solid-solid phase transition temperature increasing) are commonly ascribed to the minor amount of bonds that atoms in the surface have.

Therefore, reducing the dimension we have a minor amount of bonds per atom we have to break for melting, thermodynamical stability of the structure is reduced and, as a consequence, melting point decreases.

However, the behavior of the crystallization temperature is not a-priori well-defined. Different results, according to the material and to its surrounding surfaces, have been obtained as its size decreases. For instance, for the GeSb alloy [29] the crystallization temperature increases in a blanket film as its thickness gets smaller in the range between 7.0 and 1.3 nm. It has been also fabricated, by Electron Beam Lithography, an array of 20-40 nm isolated nanopillar from a 50nm GeSb film, reducing in the nanometer scale all the dimensions. In this case, crystallization temperature slightly decreases (about 15°C) as the nanopillar size decrease (from 50nm to 20nm), indicating an opposite behavior. To our knowledge, similar experiments on GST have been performed only for thin films. The same authors also indicates an increasing of the crystallization temperature for the amorphous-fcc transition as the GST films get thinner in the 19.0 – 1.3 nm range, and in particular no rock-salt transition has been observed below 3.6 nm. No variation of crystalline temperature has been detected in the same thickness range for the transition to hexagonal, while, abruptly, no transition has been observed at 1.3 nm.

Wei et al. [30] also confirmed a similar behavior in the 20÷5 nm thickness range, proposing a model based on thickness dependent interfacial energy. When film thickness decreases the role of the crystalline grain in the interface becomes predominant. The increasing interfacial energy causes the nucleation barrier enhancement and thus crystallization temperature increases. The increasing of the glass temperature, decreasing the structure dimensions, offers optimistic expectation concerning the devices scalability, providing an important prediction about the improvement of the data retention performance. As a matter of fact, several kinds of PCRAM devices have been fabricated [31] in the last years with data retention better than 10 years at 100°C [34].

The properties of chalcogenide amorphous materials, however, not only concern system dimension. More generally, in fact, in a glass material, an infinite kinds of amorphous phases exist, depending on quenching rate, deposition method, amorphization technique [33, 34, 35] and each amorphous state reasonably presents a peculiar kinetics behavior.

In particular, we can consider three different kinds of amorphous structures: the as deposited, the melt-quenched and ion implanted ones. The first is produced by deposition method itself, usually by the (RF or DC) sputtering action of an Ar-based Plasma on a stoichiometric target. Although the target is usually crystalline, if the deposition temperature is maintained below the chalcogenide glass temperature, the resulting film will be amorphous. Melt-quenching is the mechanism aforementioned involving the optical and electronic memories and then it refers to an amorphous originated from a liquid phase. Finally, the third kind of amorphization can be accomplished by ion irradiation. Ion bombardment, in fact, at suitable energies (tens of keV) and fluencies ($\approx 10^{14}$ ions/cm^2) can displace atom in the host target to random positions, producing disorder. Each ion impinging in the chalcogenide produces a collision cascade with a typical radius of about 10 nm. According to the thermal and atomic diffusivity of chalcogenides, the collision cascades regarding ion bombardment in the material can be correlated with a local thermal spike annealing of about 10 ps [36] at temperatures very close to the melting point.

A full comprehension of the differences connected to these three kinds of amorphous phases is still missing and, nevertheless, necessary. Recent experiments [36, 37] and atomistic simulations [34] have been focused on the different crystallization behavior between them, pointing out difference in their local order arrangements. In particular, it has been shown that deposition process causes *wrong bonds* formation, i.e. homopolar bonds not allowed in the crystalline phase, acting as an obstacle during the crystallization.

As we will show in chapter 1, a reduction of the homopolar bonds (e.g. Te-Te bonds in GeTe), occurs during ion implantation or melt-quenching with respect to the deposited amorphous. As a consequence amorphous produced by melt-quenching and by low fluencies i.i. are similar in crystallization kinetics, as previously reported [37] by means reflectivity measurements, while slower crystallization rates has been observed in as deposited sputtered films.

PCM-based memories: main designs and electrical characterizations

Several kinds of PCM-based memory devices have been proposed and successfully fabricated. Among the different designs, however, the aim of the present work is to confine the heating profile of the region in which the active storage material of the cell resides, in order to bring it easily in the melting region or in the regime of fast crystallization (Figure 4). To obtain this result, memory cell must be addressed in proximity with the electrodes. The two principal cell archetypes are reported in Figure 6.

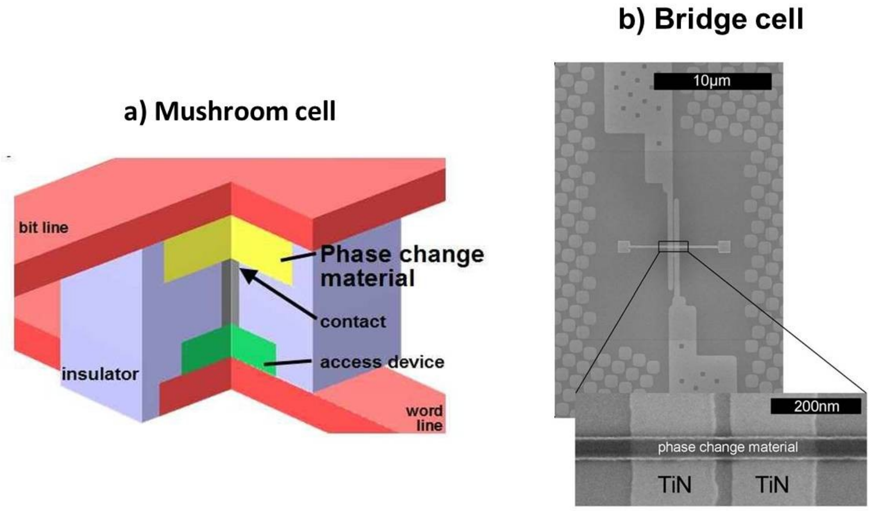

Figure 6 Phase-change device archetypes: (a) A typical contact-minimized cell, the mushroom cell, forces current to pass through a small contact formed by the intersection of one electrode and the phase change material [26]. (b) A typical bridge cell confines the active volume of the phase change material in a line between two TiN electrodes [38].

Figure 6a shows a mushroom cell. From a Bottom Electrode Contact (BEC) current is delivered towards the device through a tight via in order to increase current density and resistivity in the proximity of the metal-chalcogenide interface. Finally current reaches the Bit Line, that represents the Top Electrode Contact (TEC). Different materials can be used in the BEC in order to engineer the local resistivity and to enhance the Joule heating near the PCM. Generally, however, a Tungsten-based alloy is preferable, due to its high melting point (≈3700 K). Figure 6b illustrates a Scanning Electron Micrograph of a phase change bridge cell between two TiN electrodes. In this configuration, current is confined in the tight line (few tens of nanometers). The configuration in a) is preferred for the final industrial fabrication, because it can be easily inserted in high dense memory cell array. Configuration b), however, is more suitable to exploit the PCRAM behavior and characteristics, because of the easily access to the active region of the device (that is usually under a unique passivation film, instead of several layers) that permits morphological, structural and chemical analyses. Moreover, since one of the dimension involving the cross section in which current flows is the thickness, the bridge configuration allows scalability below the lithographical current node, permitting also predictions about future devices. Several works [39] are devoted to simulate the thermal profile, produced by Joule heating, in PCRAM during programming. Figure 7a shows the results obtained by Kim et al. referred to a mushroom cell during reset operation. Simulation assumes adiabatic and convection boundary conditions in the heat diffusion model. Over the BEC, temperature can reach the melting point of the chalcogenide material (about 916 K in $Ge_2Sb_2Te_5$). With rapid quenching (≈10 ns, with a cooling rate ≈10^9 K/s) an amorphous dome is produced, with the typical mushroom shape (Figure 7b). Again, Joule heating is responsible of the crystallization of the amorphous dome in the SET operations. However, while addressing a large amount of current is straightforward in a SET crystalline state, due to its low resistivity, in principle, we need large voltage values to obtain significant currents in an amorphous, high resistivity, state. The suitability of chalcogenide materials as electronic memory resides, instead, in their capability of changing their conductivity in the amorphous phase from an high resistivity to a conductivity state at a certain electrical field value. This mechanism, demonstrated by Ovshinsky in 1968, is called *threshold switching* [41].

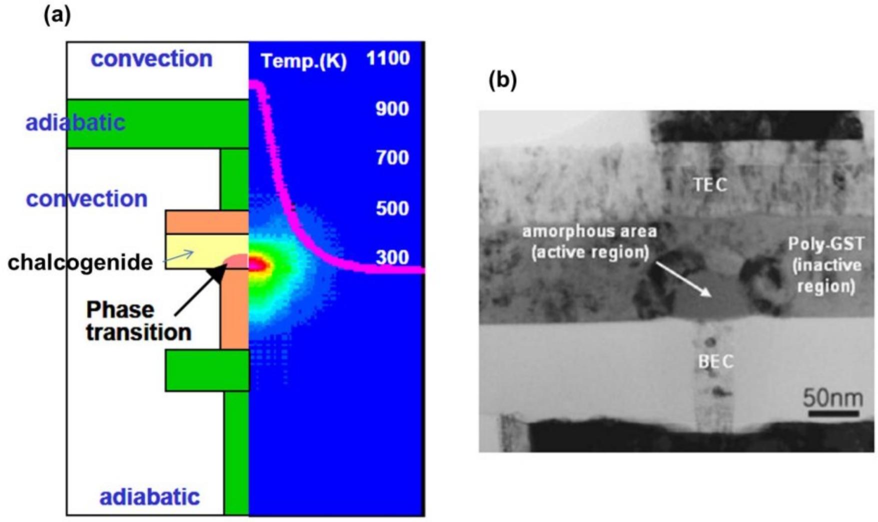

Figure 7 Simulation of the thermal profile [39] in a mushroom cell during RESET operation. Over the Bottom Electrode Contact (BEC) temperature overcomes the melting point and, from quenching, an amorphous dome is obtained (b) [40].

Peculiar I-V characteristics of a PCM cell can be obtained by voltage sweep up, typically from 0V to 2÷3 V, with ≈100ns long pulses. In Figure 8, this procedure is shown for a SET cell (full squares) and for a RESET cell (empty circles).

The SET state features a slight non-linear I-V (Figure 8) curve with a resistance varying between a low-field, low-current, regime (OFF state) and a high field, high-current, regime (ON state). For both these states the resistance measured during the pulse is usually in the KOhm range. The RESET state is characterized by a significant larger resistance in the low-field regime, usually in the range of few MOhm. However, the I-V curve suddenly changes at the threshold voltage (V_{th} in the figure) where the conductivity of the cell becomes comparable to that of the set state. This transition is known as threshold switching. Without the threshold switching mechanism, ≈10V should be applied to the PCM cell to deliver an amount of power suitable for cell crystallization. Such high voltage value would be incompatible with those operating in a CMOS addressing system.

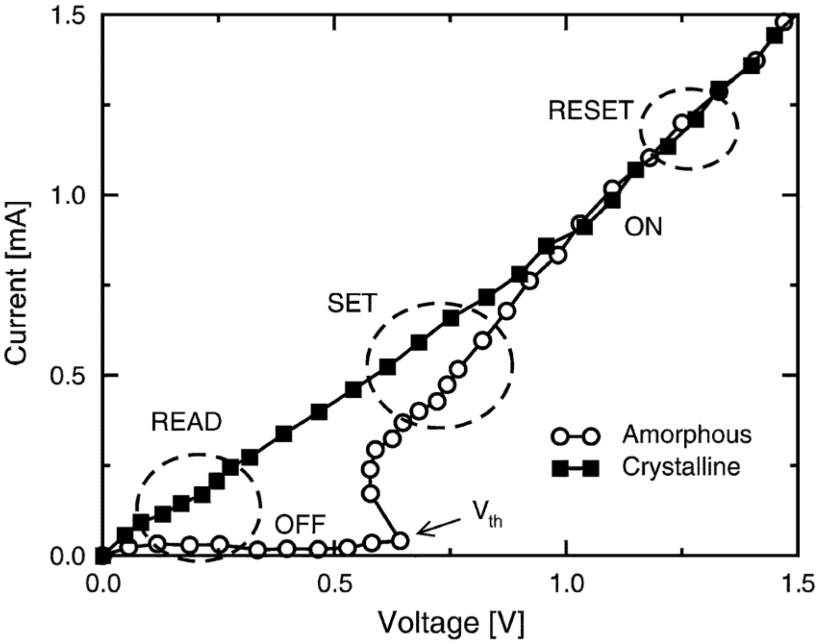

Figure 8 Experimental I–V curve of a mushroom cell with the GST in the crystalline and in the amorphous state. It is obtain by sweep up an amorphous (empty circles) or a crystalline (full squares) state. Threshold switching at V_{th} and relative snap back are clearly visible. Typical voltage regimes for reading (READ), setting (SET) and resetting (RESET) are also emphasized.

In spite of its importance, the origin of the threshold switching mechanism is still under debate. The conduction in the amorphous state has been ascribed to Poole-Frenkel (PF) transport in the presence of a high concentration of traps [42], according to the observed temperature dependence of the activation energy for conduction and to the behavior of the I-V characteristic. Conduction activation energy has been shown to be ≈0.3V in GST with respect to an energy gap of ≈0.7V in the amorphous phase. This is attributed to the Fermi level being pinned at about mid gap as a result of the huge concentration of traps due to the disordered structure.

Figure 9 reports an experimental I-V curves in semilog scale for mushroom cells, in an initial amorphous state, with different chalcogenide film thickness. In this representation it is straightforward to distinguish different regimes for the amorphous state characteristic.

For low voltage, the current is due to PF transport under equilibrium energy, i.e. a Fermi-Dirac distribution with Fermi Level E_F (Figure 10a), corresponding to a linear regime (Figure 9a). For higher electric fields, trapped electrons can gain a significant energy provided by the electric field. This can be modeled as a transition of electrons from low-energy to high-energy trap states (Figure 10b). In terms of electrons transport this corresponds to a large increase of the electron mobility, observable in the I-V characteristics with an exponential behavior (Figure 9b). However, electrons must overcome a finite distance to achieve, by electric field, the necessary energy to reach the destination trap state and, for over threshold voltages, it has been shown that an non uniform electric field is establish along the chalcogenide to sustain the continuous PF current (Figure 10c). Therefore, at the threshold switching, electric field is probably distributed in a high field equilibrium region (equ.) and in a low filed non-equilibrium region (nonequ.). In the first region electrons accumulate energy to hop in the adjacent low-field region in which shallow traps are then populated, bringing the system in a nonequilibrium regime. The total current above the threshold switching can be then successful modeled as the sum of the PF contribution by the deep and the shallow trap levels [42].

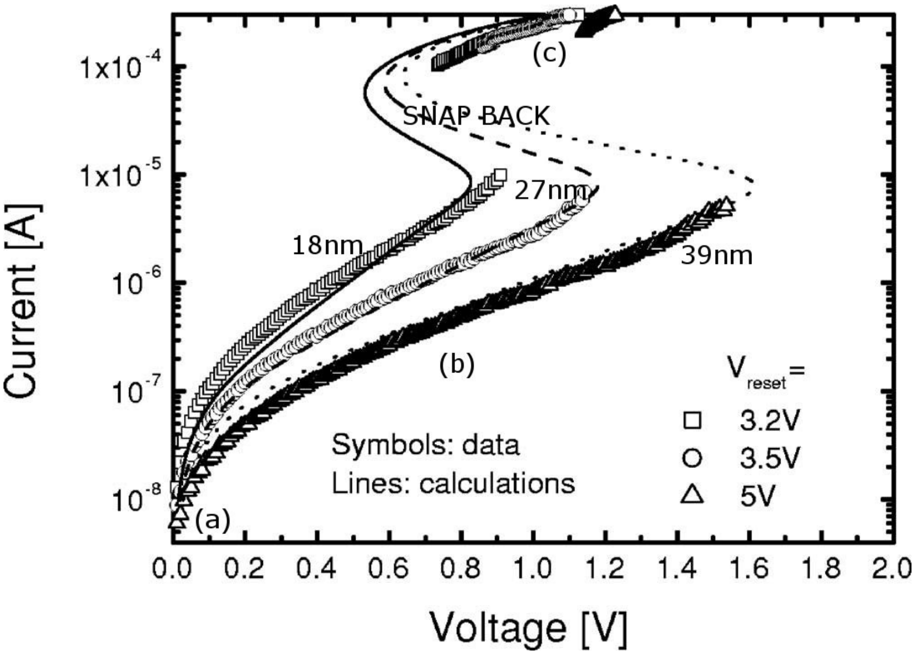

Figure 9 [42] An experimental I-V curve in semilog scale for mushroom cells, in an initial amorphous state, with different chalcogenide film thickness. It is clearly distinguished: (a) a low field linear regime, (b) an exponential sub-threshold regime and (c) a sudden current enhancement due to the threshold switching.

For the effect of the huge amount of electrons in the nonequilibrium region the field is notable lowered with respect to the equilibrium regime and, as a consequence, an evident voltage snap back is observable between these two regimes (Figure 9b-c).

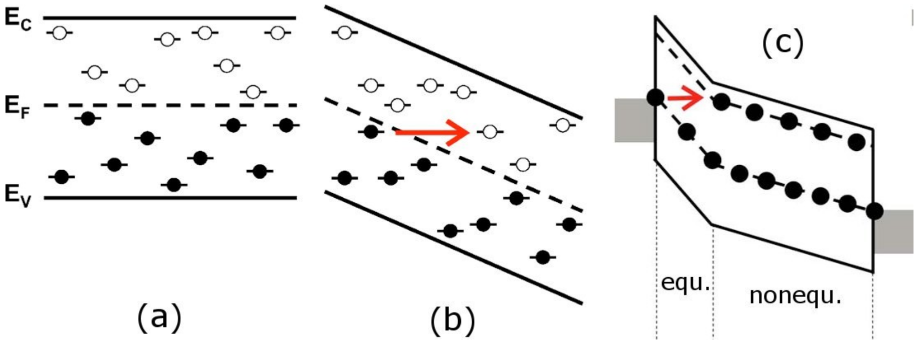

Figure 10 [42] Schematic of the carrier injection mechanism responsible for the threshold switching in chalcogenide. For low electric field, current is due to PF transport under equilibrium energy, i.e. a Fermi-Dirac distribution with Fermi Level $E_{F,}$ corresponding to a linear regime. At high field electrons can gain energy and occupy shallow traps, bringing the system in a linear regime. When a threshold field is overcome, equilibrium and non-equilibrium regions can coexist, promoting electron directly from the first regime to the shallow traps of the second one (c), suddenly lowering the total electric field required to sustain the high current.

Motivation

The aim of this thesis is to study the crystallization behavior of amorphous samples at different scales, pointing towards layouts similar to those ones occurring in PCM-based devices. To clarify the relevance of the amorphous local structures produced by ion implantation we detailed the crystallization kinetics of GeTe thin film. The crystallization of amorphous nanostructures of GST obtained by ion implantation, both isolated or embedded in its crystalline environment (fcc or hcp) has been analyzed and the results have been reported in chapter 2. Finally we have fabricated by Electron Beam Lithography (EBL) characterized (from a structural, morphological and electrical point of view) a real GST prototypal memory cell, with a line-concept layout.

In the first part of this thesis, we have analyzed the differences between as sputtered, melt-quenched and ion implanted amorphous structures in GeTe thin film by means of Raman Spectroscopy. Optical Microscopy and Time Resolved Reflectivity (TRR) were then used to investigate crystallization of the amorphous phases obtained by sputtering deposition and ion implantation.

GeTe crystalline grains have an optical contrast, with respect to the amorphous phase, of about 30%. They are also as big as tens of microns before coalescence, therefore, their nucleation and growth processes can be followed by means of optical microscopy. In addition, it is possible to protect by a metal hard mask a region of the sample performing ion implantation over this system. By this procedure it is, therefore, simple to create an ion implanted amorphous next to the unmasked, as sputtered, amorphous region. This technique permits, annealing the sample in the range of the glass temperature regime, to extrapolate the kinetic values and to compare the crystallization processes directly in the same *in situ* annealing observation.

In the second part, we analyze the data retention problem, studying the crystallization of amorphous nano region with size less than 20 nm embedded in a GST crystalline environment. This condition is very close to that one in which normally amorphous bits stay in devices. These nano regions have been fabricated by ion implantation in a nano mask produced by EBL. With aid of the results obtained in the first section, ion Implantation has been shown to be powerful tool to produce in a controlled and reproducible way amorphous region with characteristics comparable to the melt-quenched, distinctive of the PCM-based devices [35, 37, 43]. This technique permits to access to observations never performed since, for the complexity of a real device layout, is very difficult to investigate the active region of a Phase Change cell and, in fact, data retention studies in literature have been performed only with the aid of indirect electrical measurements [44-45]. Indirect measurements are based on the observation of the cell resistance or of the threshold voltage during isothermal annealing. Failure mechanism can occur in a statistical way on the memory cell array, due to nucleation inside an amorphous active region, or in a systematic one, due to the growth of the crystalline phase at expense of the amorphous one at the interfaces.

In the proposed system, selective ion implantation, combined with electron beam lithography, permits to access to minimum feature size well under the current technological node, 22nm. We will illustrate, in fact, that a minimum amorphous size of 10 nm can be achieved with this procedure. Amorphous stability is affected by the surrounding crystalline environment, since growth from the surrounding grains can start without any nucleation occurrence. This extremely small size condition, therefore, is very critical for the bit retention, because surface/volume ratio gets greater with decreasing the structure radius.

In the third part of this work, we present our prototypal device.

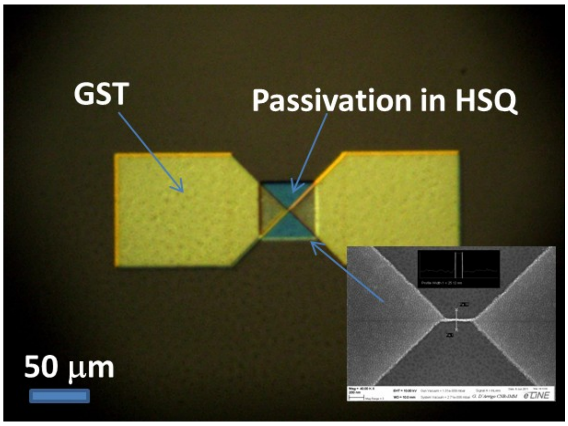

Figure 11 Optical image of the device we have fabricated in this thesis. The large GST square areas (l=100μm) work as pad for the electrical access to a shrunk line region (w=25nm, L=410nm, th=20nm), in the inset, that is the active memory part of the device. Over it, Hydrogen silsesquioxane (HSQ) is deposited for passivation.

Starting from a line layouts, previously reported in literature [46], we scaled the active region sizes, simplifying the steps required to process the device. In Figure 11 an optical image of the device is shown. The large GST square areas (l=100μm) work as pad for the electrical access to a shrunk line region (w=25nm, L=410nm, th=20nm). The inset of the figure shows a Scanning Electron Microscope (SEM) micrograph of this line region that is the active memory part of the device. Over it, Hydrogen silsesquioxane (HSQ) is deposited for passivation.

By suitable voltage pulses, 300ns long delivered by an HP81110A pulse generator, memory cell has been programmed. Also we have measured current and power during the pulse and we correlate them with the resistance of the cell, read in DC by a semiconductor analyzer.

The obtained well scalable structure is particularly suitable to study fundamental physics phenomena involved in the device working such as threshold switching, transitions, electromigration and doping. Electrical measurements on this test structures has been performed by Andrea Cattaneo at Politecnico di Milano.

Chapter 1

Nucleation and grain growth in as deposited and ion implanted GeTe thin films

The working principles of PCM-based devices strictly depend on the amorphous characteristics. However, in a glass material, an infinite variety of amorphous states take place, depending on quenching and on deposition.

In this chapter we have studied the crystallization dynamic of GeTe 50nm thick films, deposited on a SiO_2/Si substrate by RF magnetron sputtering, in its three different amorphous states: as deposited, ion implanted and melt-quenched.

Since ion implantation represents a powerful tool to create amorphous regions in a controlled and reproducible way, in the first part of the chapter we present an insight of this technique for blanket films.

In the second part, we present our results obtained by means of *in situ* time resolved reflectivity measurements (TRR) and optical microscopy during annealing in the 143-155°C temperatures range on as deposited and ion implanted amorphous samples. The data are compared using the Johnson Mehl Avrami Kolmogorov (JMAK) model.

Finally, a more comprehensive explanation of the kinetic results is presented by means of Raman Spectroscopy on the as deposited, ion implanted and melt-quenched amorphous samples.

1.1 Ion Implantation in chalcogenide thin film

Amorphous phase in chalcogenide represents the crucial state of a device: this is essentially correlated to the RESET information stability, i.e. the propensity of amorphous phase to maintain its metastable arrangement upon increasing the temperature. Although stability enhances the data retention properties of devices, however, generally it elongates the pulse duration required to the SET (crystalline) programming [47].

A powerful tool to control the amorphization level of a specimen is ion implantation. This method consist of bombardment with ion projectiles that hitting the target can displace its atoms if the transferred kinetic energy is greater that the bounding energy. At each ion an amount of damage, i.e. target atom displacements, is then associated. When the damage reaches a threshold value amorphization occurs. The total distance which an ion mass M_1 travels in coming to rest in a target of atomic mass M_2 is called its range R. The distance along the axis of incidence is called the projected range R_p, and the distance travelled along the axis perpendicular to the axis of incidence is called the perpendicular distance $R_\perp$. R and R_p are mean values because the number of collisions per unit path length and the energy lost per collision are random variables, i.e. all the ions having the same incident energy do not stop at the same location. There is instead a distribution in space of stopping points which is described by a range distribution function. The fluctuation or straggle in the projected range is ΔR_p. The perpendicular distance or the lateral spreading, $R_\perp$, caused by multiple collision of the ions will increase with depth into the target and it is a function of the mass ratio M_2/M_1. For $M_2/M_1 \approx 0.1$, in th so-called heavy-ion implantation regime, we find $R_\perp \approx \Delta R_p$ and $R_\perp \approx 0.2R_p$. For $M_2 \approx M_1$, a good lateral spreading estimation is $R_\perp \approx 0.5R_p$ while $R_\perp \approx 2\ R_p$ if $\frac{M_2}{M_1} \approx 0.1$, i.e. for light ions. In the classical scattering theory [48] the interaction between the moving ions with the target atoms is described assuming two separate processes: elastic collisions with the nuclei, the so-called *nuclear* contribution, and inelastic collisions with the electron in the target, the so-called electronic contribution. The energy loss along the incidence direction x, is then described as

$$\frac{dE}{dx} = \left.\frac{dE}{dx}\right|_n + \left.\frac{dE}{dx}\right|_e \qquad (1.1)$$

The nuclear contribution is due to the Coulomb repulsion between the ion and the target nuclei. Excitation and ionization of host electron only affect the energy of the ion and they does not change its trajectory. In sum, every nuclear scattering event can deflect the ion trajectory while electronic energy loss only contributes to a continuous slowing down acting as a sort of friction force.

Generally, the nuclear term dominates at very low ion velocities while at higher ion energies electronic term can be several order of magnitude greater than the nuclear stopping. The occurrence of the first or the second regime, generally, depends on the comparison between the ion velocities and the velocities of the outer electrons of the host atoms.

When an ion impinges into the target it can displace host atoms from the crystalline lattice if the energy E' ceased by the ion is greater than the displacement threshold energy E_d ($\sim 15eV$ in Si and Ge, $\sim 25eV$ in Sb and Te). The extra energy acquired by the knock-on atom, $E' - E_d$, can be spent to travel through the target itself and produce secondary collisions, hitting other atoms, giving them energy and eventually producing secondary knock-on atoms if the energy is enough, and so on in a process called collision cascade. Displacing atoms from their lattice position collision cascades produce defects (interstitials, vacancies, etc.) in the target material.

Figure 12 and Figure 13 show collision cascades along beam incidence and transversal directions, respectively. Primary ion trajectory is shown in red, while secondary cascades are represented in green. The damage is then localized where the cascades overlap.

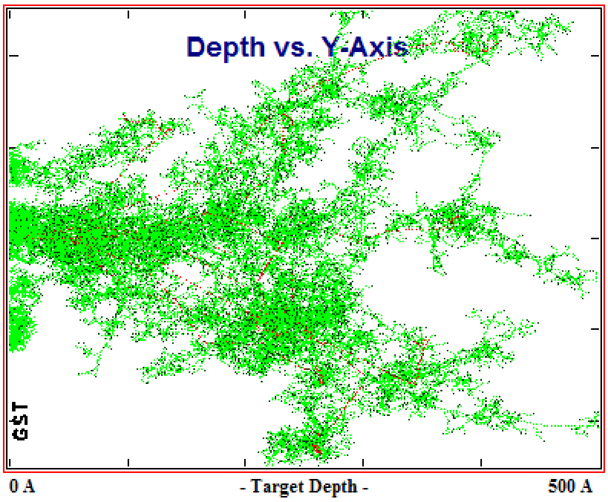

Figure 12 Ge^+ ions at 40 keV, impinging on a GST sample, produce collision cascade, shown along the beam incidence direction. Ion trajectories are indicated by red dots while secondary knocked out atoms in green.

Similarly to the ion range, we can associate several parameters to the damage profile. Approximating this profile with a Gaussian distribution we identify its center along the axis of beam incidence with D_p and we indicate with ΔD_p the relative straggling. The damage distribution extends also in the perpendicular direction and we indicate the relative lateral straggling as σ.

The damage distribution is mainly related to the energy deposited in nuclear encounters. This last term is related only to the ion energies and to the masses of the projectile and of the target atoms. The distribution of this energy can be deduced either analytically or based on Monte Carlo procedures. Nuclear encounters require target atoms and ions to approach very close, therefore, the probability for three or more particles collisions is extremely small.

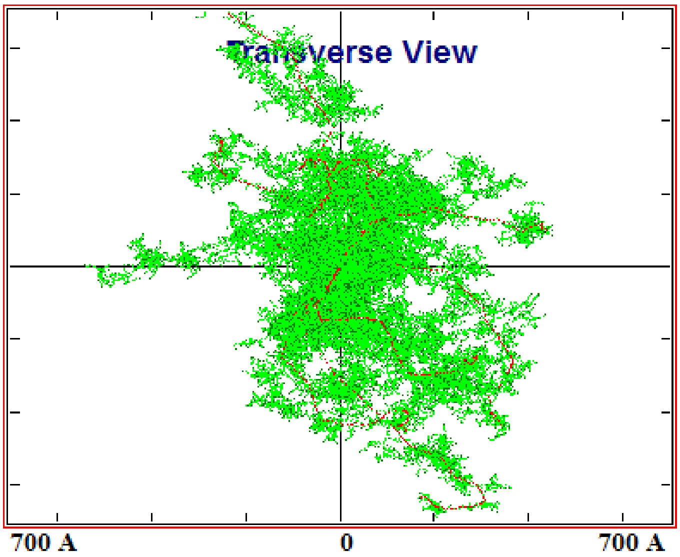

Figure 13 Ge$^+$ ions at 40keV, impinging on a GST sample, produce collision cascade, shown along the transversal direction (with respect to the beam incidence axis). Ion trajectories are indicated by red dots while secondary knocked out atoms in green.

Both simulations and calculations are then based on the Binary Collision Approximation (BCA). By the SRIM code [49], for instance, it is possible to simulate the ion implantation process with results closer to the experimental ones. The final structure of the damage depends however on the material, semiconductor, metal, insulator, etc., and on the temperature. In a semiconductor, for instance, light ion collisions occurs at a mean free distance very large with respect to the lattice parameter. As a consequence, damage is represented by a diluted distribution of point defects and the displaced atom profile present a buried peak. On the contrary, heavy ions the collision mean free path is of about the interatomic distance and, therefore, dense collision cascades are generated. Recoiled atoms transfer energy and damage to greater depths, producing the main contribution to the final damage profile.

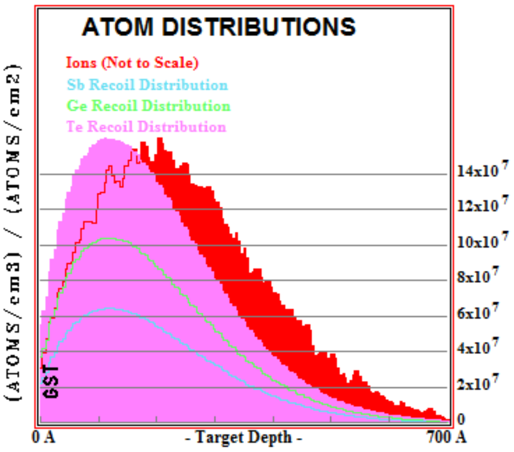

Figure 14 Ge$^+$ range distribution (Ions) and Ge, Sb, Te recoils, referred to the dose, along the beam incidence direction (SRIM calculation). Ion energy was set to 40 keV.

The elastic recoil loss, $\nu(E,x)$, is always 20%-30% less than the total nuclear stopping power because a fraction of the kinetic energy ceased to the target atoms is released by electronic excitations in subsequent collisions. The number of the displacement density can be obtained from $\nu(E,x)$ using the modified Kinchin and Pease expression:

$$n_d(x) = \frac{0.8\,\nu(E,x)}{2E_d} \qquad (1.2)$$

From the last expression, the target density N (at/cm^3) and the ion dose ϕ (at/cm^2) we can calculate the number of Displacements Per (target) Atom (DPA):

$$DPA = \frac{0.8\,\nu(E,x)\phi}{2E_d N} \qquad (1.3)$$

As a rule of thumb, generally amorphization occurs when $DPA \approx 0.3$, i.e. when there is a displacement in the target lattice every three atoms. As shown in Equ. (1.3), the ion dose ϕ plays a relevant role in reaching the amorphization threshold. Heavy ions produces large collision cascade, in which each particle can displace about $10^4 \div 10^5$ target atoms, with a damage lateral straggling of the order of ten nanometers. For low fluences ($< 10^{12}$) this produces isolated damage regions around each ion track. Complete cascade overlap requires high fluence ($> 10^{14}$) producing an uniform lateral distribution of damage and, therefore, amorphization.

In Figure 15a we show the DPA as function of the longitudinal direction, of a 20nm GST thin film on SiO_2, covered by 10nm of amorphous Silicon and the line of amorphization threshold (red).

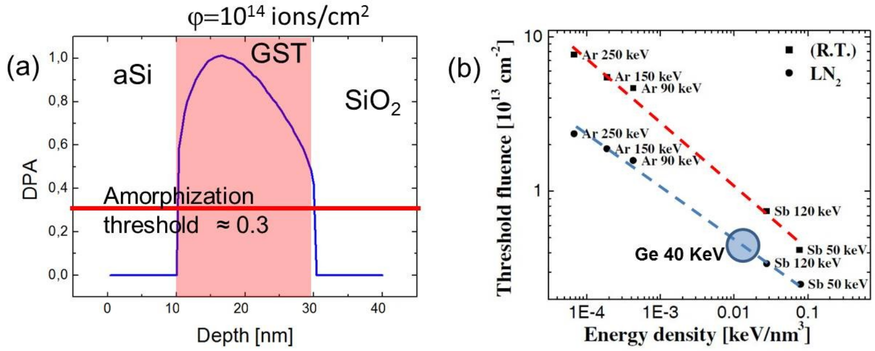

Figure 15 (a) DPA produced by 10^{14} Ge+ ions/cm^2 at 40 keV on a 20nm GST film protected by 10nm of amorphous Silicon. (b) Threshold amorphization fluence produced by different ions and energy at R.T. (squares) and at LN_2 temperature.

Finally, temperature plays a relevant role in determining the effective amorphization fluence. Electronic energy (and extra displacement energy ceased to host atom during nuclear encounters) is dissipated by lattice vibration. As the temperature increases, defect mobility increases exponentially and, as a consequence, they can partially annihilate dynamically the produced damage. This observation justify the experimental results (Figure 15b), performed on a GST thin film [50], showing that the amorphization threshold depends on the temperature of the target during the implantation: it decreases as the target temperature decreases.

1.2 Comparison between as deposited and ion implanted amorphous GeTe by Optical Microscope

In the first part of this study, we have irradiated amorphous regions next to as deposited ones on a GeTe thin film using the masking technique aforementioned. Thin GeTe films 50 nm thick were deposited at room temperature (RT) by RF-magnetron sputtering, from a stoichiometric target, over a thermal 550 nm thick SiO_2 covering a Si substrate. Then, each sample was covered with a gold circular mask (thickness ≈ 25 µm, diameter ≈ 3 mm).

The ion irradiation was performed at R.T. using 130 keV Ge+ ions at fluence of $1x10^{14}$ ions/cm^2. This dose and the beam energy values were chosen in such a way to reduce the effect of sputtering, produced by Ge+ ions at high fluencies (>$1x10^{15}$) and then to avoid any appreciable change in the stoichiometry of the film.

The ion projected range R_p (obtained through SRIM simulations) is 54 nm, with a straggling ΔRp ≈24 nm (Figure 16).

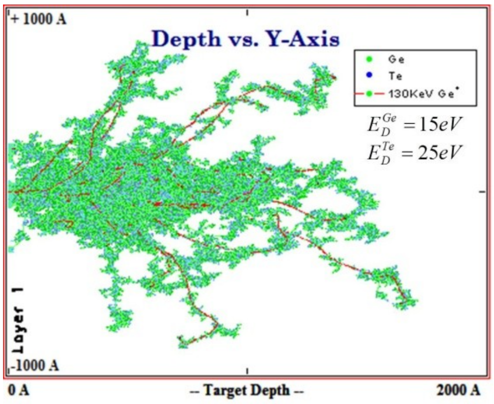

Figure 16 Ge+ ions at 130 keV producing collision cascades in GeTe

The beam current was kept constant to smaller values (100 nA) to avoid heating of the sample. A nearly uniform nuclear energy loss across the layer thickness was also obtained with the settled irradiation parameters Figure 17.

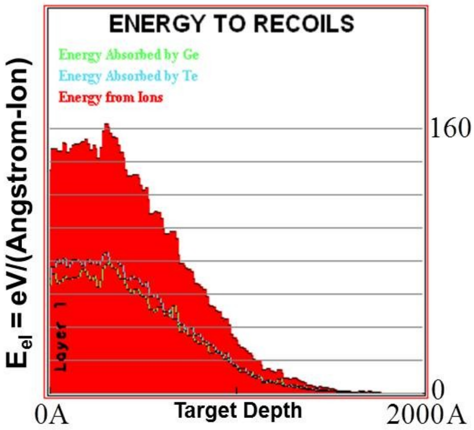

Figure 17 Energy to recoils produced by ion implantation of Ge+ ions at 130 keV

As one can note from Figure 18, displaying the DPA, this configuration produces a good distribution of damage along the sample, well over the 0.3 amorphization threshold.

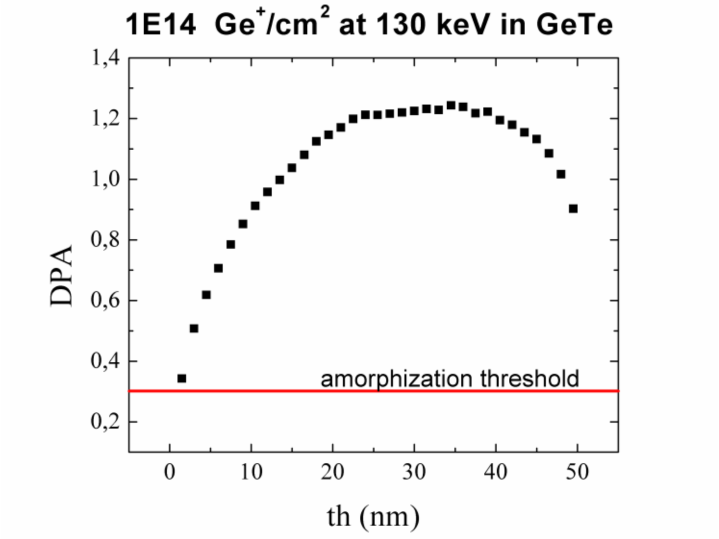

Figure 18 DPA produced in a 50 nm thick GeTe film by 10^{14} Ge+ ions/cm^2 at 130 keV

Once we have two kinds of amorphous GeTe in the same specimen, the crystallization kinetic of the sample has been investigated in situ by means of Optical Microscopy during annealing in the 143-155 °C temperature range. The Mitutoyo microscope used during the observation was equipped with a 20x objective lens and a stage position measurement system. With this configuration, the images of the sample were stored with an optical resolution ≈1 µm. During the annealing processes, oxidation was avoided by continuously fluxing the sample with dry nitrogen.

The large area covered by a single GeTe grain, few microns, before coalescence permits a direct estimation of the nucleation and growth processes.

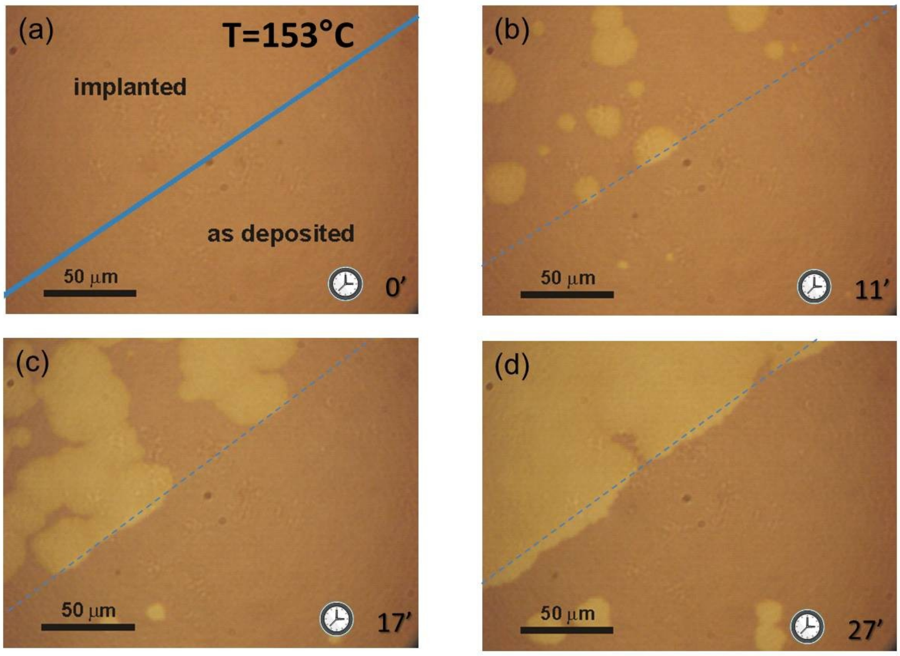

Figure 19 Optical sequence of a GeTe sample irradiated with Ge+ at a fluence of 1x10^{14} ions/cm^{2} on the left upper region (a) and annealed at 153 °C. The crystallization dynamic is faster in the implanted region where it is complete after 27 minutes (d) while in the contiguous unirradiated amorphous region the process is just starting. Note that the grain growth velocity slows down at the border of the unirradiated area (dashed line).

A typical sequence of optical images is shown in Figure 19 for a sample annealed at 153 °C. The analyzed region spans both an as deposited amorphous area and a contiguous irradiated amorphous region. The sample was annealed at 153 °C for different times. The enhancement of both nucleation rate and grain growth velocity in the irradiated area is clearly visible as well as the stop of the growing grain at the border of the unirradiated area. In addition, the sharp interface between the ion implanted and as deposited amorphous regions permits a direct observation of the change in the growth velocity of a grain when it crosses the boundary of the two systems.

At each settled temperature several images have been stored. From them, the area of each grain has been obtained and the relative radii have been calculated by circle-area approximation, i.e. valuating the area of each grain and assigning to it a radius measurement $r = \sqrt{A/\pi}$.

In Figure 20 the radius of the crystalline grains measured in the as deposited and ion implanted regions is reported as a function of time during annealing at 149 °C. The data refer to the size of five different grains in each region. The grain radius increases linearly with time and the slope (extracted from the linear fit) directly gives the growth velocity. The growth velocity, at 149 °C, in the as deposited amorphous region is G=2.7± 0.1 nm/s, rising to G=9.3± 0.5 nm/s in the irradiated area. Similar experiments were performed at other temperatures, and all over the investigated range the growth of the grains in the irradiated region is nearly three times faster that measured in the un-irradiated area.

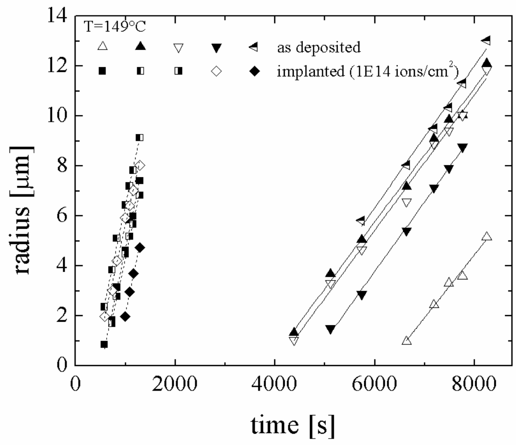

Figure 20 Time dependence of the grain radius during annealing at a temperature of 149°C in irradiated and unirradiated amorphous regions respectively. For each set of data, the line (solid for the as deposited samples and dashed for the implanted ones) represents the linear fit of the radius as function of time (correlation coefficients > 0.99). The growth

velocity, G=9.3±0.5 nm/s (defined as the slope of the linear fit), is 3 times faster in the region implanted with 10^{14} ions/cm^2.

The grains surface density has been measured as a function of the annealing duration. As an example, the time dependence of the grain density during annealing at 149 °C is reported in Figure 21. The slope of the curve gives a measure of the steady state nucleation rate and an enhancement of the nucleation rate in the irradiated area by a factor ≈13 is clearly visible.

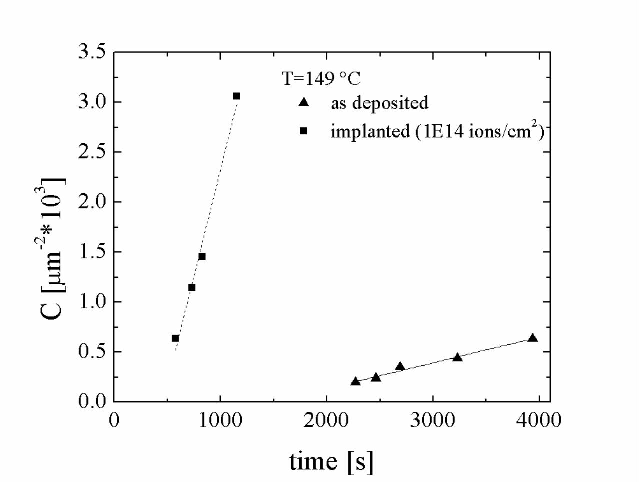

Figure 21 Time dependence of the grain density C, at the annealing temperature of 149 °C in the irradiated (1x10^{14} ions/cm^2) and unirradiated regions. For each set of data, the line (solid for the as deposited samples and dashed for the implanted ones) represents the linear fit of C as function of time (correlation coefficients > 0.99).

The grain growth velocity has been reported in Figure 22 in a semilog scale as a function of $1/k_BT$ for both irradiated and un-irradiated regions. The reported values are the averages performed on several grains and the error bar indicates the spread of the measurements. A similar procedure was adopted for the temperature dependence of the nucleation rate and the data are reported in Figure 23.

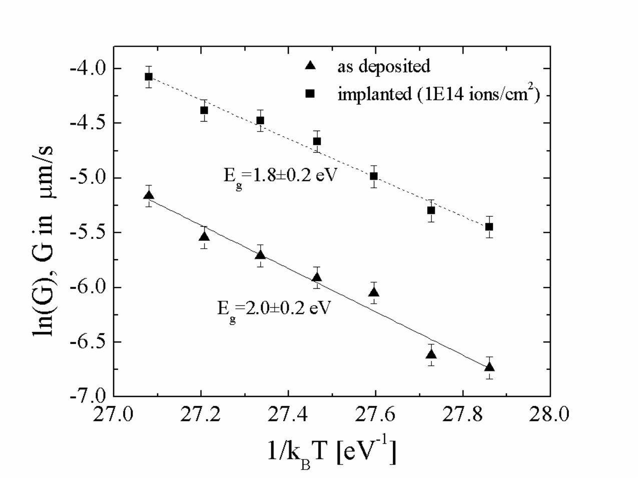

Figure 22 Arrhenius plot of the grain growth velocity, G, at several temperatures for the as deposited amorphous (▲) and the implanted (■) samples respectively. For each set of data, the line (solid for the as deposited samples and dashed for the implanted ones) represents the linear fit of ln(G) as function of 1/kBT. The fit parameters, G_0 and E_g according to Eq. (1.4), and the correlation coefficients are reported in Table 1.

Both the graphs show that grain growth velocity and nucleation rate follow an Arrhenius behavior, respectively given by

$$G = G_0 \exp\{-E_g/(k_B \mathrm{T})\} \qquad (1.4)$$

and

$$\mathrm{I} = I0\exp\{-En/(kB\mathrm{T})\} \qquad (1.5)$$

being G_0 and I_0 the pre-exponential terms and E_g and E_n the activation energies of the two processes respectively. The value of E_g and G_0 have been extracted by the linear fit of $\ln(G)$ data as function of $1/(k_B\mathrm{T})$. The same procedure was used to extract the value E_n and I_0 from the nucleation data. The fitting parameters and the correlation coefficients of these fits are reported in Table 1.

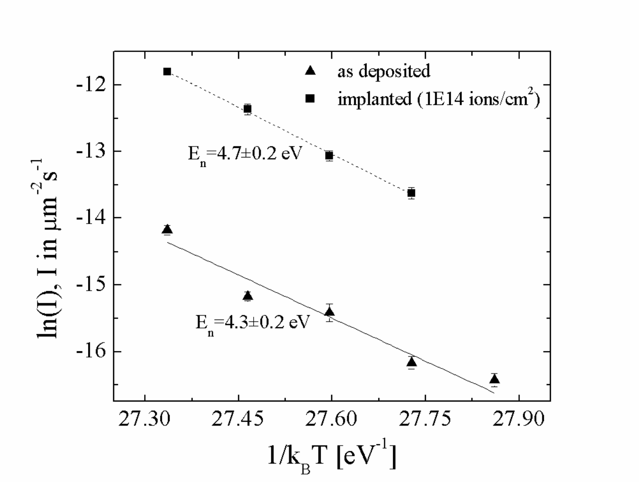

Figure 23 Arrhenius plot of the nucleation rate, I, at several temperatures for the as deposited (▲) and the implanted (■) samples respectively. For each set of data, the line (solid for the as deposited samples and dashed for the implanted ones) represents the linear fit of ln(I) as function of 1/k_BT. The fit parameters, I_0 and E_n according to Eq. (1.5), and the correlation coefficients are reported in Table 1.

Table 1 Crystallization parameters of GeTe as found by in situ optical measurements.

	as deposited	**Irradiated**
Correlation coefficient (Growth velocity fit)	0.98	0.992
ln(G_0), G_0 in [μm/s]	48±4	44±4
E_g	2.0±0.2 eV	1.8±0.2 eV
Correlation coefficient (Nucleation rate fit)	0.97	0.9994
ln(I_0), I_0 in [/μm^{2}s]	103±6	117±6
E_n	4.3±0.2 eV	4.7±0.2 eV

1.3 Comparison between as deposited and ion implanted amorphous GeTe by TRR measurements.

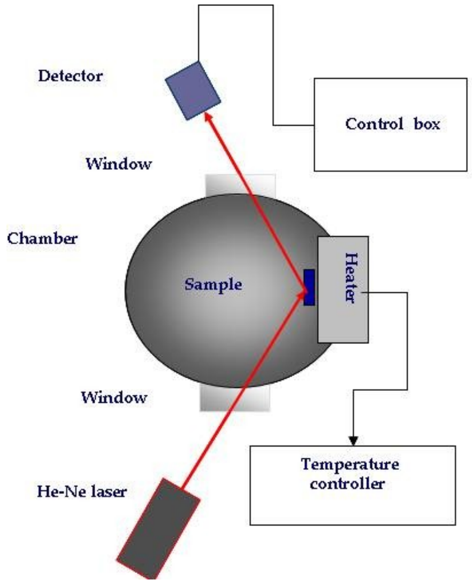

Figure 24 Time Resolved Reflectivity setup. The sample is placed in a vacuum chamber at a pressure of about 10^{-3} Torr. Samples is heated at a set temperature with a PID controlled heater. During annealing, a 5mW He-Ne laser beam reflects on the sample and its power is then measured by a photodiode.

Time resolved reflectivity measurements, using a He-Ne laser (λ=633 nm, P=5mW), were performed to monitor the fraction of crystallized material during the annealing in the range 147-154 °C. The sample were placed in a vacuum chamber at a pressure of about 10^{-3} Torr (Figure 24). For both the systems, the heating rate was 10° C/min and the settled temperature was constant within ± 0.1 °C.

This method takes advantage of the difference between the optical constants of the two phases to correlate the actual reflectivity to the fraction of transformed material over the probed region that is of the order of the laser extinction length (10 and 20 nm for crystal and amorphous GeTe, respectively). However, the crystallized film has a columnar structure with a crystalline grain size of the order of few microns and so it's reasonable to assume that the volume fraction of crystalline material coincides with the surface fraction detected by TRR.

Typical time resolved reflectivity curves of unimplanted amorphous GeTe, annealed at different temperatures, are shown in Figure 25. The crystalline volume fraction χ is obtained from the experimental TRR data, according to the linear approximation, widely demonstrated for GST [51]:

$$\chi = \frac{R_m - R_{am}}{R_{xtl} - R_{am}} \qquad (1.6)$$

Where χ is the crystalline fraction on the probed sample, R_m is the measured reflectivity, R_{am} is the reflectivity of an amorphous sample and R_{xtl} is the reflectivity of a crystalline sample. This equation assumes that the grains have a prism-like-shape across all the film thickness with a base at the free surface and it has been extensively adopted in literature to study the crystallization of chalcogenide amorphous layers.

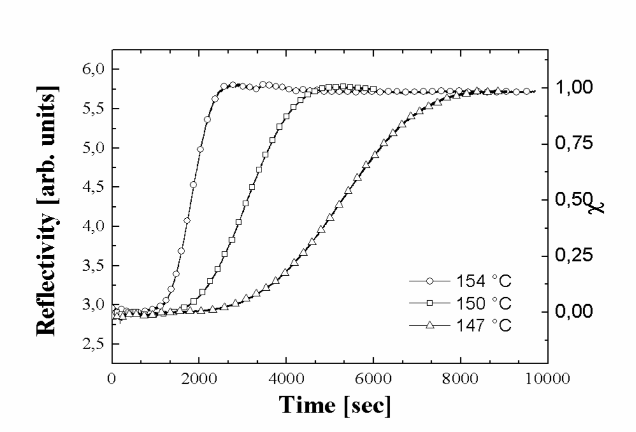

Figure 25 Time dependence of the reflectivity during annealing at different annealing temperatures of as deposited amorphous GeTe layers.

We define the characteristic crystallization time τ_0 as the time at which the time-derivative of $\chi(t)$ reaches the maximum, being the origin of the time scale coincident with the time at which the settled temperature is reached. The characteristic time of the as-deposited and implanted samples is reported in Figure 26 as a function of the inverse of temperature. An enhancement of the crystallization rate occurs in irradiated GeTe over the investigated temperature range. The τ_0 values measured at different temperatures follow an Arrhenius law with an activation energy of E_i=3.0±0.1 eV and E_i=2.5±0.1 eV for the unimplanted and implanted samples, respectively.

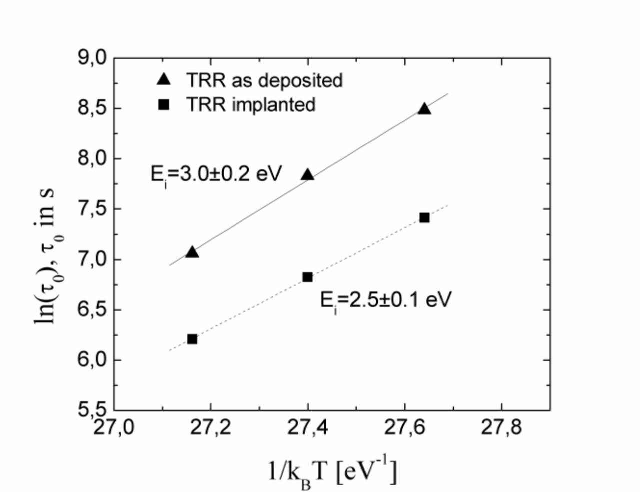

Figure 26 Arrhenius plot of the crystallization time, τ_0, at several annealing temperatures for the as deposited (square) and implanted amorphous (triangle) samples.

1.4 The JMAK Model

The information achieved by TRR is global, since it does not discriminate the different contributions responsible of the crystallization, i.e. nucleation and growth of the new phase. On the other hand, the nucleation and growth terms have been independently determined by means of optical microscopy.

In this context a reliable model is necessary in order to connect the two different approaches and to analyze them in a wider context. The JMAK model [52-59] connects the transformed volume fraction, during isothermal annealing, to the nucleation and growth parameters. This model assumes a random nucleation in the amorphous layer and neglects the lag time, before which the nucleation rate is zero. At a given temperature T, the time dependence of the crystalline volume fraction χ is given by

$$\chi(\mathrm{t}) = 1 - \exp\{-\mathrm{k}t^{n}\} \qquad (1.7)$$

where the Avrami exponent n is an integer that depends on the nucleation and growth mode, and k is a parameter whose temperature dependence follows an Arrhenius law:

$$\mathrm{k(T)} = k_0 \exp\{-\Delta\mathrm{H}/k_B\mathrm{T}\} \qquad (1.8)$$

where ΔH is the activation energy of the whole crystallization process. It has been shown [60] that the Avrami exponent is given by:

$$\mathrm{n} = \mathrm{a} + \mathrm{bc} \qquad (1.9)$$

where a is the nucleation index, b is the dimensionality of the growth (b=1,2 or 3, one, two or three-dimensional growth of the crystalline grain) and c is the growth index. In the present case b=2 and c=1, being the growth two dimensional and interface-controlled. In fact, the grain size is much larger than the film thickness and the growth velocity is time independent all over the investigated range (Figure 20). The nucleation index *a* is correlated to the time dependence of the nucleation rate I by the following

$$I = I_0 t^{a-1} \exp\{-E_n/(k_B T)\} \qquad (1.10)$$

where E_n is the activation energy for nucleation. In our sample a=1 since we have shown (Figure 21) that the grain density increases quite linearly with time. Therefore in the investigated regime both the nucleation and growth rate are time independent and then Eqs. (1.4) and (1.5) well describe the temperature dependence according to the JMAK model. Under these conditions the k parameter is related to the nucleation and growth rate according to the relation

$$k = (\pi/3) G^2 I \qquad (1.11)$$

Moreover, the overall activation energy for crystallization ΔH is related to the activation energies of the individual processes, E_n and E_g, by the following:

$$\Delta H = E_n + bcE_g \qquad (1.12)$$

In our analysis E_n and E_g were determined by *in situ* optical microscopy; ΔH was estimated from TRR measurements.

In the JMAK model approximation, crystallization , described with Eqs. (1.4)(1.5)(1.6), take places after an *incubation time*, during which no nucleation and growth processes occur. Incubation time is temperature-dependent according to the equation

$$\tau_0 = \tau_{00} \exp\{+E_i/(k_B T)\} \qquad (1.13)$$

where E_i is an activation energy related to the JMAK parameters according to the equation

$$E_i = \Delta H/n \qquad (1.14)$$

the characteristic crystallization time, indicated by the maximum of $\chi'(t)$, is expected to be about the incubation time and it therefore follow an arrhenian behavior, as Figure 26 reflects. In the following section we will use Equ. (1.13) to analyze the characteristic time.

To summarize: optical measurements directly provide G(T), I(T), G_0, I_0, E_n and E_g, while TRR provides χ(t), τ_{00} and τ_0. ΔH can be determined from the optical measurements using Eq. (1.12) with b=2 and c=1.

In the next paragraph we show that, through simple approximations, it is also possible to find the value of k(T) and n from TRR and to compare them with those determined by the optical measurements through the JMAK model.

1.5 Comparison between TRR and Optical Microscopy in situ measurements

Several procedures are reported in literature to obtain from TRR curves the physical quantities of the JMAK model and different results are presented according to the different methods [61-63]. In particular both the Avrami exponent and the k parameter of Eq. (1.7) can be obtained by the plot of ln(-ln(1-χ)) vs ln(t). However the results can be affected by the choice of lag time and by the time unit. To avoid this ambiguity we follow another procedure. The Avrami exponent, n, was obtained by the plot of ln(-ln(1-χ)) vs ln(t/τ_c) (Figure 27). At each temperature, the τ_c value was found assuming τ_c=k(T)$^{-1/n}$ as the time at which χ(τ_c,T)=0.63.

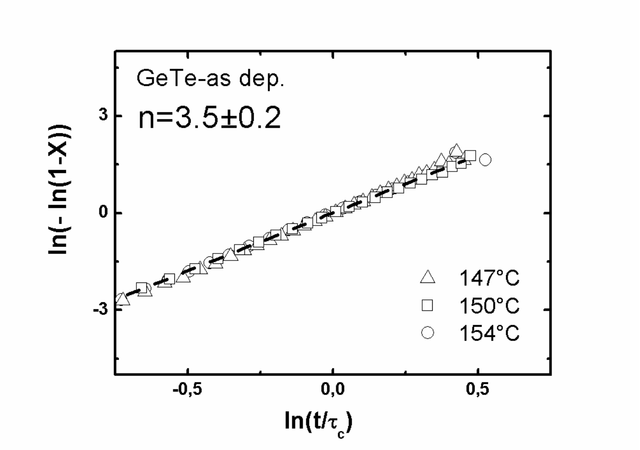

Figure 27 the Avrami exponent, n, is obtained by the plot of ln(-ln(1-χ)) vs ln(t/τc). At each temperature, the value has been found by posing τ_c =k(T)$^{-n}$ as the time for which χ(τ_c,T)=0.63

This procedure is similar to that used by Cros et al. [63] to describe amorphous to crystalline transformation of $CoSi_2$ films. The definition of τ_c follows straightforwardly from Eq. (1.7). For both as deposited and ion implanted GeTe samples we found n≈3.5.

On the other hand, the n and k parameters can be determined by fit the TRR data (Figure 25) in the region $\chi<0.3$ using the approximation

$$\chi \approx kt^n \qquad (12)$$

We found $n\approx3.3$. The ln(k) is reported as a function of $1/k_BT$ (empty symbols), in Figure 28, along with the ln(k) values determined by optical microscopy (full symbols) for both irradiated and unirradiated amorphous GeTe. The good match between the two different approaches is evident and the irradiation only affects the value of the pre-exponential factor. The crystallization parameters obtained by the TRR analyses are summarized in table II. The values of $E_i=\Delta H/n$ are obtained, according to Eq. (1.14), by the fit curves in Figure 28.

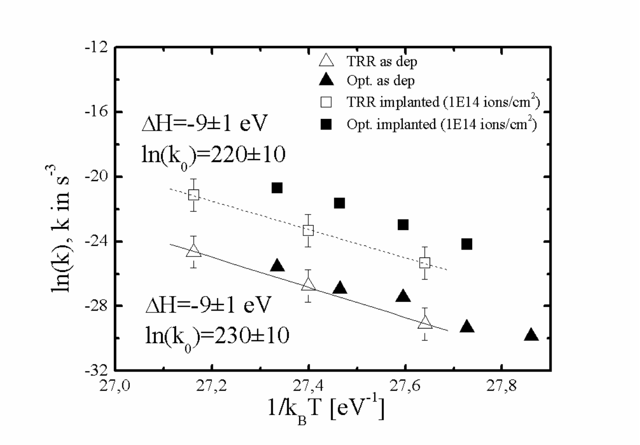

Figure 28 Arrhenius plot of k at several temperatures for the as deposited (square) and implanted (diamond) samples by TRR and optical (full) microscope measurements. For each data set the values of ΔH and $\ln(k_0)$ are reported in tab. II.

Also, through the model described above, we have extended in table III the parameters extracted by the optical data analisys.

The values for ΔH and ln(k_0) obtained with the two methods are in good agreement taking into account the uncertainness associated to these measurements.

Table 2 Crystallization parameters as found by TRR measurements using JMAK approach.

	as deposited	**Irradiated**
ΔH/n	3.0±0.2eV	2.5±0.1eV
n	3.3±0.2	3.4±0.2
a	1.3±0.2	1.4±0.2
ΔH	9±1eV	9±1eV
ln(k_0), k_0 in [s^{-3}]	230±10	220±10

Table 3 Crystallization parameters as found by optical measurements using JMAK approach.

	as deposited	**Irradiated**
ΔH	8±1eV	9±1eV
ln(k_0), k_0 in [s^{-3}]	203±22	225±31

1.6 An insight on the different amorphous structures by means of Raman Spectroscopy measurements

We have analyzed as deposited, ion implanted and melt-quenched amorphous GeTe specimens by micro-Raman spectroscopy recording in a backscattering geometry using a single spectrometer. The as deposited and ion implanted samples are the same used in the previous sections, while melt-quenched specimen has been obtained by an as sputtered sample laser irradiated. The laser was a frequency-doubled Nd:YAG at 532 nm. The laser pulse duration was about 10 ns at an energy density of 150 mJ/cm2. The spot size was 2 mm.

The samples for the Raman analisis were excited with a He-Ne laser (λ=633 nm), focused to ≈6 μm using a microscope objective lens. The incident laser power was adjusted to 2 mW in order to minimize heating effects in the illuminated sample region.

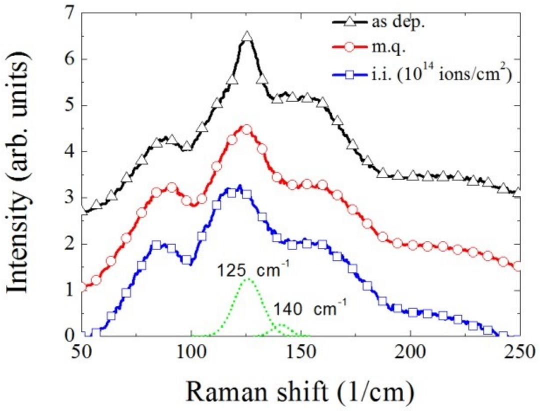

Figure 29 Raman spectra of different amorphous GeTe films: as deposited (line + open triangles), melt quenched (line + open circles) and ion implanted (line + open squares). The dotted lines represent the contribution of the 125 cm^{-1} and 140 cm^{-1} peaks to the as deposited Raman spectrum, according with the band assignment reported in [36].

Melt quenched and ion implanted amorphous layers present very similar Raman spectra, as shown in Figure 29. These two spectra are quite different with that concerning the as deposited sample. In particular, stronger bands at 125 cm^{-1} and 140 cm^{-1} are present in the as deposited sample. The interpretation of the Raman signal is still under debate and different models of the GeTe amorphous structure are present in the literature [64][65]. It is not clear if fourfold coordinated Ge atoms are mainly in a tetrahedral configuration [64] or, as recently pointed out, in a defective octahedral one [65]. Raman peaks are then alternatively attributed to the symmetric stretching mode of corner-sharing and edge-sharing Ge tetrahedral [64] or to the vibrational mode of defective octahedral sites [65].

Moreover, it is possible that the presence of Te-Te dimers and trimers [64][34] contributes to the intensity of the bands at 125 cm^{-1} and 140 cm^{-1} in the as deposited Raman spectrum. It is known that crystalline Tellurium has the stronger peaks at 121 cm^{-1} and 141 cm^{-1} [66].

Theoretical calculations [34] show the presence of homopolar bonds, called wrong bonds, in as deposited amorphous samples. Since these bonds are not present in the crystalline phase, they act as an obstacle during crystallization, enhancing crystallization time and temperature with respect to the m.q. amorphous system. Also, recent theoretical models [25] on m.q. amorphous systems show the presence of a crucial structural motif of misaligned ABAB squares (A=Ge,Sb for GST, A=Ge for GeTe; B=Te), which can straightforward rearrange to the crystalline configuration. Numerical simulations [34], performed on GST, show that these motifs are less in as deposited samples probably due to the presence of the homopolar wrong bonds. Moreover, ABAB squares in melt-quenched GST are correlated with a defective octahedral environment, in agreement with other simulations [27], whereas as deposited GST is expected to have a greater number of tetrahedral structures [34].

Therefore, in comparison with as deposited sample and according to simulations, we believe that a reduction of the homopolar Te-Te bonds, forbidden in the crystalline structure, occurs during ion implantation. Consistently, the Raman spectra collected in the amorphous region of partially crystallized GeTe film exhibited a reduction of the 125 cm^{-1} peak intensity similar to that observed in the irradiated samples [36]. This evidence further confirms that ion implantation establishes a favorable environment for crystallization.

1.7 Discussion

The experimental results indicate clearly an enhancement of the crystallization rate in irradiated as deposited amorphous GeTe thin films. The absolute value of the nucleation rate and of the grain growth rate depends strongly on the sample preparation and on the ion implantation conditions, besides on the system calibration. We have, then, compared our results with others referring to as deposited GeTe.

A similar analysis, based on optical images [67] gave an activation energy E_g=1.77±0.14 eV and a pre-exponential factor $G_0=6x10^{20}$ μm s^{-1} for the grain growth velocity in good agreement with our determination ($G_0 \approx 10^{21}$ μm s^{-1}, E_g=1.8±0.2 eV). The measured activation energies of the nucleation rate are E_n=4.3±0.2 eV in the as deposited region and E_n=4.7±0.2 eV in the implanted one, while the activation energy for incubation time, as determined by TRR measurement, was 3.0±0.2 eV and 2.5±0.1 eV respectively.

Also, we have analyzed, by comparison, the Atomic Force Microscopy (AFM) images reported in ref. [68] of as deposited amorphous GeTe film annealed at 165°C. The adopted method relies on the higher density of the crystalline phase with respect to the amorphous one (~5%). A growth velocity of 4.1 nm/s has been obtained. The extrapolation of our data at this temperature provides instead G= 19 nm/s, i.e. a factor 5 higher than that previously reported. This variation can be accepted, taking into account that the crystallization kinetics is strongly dependent on sample stoichiometry [69], interfaces, presence of capping layer and contaminants. A greater difference, of about two orders of magnitude, has been found instead with respect to the measurements of ref. [67], probably due to a difference in the temperature calibration.

Nevertheless, this result demonstrates that the comparison between different kinds of amorphous samples must be performed on the same sample, possibly considering contiguous region, as in our setup.

Moreover, the implantation must be performed at low fluences to avoid any spurious effect. As well known, indeed, phase change materials crystallize usually by heterogeneous nucleation at free surface or interfaces. Ion implantation might cause a change of the surface chemical composition by a mixing of the surface layer (oxide, contaminants etc.) with the underlying film. It has been found [68] that ion irradiation, with a fluence above 10^{15}/cm2, of a GST film covered with a thin SiO2 layer, causes a retardation of the crystallization process due to the recoil implantation of oxygen and silicon. In the present work, the amount of recoiled contaminants present on the sample surface is practically negligible due to the low value of adopted fluence. Moreover, the presence of contaminants should retard the crystallization process instead of enhancing it. In addition, the influence of ion irradiation on the growth velocity clearly indicates that the phenomenon is associated to the change of the local order induced by ion irradiation.

Raman spectroscopy supported important information about the mechanism involving the crystallization process. The amorphous to crystalline transition has been described in terms of a local structure change from a Ge-rich tetrahedra to a Te-rich one [23][69] or, as recently reported from 3÷5 fold coordinated defective octahedral Ge or Te sites to ordered octahedral sites [65]. During sputtering deposition, random positioning of the Ge and Te atoms permits the formation of homopolar bonds. Ion irradiation gives local mobility to the host atoms, permitting the relaxation of the amorphous structure and promoting the system to a state closer to the crystalline phase. The local rearrangement has been associated to the thermal spike created by the dense collision cascade during the ion implantation [36]. It has been estimated that a temperature spike of 870 K for a duration of 10 ps is enough to justify a local rearrangement of GeTe bonds, in a mechanism closer to the melt-quenching observed in optical or electronic devices. An experimental evidence of amorphous ion induced relaxation is shown in Figure 19. At first, nucleation takes place in the irradiated area, after an incubation time shorter than that occurred in the as deposited area. Grains grow very fast reaching the implantation interface and continuing their growth in the unirradiated region. Here, their velocity slows down to the same value found for the grains nucleated in the as deposited area. The higher value found in nucleation rate and growth velocities of irradiated film can be ascribed then to a more favorable energetic surrounding in which crystallization takes place. In this environment the lattice organization can occur easier because, probably, every step concurring to crystallization must overcome the same or near the same energy barrier encountered in the unirradiated amorphous sample, but more sites are rearranged at the same time. As a matter of fact, indeed, a small change in the critical free energy for cluster formation ΔG_c is enough to take into account the observed variations in the ratio I/G between nucleation rate and growth velocity for the irradiated and as deposited amorphous samples [70]. This term is diffusion-independent according to the locally diffusion-limited crystallization model. A difference $\Delta G_c^{1E14} - \Delta G_c^{as\ dep} = 0.04 \pm 0.01$ eV for the implanted region is able to justify the experimental data.

The extraction of elementary physical quantities as the activation energy for atomic migration, the activation energy of the nucleation rate and the relative pre-exponential factors has been performed analyzing the crystallization process over a narrow range of temperature. This range is imposed by the crystallization time that must be large enough to let the optical evolution well-discernible (tens of minutes) and smaller enough to avoid sample degradation. The grain growth activation energy results slightly lower in the irradiated samples (1.8 eV ± 0.2 eV) with respect the unirradiated region (2.0 eV±0.2 eV). The vice versa does for the activation energy of the nucleation rate: 4.3±0.2 eV in the as deposited sample and 4.7±0.2 eV in the irradiated sample. An opposite behavior characterizes the pre-exponential factor; it is higher for the nucleation rate of the irradiated amorphous samples and lower for the growth velocity of irradiated samples with respect to those of the unirradiated amorphous ones.

However, an interpretation of the results found in this temperature range is not trivial and their extension to a larger range is under investigation. We operate, in fact, near the glass temperature of GeTe, where the viscosity of the alloy follow a non-arrhenian law, influencing the behavior of all the kinetic parameters.

However, it is evident that the process is characterized by huge values of the pre-exponential factors that govern both nucleation rate and grain growth if compared with those characteristic of other materials. The pre-exponential of the growth velocity of the Ge crystalline grains during the amorphous to crystal phase transition [71] is about 10^9 cm/s while that of GeTe is about 10^{17} cm/s. Therefore, a difference of eight orders of magnitude in the pre-exponential factor holds. The high values found for chalcogenides are characteristic of atomic mobility in the liquid phase and probably they underline the glass character of the amorphous state that is maintained during the transition to the ordered phase. As argued in [34] the high pre-exponential values can be explained through the high configurational entropy due to the peculiar chalcogenide structure and to the presence of a certain amount of vacancies [69]. In particular, in GST, the crystalline structure in the metastable phase has been shown to be rock-salt, i.e. divided in two face-centered-cubic (f.c.c.) sublattices. One f.c.c. structure is occupied by Te atoms. The other f.c.c. is randomly occupied by Ge and Sb atoms and vacancies (20% of the sublattice).

GeTe lattice presents a similar distorted rock-salt structure [72] in which Te atoms occupy a f.c.c. sublattice while Ge atoms and vacancies (about 10% of the sublattice) [73] form the other one. In this scenario, the difference of four order of magnitude between the growth velocity pre-exponential of GST, about 10^{21} cm/s [13], and the present value found for GeTe ($\approx 10^{17}$ cm/s), can be explained by the less amount of configurations compatible with the lattice structure of GeTe, based on the absence of Sb and the reduced number of vacancies.

Chapter 2

Fabrication and characterization of amorphous nano-structures of $Ge_2Sb_2Te_5$ for amorphous to crystalline transition study

Many works in the literature are devoted to understand the amorphous to crystalline transition in phase change materials thin film [23, 30, 37]. Several analysis methods, spanning from kinetics investigations (Time Resolved Reflectivity and Resistivity, static tests etc.) to structural ones (XRD, EXAFS, PDF), support important data about the material bulk behavior. This kind of analyses has suggested fundamental information about the phase change mechanisms in chalcogenide and, providing information about metastable phase stability, electro-optical characterization and thermodynamics data, have revealed an important roadmap in which material scientist and industries have moved to fabricate new PCRAM devices [28].

However, as discussed in the introduction, the condition in a confined nanostructure, in which PCRAMs operate, can be very different from the bulk configuration. Several characteristics, regarding the surface/volume ratio, the thermodynamics and the interfaces, can depend from the dimension in which the active volume of the device is confined. Many others strictly depends on the environment in which this volume is located, on the processes it suffers during fabrication and on the solicitations it undergoes during its programming/operation.

A deeper inside investigation in these subjects is then necessary. In this chapter we propose a method to fabricate nano amorphous structure, either surrounded by crystalline phase or isolated, by the aid of Electron Beam Lithography and selective ion implantation.

2.1 *Fabrication of nano structures by Electron Beam Lithography*

The $Ge_2Sb_2Te_5$ (GST) amorphous films, 20 nm thick, were prepared by RF sputter deposition at room temperature using a stoichiometric target, over a 100 nm SiO_2 layer thermally grown on silicon wafers. The film was covered by a 10 nm thick amorphous silicon layer deposited by RF sputter. This film protects the GST layer during the subsequent etching of the EBL PMMA mask and also enhances the film adhesion with the Hydrogen silsesquioxane (HSQ) EBL resist [74]. Also, amorphous Silicon layer prevents the GST film from further oxidation.

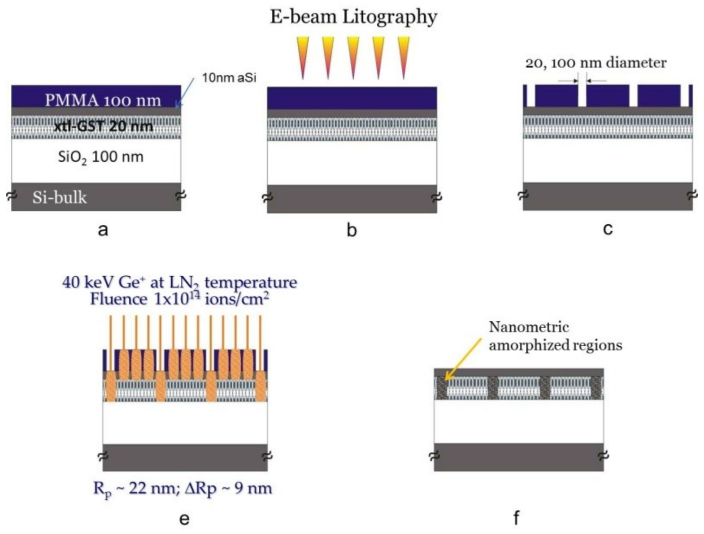

Figure 30 Flow-chart involving nano amorphous regions fabrication: over a 20nm GST film, protected by an overlayer of 10nm amorphous silicon, apertures ranging from 20 to 100 nm are patterned by EBL. The sample is then irradiated by Ge+ ions at suitable energy and fluence. Under the apertures, ion damage produces amorphization.

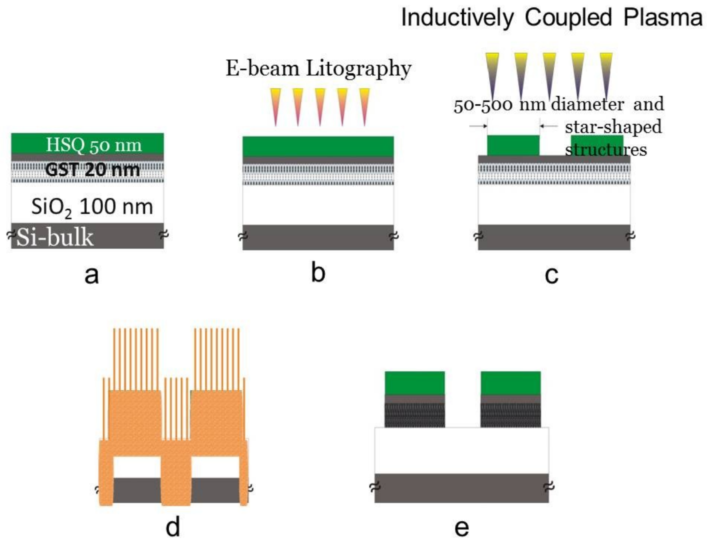

Figure 31 Flow-chart involving isolated nano amorphous region fabrication: over a 20nm GST film, protected by an overlayer of 10nm amorphous silicon, resist dot ranging from 50 to 500 nm, together with star-shape structures, are patterned by EBL. Resist geometries are transferred to the GST layer by Inductively Coupled Plasma (ICP). Structure are finally irradiated by Ge+ ions at suitable energy and fluence to amorphize the GST nano structures.

2.1.1 Nano-apertures

As-deposited amorphous films were crystallized by isothermal annealing at 180 °C and 350 °C for 10 minutes in order to obtain, respectively, a face centered cubic (f.c.c.) and hexagonal close packed (h.c.p.) phase.

In both the crystalline films a pattern of 100 nm and 20 nm circular apertures were obtained by an E-Line Raith apparatus on a 950k Poly-methyl methacrylate (PMMA) resist 100 nm thick. At the accelerating selected voltage, 20 kV, the electron beam diameter is less than 2 nm.

PMMA is a positive polymeric resist (Figure 32), i.e. the radiation exposed fraction is removed. After GST annealing, the resist is applied by spinning a solution of 2÷4% PMMA in ethyl lactate at 2000 rpm for one minute to obtain an uniform covering film. Then, we perform a bake process of two minutes at 120°C in order to eliminate the solvent. This sequence produces an overlayer of PMMA about 100 nm thick.

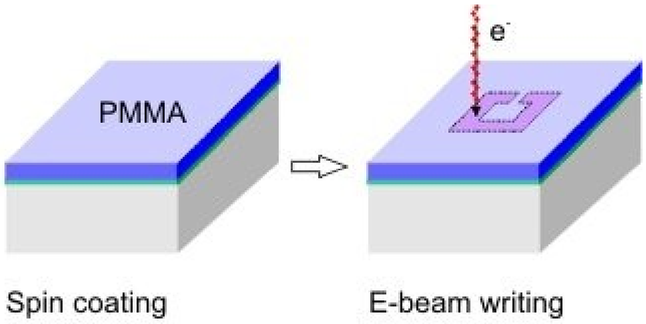

Figure 32 Spin coating of PMMA resist and successive electron beam writing on it.

Electron beam lithography breaks the polymer into fragments that are dissolved easily by a developer such as MIBK. This procedure is also analogous to the case of optical exposure in which a laser (or a strong light source) is used to break the polymeric bonds (Figure 33).

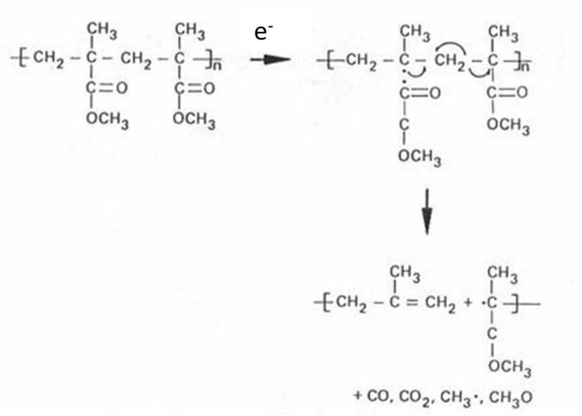

Figure 33 Mechanism involving the electron beam PMMA patterning. Electrons, interacting with the polymer chain, break C-C bonds separating the polymer in smaller region, then removed by the developer solution.

However, MIBK alone not only eliminates the irradiated fraction but also it damages the unexposed resist. Therefore, the developer is usually diluted with a weaker solvent, i.e. IsoPropilic Alcohol (IPA). A mixture of 1 part MIBK to 3 parts IPA produces very high contrast but low sensitivity. By making the developer stronger, say, 1:1 MIBK:IPA, the sensitivity is improved significantly with only a small loss of contrast. The developing step is then stopped immerging the sample in a IPA only solution.

The sample is finally annealed again in a post-bake process at 120°C for two minutes, in order to consolidate the PMMA bonding of the unexposed resist fraction.

By Electron Beam Lithography, therefore, we have patterned an array of nano apertures in PMMA. The EBL works in writing field of 100x100 μm^2. In each field we have fabricated both array of nominally 20 nm apertures, in a squared arrangement, with a pitch of 160 nm and a nominally 100 nm array of apertures, spaced 400 nm (Figure 34).

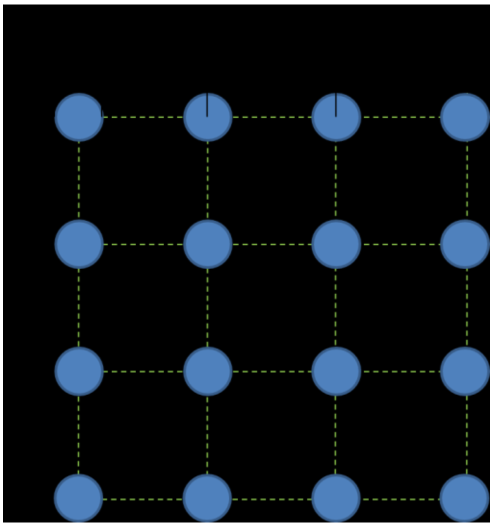

Figure 34 Schematic layout of the patterned template. An array of 100nm wide circular apertures have been fabricated with a pitch of 400nm. For the smaller 20nm wide aperture, an array with 160 nm pitch has been exposed.

The wider spacing in the 100 nm apertures prevents proximity effect due to the interaction of charge distribution of neighbor exposed regions. The writing field is finally repeated 100 times, to pattern a total square area of 1 mm^2. AFM Micrographs of the patterned PMMA resist are shown in Figure 35.

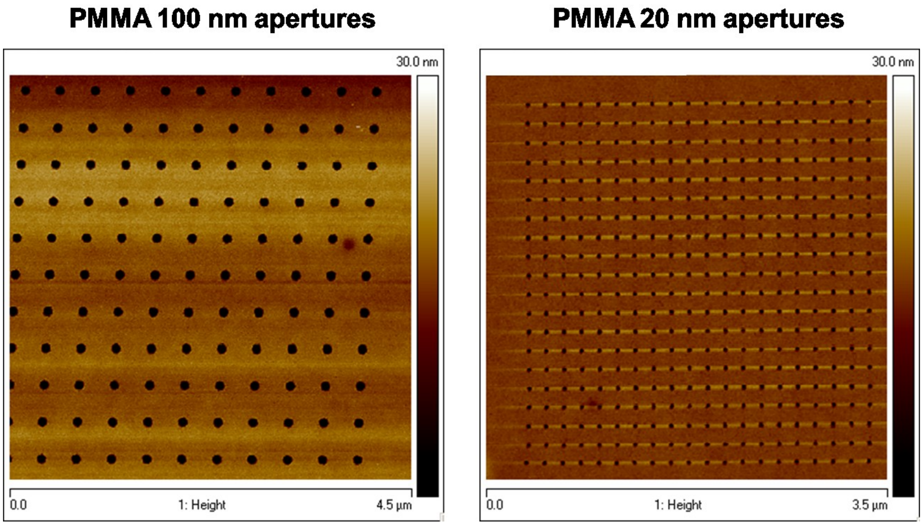

Figure 35 Atomic Force Micrographs of the 100nm wide apertures and 20nm wide apertures patterned on PMMA 950k.

AFM line scans performed on the samples reveal an effective aperture wideness of about 98 nm, while AFM measurements for the smallest apertures are heavily affected by the convolution with the AFM tip shape.

The unmasked regions were amorphized by irradiation of 40 keV Ge$^+$ ions at a fluence of 10^{14} at/cm^2. The ion energy was established by SRIM calculation [49] in order to take into account the energy loss in GST needed for complete amorphization and to stop the Ge$^+$ ions by the PMMA mask (Figure 36). Ion implantation was performed at LN$_2$ to reduce atomic mobility and then damage annealing (see 1.1) and to produce a sharper amorphous-crystalline interface. After implantation PMMA mask was removed using an Ar/O_2 plasma etching.

This etching step is required by the hard cross-linking of the resist polymer produced by ion implantation. Although, in fact, normally PMMA dissolves in Acetone, ion implantation establishes very strong bonds and removing the resist requires an aggressive physical etching. During this etching step, however GST is protected by the amorphous Silicon layer.

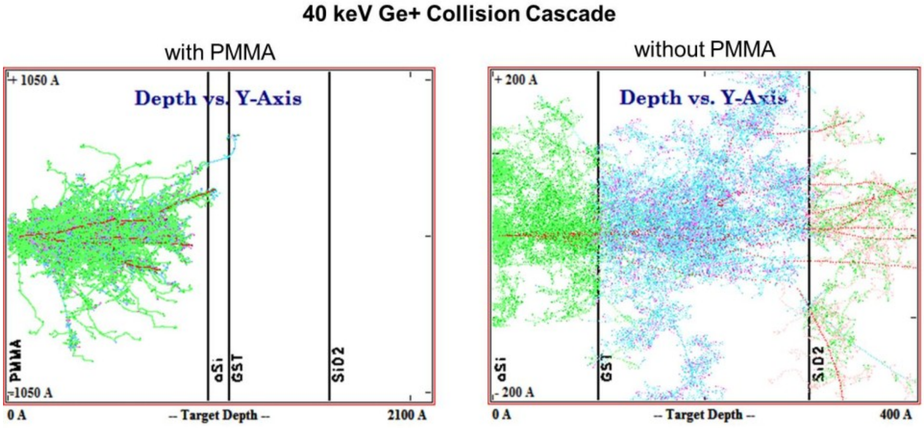

Figure 36 Collision Cascade of 40 keV Ge^+ in the sample described in the text: in the region with the PMMA resist and in the region under the apertures.

2.1.2 Nano pillars

In an as-deposited amorphous film, a pattern of dots, from 500 nm to 50 nm of diameter, were obtained by the EBL apparatus using a Hydrogen silsesquioxane resist (HSQ). HSQ is a negative resist, i.e. the radiation exposed fraction is cross-linked, while the remaining resist fraction can be etched by the developer.

HSQ is a monomer with a cubical-shaped molecule having one Si atom at each corner, with corners being linked via oxygen atoms. Its chemical formula is $H_8Si_8O_{12}$. It behaves like an off-stoichiometric Silicon Dioxide, especially for its passivation and breakdown voltage properties (see **Errore. L'origine riferimento non è stata trovata.**). HSQ is diluted in a solution with MBIK, with a percentage from 2% to 4%.

The resist is applied by spinning the solution at 5000 rpm for one minute. Then, we perform a bake process of two minutes at 120°C in order to eliminate the solvent. For the 2% HSQ solution we then obtain a 10-20 nm thick HSQ layer, while for the 4% HSQ solution the correspondent thickness is about 50 nm. Although, in a way of concept, a thinner layer permits to reach better resolution for a reliable etching result it is necessary to use a thicker resist, therefore the 4% HSQ solution has been used.

We fabricated circular pillar ranging from 50 nm to 500 nm in diameter arranged in a regular array, inserted in a writing field of 100x100μm^2. Next to each of this circular fields a star-shape, with body-size of few micron and a radius of curvature in the tips of about ten nanometers (Figure 37), was prepared, in order to study the crystallization of GST in a size-varying structures.

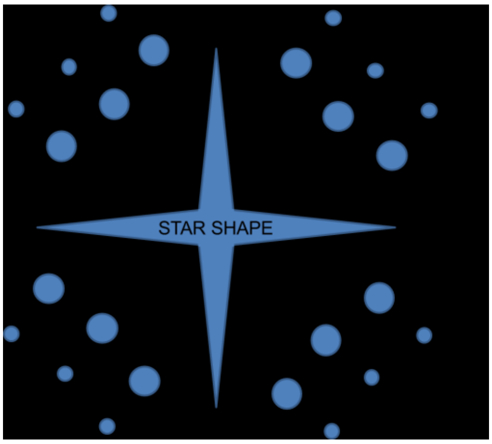

Figure 37 Schematic layout of the patterned template. Circular shapes ranging from 50 nm to 500 nm arranged in a regular array, together with star-shape structures was prepared.

The unexposed HSQ resin is then dissolved in a 4% solution of TMAH. After one minute, the developer action is stopped by immerging the sample in a IPA solution. In order to consolidate the exposed cross-linked area, the sample is then annealed at 120°C for two minutes.

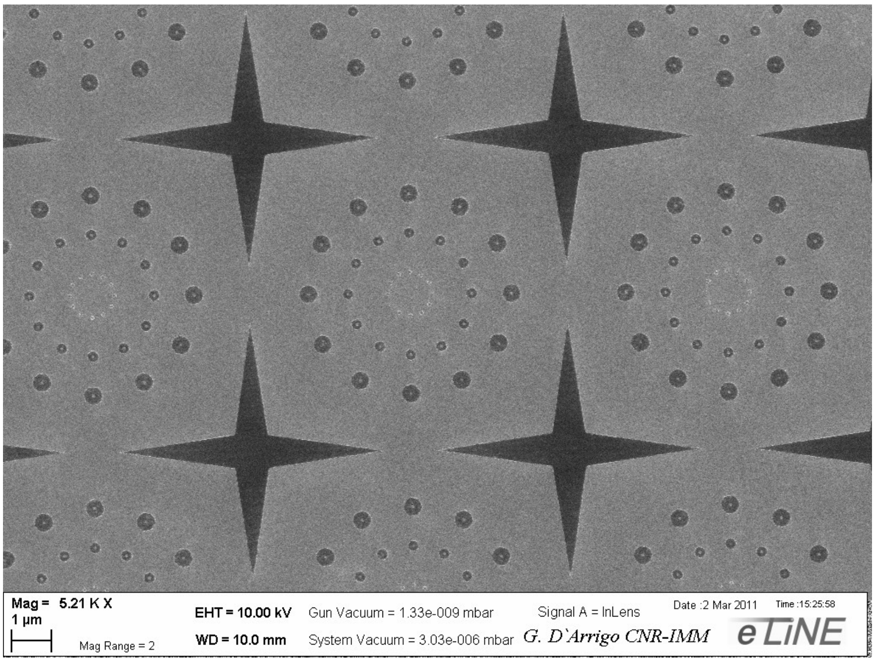

Figure 38 Scanning Electron Microscope Micrograph of the HSQ resist patterning.

The writing field is finally repeated 100 times, to pattern a total square area of 1 mm^2. To control the quality of the above mentioned processes, the HSQ patterning was verified at the Scanning Electron Microscope (Figure 38).

The GST film was etched by ICP. Different Etching Chemical Plasmas have been tried in order to obtain the optimal vertical anisotropic cutting. The gas available for the ICP was Ar, O_2, SF_6, CHF_3. At the beginning we have tried with a pure physical etching based on a plasma of Ar. However, for so small structures, the total absence of chemical component provides a too vehement process and the quality of the etching is very poor (Figure 39).

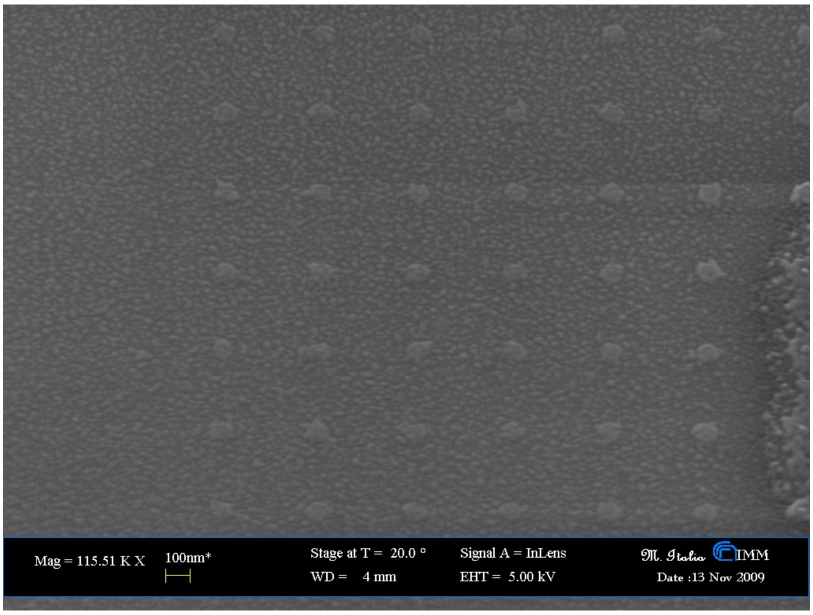

Figure 39 Shadow of 100nm Dot obtained by Ar-only ICP etching of a patterned HSQ over an aSi/GST/SiO2/Si film.

Then, we added O_2 and CHF_3 to Ar to enhance the chemical contribution. However CHF_3 as a big etching rate on $SiO_{2,}$ HSQ and GST. Therefore no suitable etching selectivity can be achieved with this gas combination. With this information, we have finally tried a combination of Ar, O_2 and SF_6. This gases are used normally in the etching of Si, in fact, they presents an optimal Si selectivity both with respect polymeric resist and SiO_2. The etching has been optimized using a pre-process composited by 30 sccm of Ar and 5 sccm SF_6 (chamber pressure 5E-3 mbar) with a RF power of 300W and no bias for 30 s, after this a plasma composited by 30 sccm of Ar, 2 sccm of O_2 and 40 sccm of SF_6 (chamber pressure 5E-3 mbar) with a RF power of 300W and 50 V bias is applied for 220 s. With these powers and fluxes we have obtained a good etching quality (Figure 40), although the GST:HSQ selectivity was about 1.

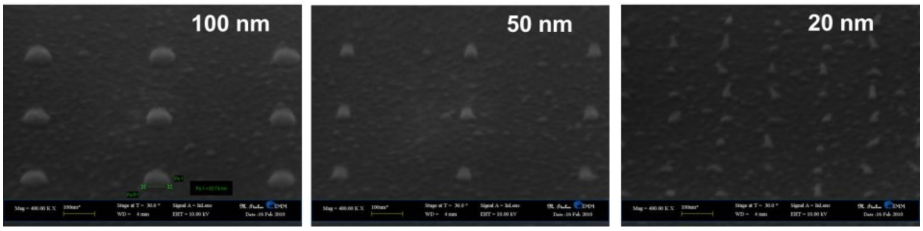

Figure 40 Patterning of GST with HSQ hard mask and an Inductively Coupled Plasma of Ar, O_2 and SF_6. Very good transferring quality has been obtained for feature size greater than 20nm.

This gas mixture, for isolated circular structures, is suitable until about 50 nm. For smaller dots, as the 20nm wide shown, the etching quality decreases and good structures are found only statistically. For other geometries, this limit can be further lowered. As we will show in the next chapter, in fact, for line geometries we can obtain a wideness as small as 25 nm.

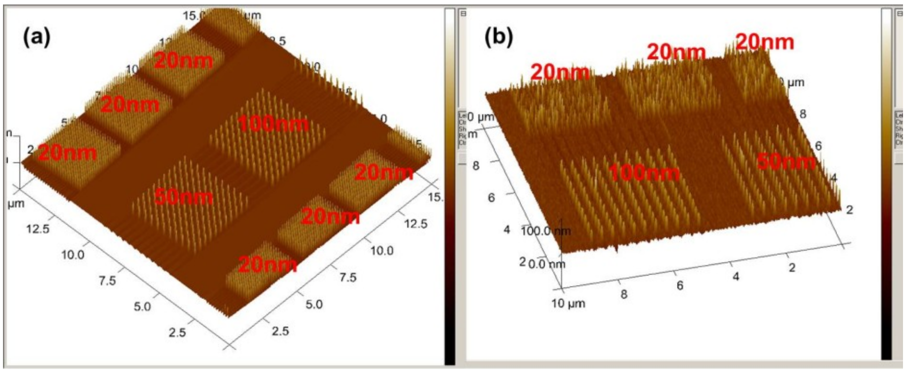

Figure 41 Atomic Force Microscopy (AFM) performed on the (a) HSQ hard mask and (b) in the patterned GST. Very good transferring quality has been obtained for feature size greater than 20nm

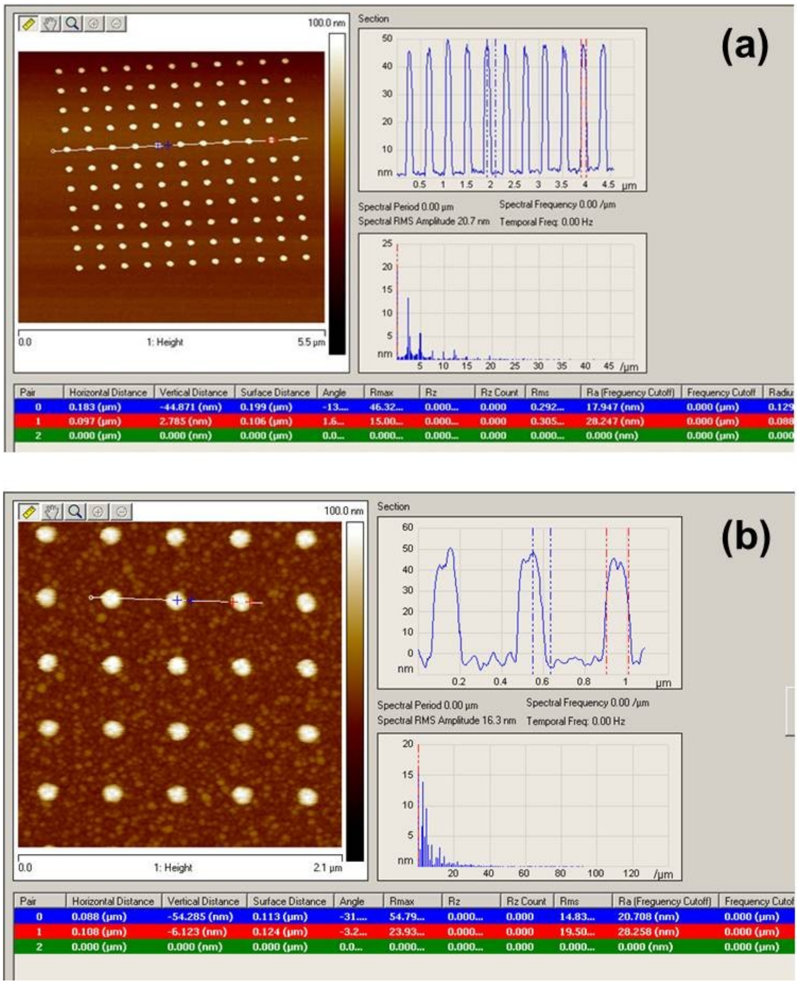

Pair	Horizontal Distance	Vertical Distance	Surface Distance	Angle	Rmax	Rz	Rz Count	Rms	Ra (Frequency Cutoff)	Frequency Cutoff	Radiu
0	0.183 (µm)	-44.871 (nm)	0.199 (µm)	-13....	46.32...	0.000...	0.000	0.292...	17.947 (nm)	0.000 (µm)	0.129
1	0.097 (µm)	2.785 (nm)	0.106 (µm)	1.6...	15.00...	0.000...	0.000	0.305...	28.247 (nm)	0.000 (µm)	0.088
2	0.000 (µm)	0.000 (nm)	0.000 (µm)	0.0...	0.000...	0.000...	0.000	0.000...	0.000 (nm)	0.000 (µm)	0.000

Pair	Horizontal Distance	Vertical Distance	Surface Distance	Angle	Rmax	Rz	Rz Count	Rms	Ra (Frequency Cutoff)	Frequency Cutof
0	0.088 (µm)	-54.285 (nm)	0.113 (µm)	-31....	54.79...	0.000...	0.000	14.83...	20.708 (nm)	0.000 (µm)
1	0.108 (µm)	-6.123 (nm)	0.124 (µm)	-3.2...	23.93...	0.000...	0.000	19.50...	28.258 (nm)	0.000 (µm)
2	0.000 (µm)	0.000 (nm)	0.000 (µm)	0.0...	0.000...	0.000...	0.000	0.000...	0.000 (nm)	0.000 (µm)

Figure 42 Height measurement performed by AFM on 100nm wide dot (a) before plasma etching and (b) after. Similar height values (≈50nm) have been found in both the cases, indicating that the etching process has a HSQ:GST selectivity ≈1.

Pre-bake and Post-bake of the resist was performed at about 150°C for few minutes. To re-amorphize the GST, the sample was implanted by 130 keV Ge^+ ions at a fluence of 10^{14} at/cm^2 at room temperature (RT).

Transmission electron microscopy, and plan-view configurations, was performed using a JEOL JEM 2010F TEM equipped with a 200-kV Schottky field-emission electron gun, and an ultra high-resolution objective lens pole piece.

The nano-structured films were prepared for the plan-view observation by the combined use of mechanical polishing and CP4 chemical etching. *In situ* TEM analyses were performed using a Gatan 626TA single tilt heating holder equipped with a 901 SmartSet Hot Stage controller to maintain the temperature to the set-point (within ±1 °C) without overshoot.

2.2 Ion Beam Implantation in nano-apertures

Ion implantation in blanket continuous film implies heterogeneous random overlapping of collision cascades, i.e. ion damage density function is the same over all the film. When we perform an implantation along a masked film, however, the aperture geometry produces a different ion and damage distribution at the edge of the window with respect to the inner parts (Figure 43).

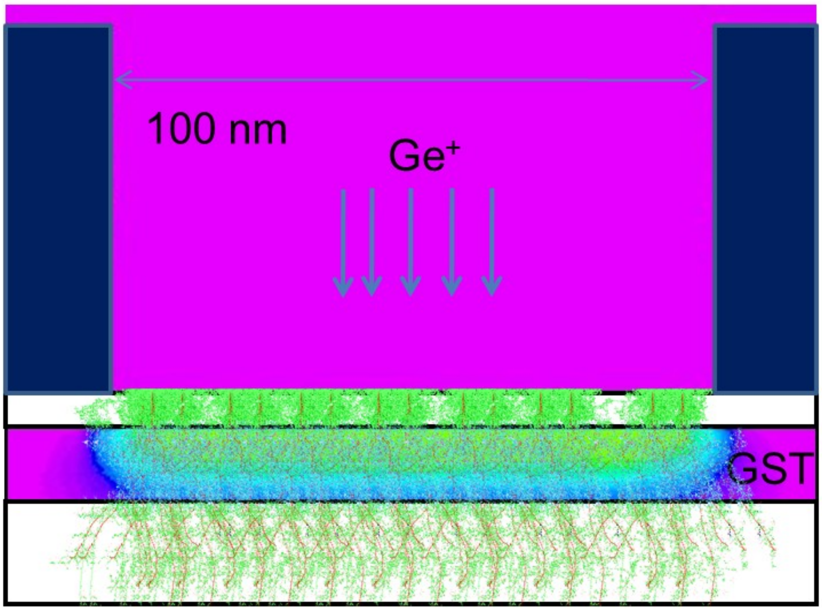

Figure 43 Ge+ Collision Cascades on an aperture of 100nm. At 40 keV each cascade has a straggling of about 9nm on GST.

In particular, damage is reduced at the edge of the mask because cascade overlapping contribution from ion impinging the masked area is missed. Assume a circular aperture with raidus r. If $\sigma \ll r$, one can easily proves that the damage at the edge is about the 50% respect the damage at the center of the aperture (that is the same produced by the same implantation in a blanket film). Generally, however, one must solve the problem numerical, being the damage in a point $\vec{r}$ of the sample:

$$f(\vec{r}) = k \int_{A_{aperture}} e^{-\frac{(\vec{r}-\vec{R})^2}{2\sigma^2}} d\vec{R}^2$$

with

$$k^{-1}D_{blanket} = \int_{A_{blanket}} e^{-\frac{(\vec{r}-\vec{R})^2}{2\sigma^2}} d\vec{R}^2$$

where $D_{blanket}$ is the damage produced by the same implant in a blanket film.

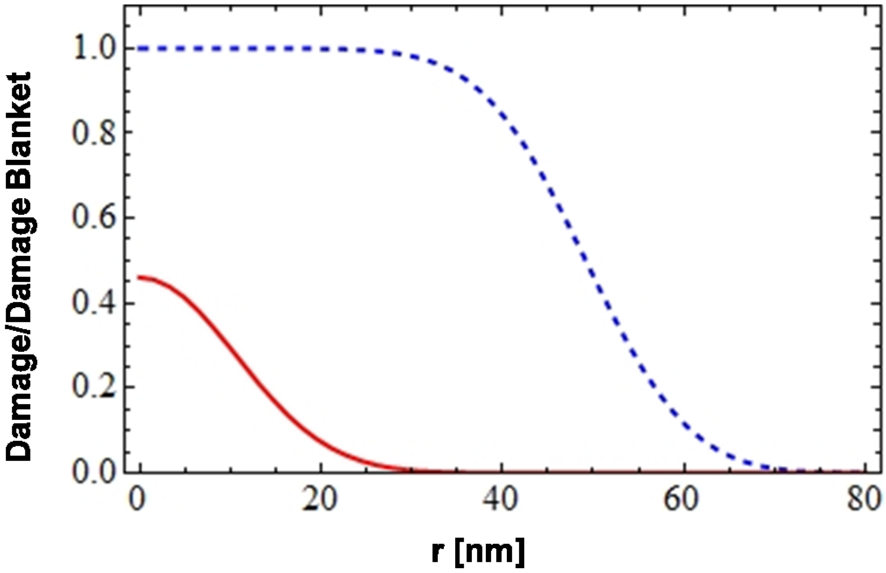

Figure 44 Damage of GST under an aperture with respect to the damage in a blanket GST film, produced by 40 keV Ge+ for a 100nm wide aperture (dotted blue line) and for 20nm wide aperture (solid red line). In the calculation, a damage straggling of 9nm is assumed.

In Figure 44 one can notice the difference for the damage profile produced on a circular aperture for an implant of Ge^+ at 40 keV in apertures of 100nm (blue dotted curve) and 20nm (red curve). The straggling produced by this kind of implantation is about 9nm. For this reason in the case of the larger aperture, where $\sigma \ll r$, the damage at its center is almost equivalent to that one produced by the same implantation in a blanket film, while at the edge it reduces to the 46%. Otherwise in the smaller aperture the radius and the straggling are comparable and the damage at the center of the structure lower to about 46%. Damage at the edge is about 29% and, therefore, a judicious choice of the implantation parameter (Energy, dose and temperature) must be taken into account in order to obtain amorphization in this case.

2.3 In situ annealing of nano amorphous structures by Transmission Electron Microscopy

2.3.1 Embedded nano amorphous regions

2.3.1.1 Sample Preparation

After the ion irradiation of the masked GST film described in 2.1.1, the sample is prepared for TEM observation. The usual TEM sample preparation for plan-view micrograph consists of several polishing step to reduce the sample to a disk of nominally 3.0 mm diameter and thick, in the region of TEM observation, less than 150 nm. In the first step an ultrasonic cutter is used for stamping a circular disk from the surface of the sample. The disk, about 3 mm in diameter and 200 μm thick, is only obtained grinding down the surface, from a specimen thick about 600 μm. An alignment procedure is followed in this step, in order to maintain the patterned region at the center of the disk. Since the grinding doesn't cross all the sample thickness, the disk remains attached to the rest of the sample. The sample is then attached, from the patterned surface, to a cylinder (1/2 inch diameter) to mechanical polish the back until its thickness is about 70 μm. Normally, this attachment is obtained using a thermoplastic resin, at a temperature of about 150°C. Unfortunately, amorphous GST crystallizes at this temperature and, therefore, ciano-acrylate glue has been used, in order to attach the sample at room temperature. Once the sample is mechanical polished the disk is completely detached from the rest of sample (since the previous grinding was 200 μm deep). At this point a dimpler is used in combination with an abrasive paste with 3 μm wide SiC component, in order to reduce the back thickness (in the central part of the disk) to about 30 μm.

Normally, at this point, for blanket chalcogenide film we use ion milling at very low energy, about 3 keV. Although, in fact, for any other common semiconductor, e.g. silicon, the milling energy can be increased up to about

5 keV, the samples can reach about 200°C [63]. The lower energy of 3 keV, for blanket amorphous film, is instead high enough to polish completely the 30 μm in about 1 hour and to maintain the sample temperature low enough to avoid crystallization. Although this procedure is quite fine for blanket amorphous samples , however, when we applied it to our nano amourphous samples we observe completely crystallized areas, as shown in Figure 45, both for (a) 100nm circular areas and for (b) 20nm ones.

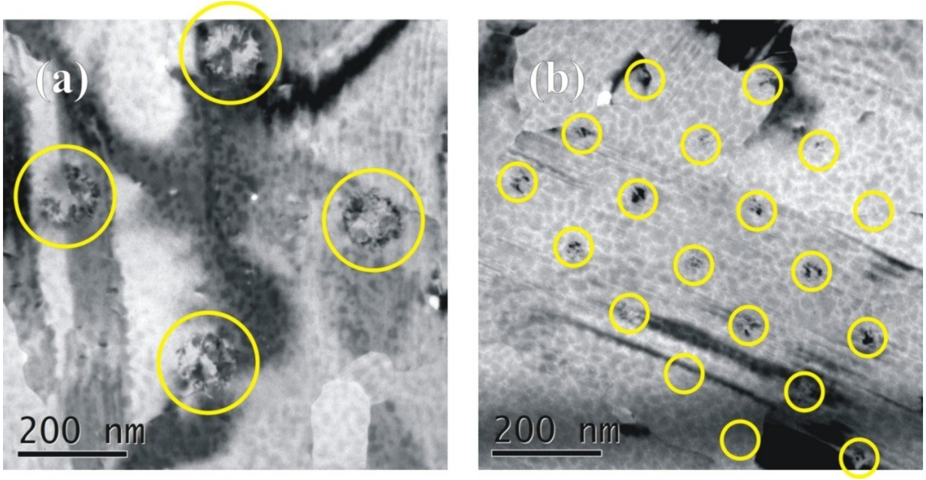

Figure 45 High contrast crystalline circular region, after a 3keV ion milling in Ar.

Therefore, we used a room temperature chemical polishing using a CP4 solution (1 HF : 4 HNO_3). CP4 Solution has a good Si:SiO_2 etching selectivity. The sample was immersed in the solution for several second, controlling by transmission optical microscope the presence of Si and, if any, repeating the immersion until silicon disappears. It is very important to control step by step the presence of silicon and stop the procedure when it vanishes in the thinnest region: GST film would dissolve for several microns if in contact with the solution; chalcogenides, in fact, presents a very high etching rate with the aggressive CP4 solution.

At the end of the process, in the thinnest region of the disk (that is in the central part of it, where we positioned the patterned region in the first step) the sample is about 130 nm thick (100nm SiO_2 + 20nm GST + 10nm amorphous Silicon) and it is then ready for the TEM observation.

As shown in Figure 46, completing the thinning procedure by CP4 wet etching, the amorphous nano regions are preserved.

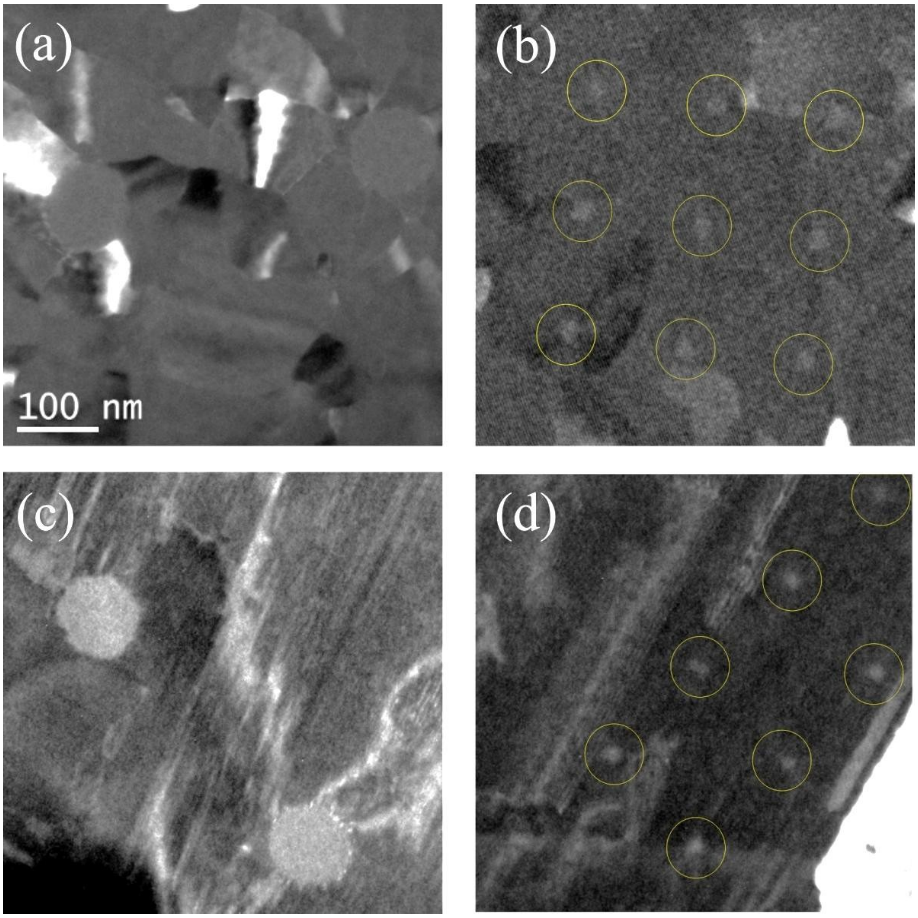

Figure 46 TEM micrographs (dark field) of nano amorphous regions of GST embedded in its fcc (a, b) and hcp (c, d) phase. In (a) and (c) the diameter of the regions is about 100 nm

while in (c) and (d) the diameter is nominally 20 nm. All the nano regions are clearly in the amorphous phase using the CP4 wet etching described in the text.

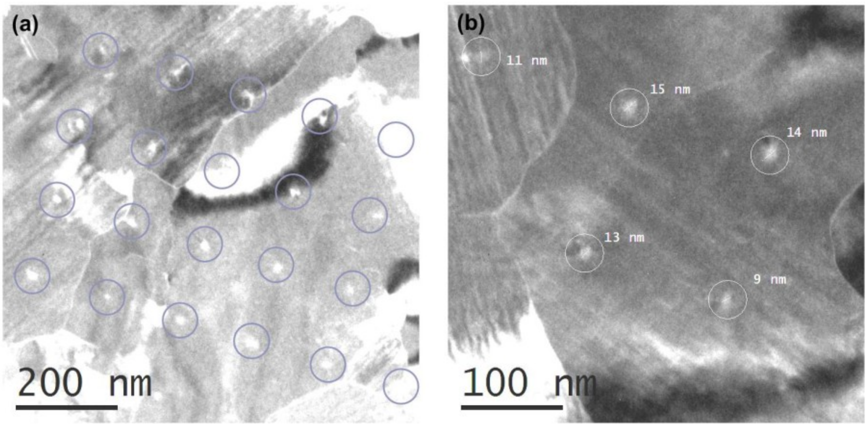

Figure 47 (a) An array of nominally 20nm amorphous regions; (b) an insight of the real size distribution of the structures in (a).

In Figure 47 an insight in the nominally 20 nm amorphous regions is shown. In particular, in (b), we observed that, at this small dimensions, the dots are not identical but they are distributed in size from from 9 nm to 15 nm in diameter. This issue can be ascribed to two different causes. First, differences in the PMMA mask apertures can occur, since we work with conditions quite close to the resolution limits of the system PMMA/EBL. At 20 keV, the lithography beam, nominally 2nm wide, spreads to about 100 nm of PMMA. Bonds in the resist can be broken statistically, according to the energy they receive. Second, as we have observed in paragraph 2.2, ion implantation in such small apertures is reduced respect to the nominal dose of about 30%, at the boundaries of the mask aperture. Moreover, since at a fluence of 10^{14} at/cm^2 about 350 ions fall in a 20 nm aperture, the system is heavily subjected to the statistics of the incident ion distribution along the specimen surface.

2.3.1.2 Measurements

In the hcp case, the a-c interface moves at expense of the amorphous phase, starting with a defective crystalline layer. In Figure 48 the amorphous regions have been shown as a function of time, for an annealing at 90°C. In the initial step, a defective crystalline layer emerges, as observed in the figure (t=900s). During the creation of this layer the a-c interface moves faster (6.4 pm/s) with respect to the remaining recrystallization process (1.7 pm/s). This last value is very close to that one found for a corresponding amorphous-in-fcc dot with the same size, that was 1.1 pm/s.

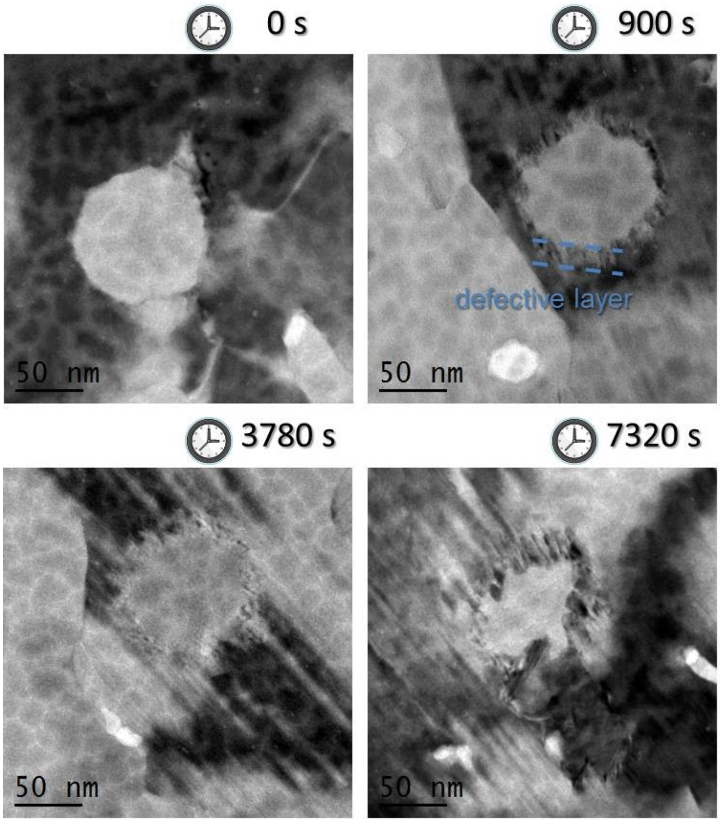

Figure 48 Plan-view TEM micrographs (bright field) of amorphized dot (100 nm) surrounded by hcp phase during in situ isothermal annealing at 90°C. Crystalline regrowth from the rim of the dot has been observed.

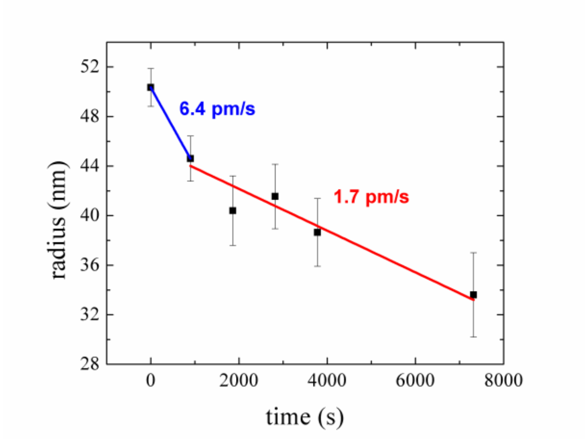

Figure 49 Time dependence of the average radius of several 100nm-wide amorphous regions at 90°C, embedded in hcp phase.

For the amorphous dots in hcp the same measurement is repeated at 75°C. In this case we found a growth velocity of 0.58 pm/s in the first step and 0.14 pm/s in the remaining process (Figure 50).

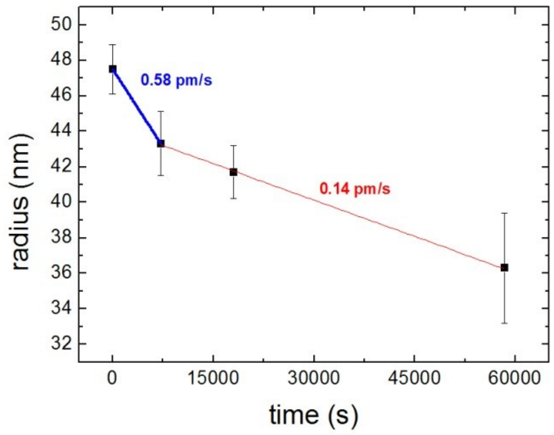

Figure 50 Time dependence of the average radius of several 100nm-wide amorphous regions at 75°C embedded in hcp phase.

At each temperature, 10÷20 grains are analyzed, and the radius value reported in the figure is an average of the measured values, while the bar indicates the spread between the value distribution (standard deviation). One should notice that distribution spreads with time, indicating a different behavior of each grain. This means also that the different growth velocities had due probably to the random orientation of the surrounding crystalline grains.

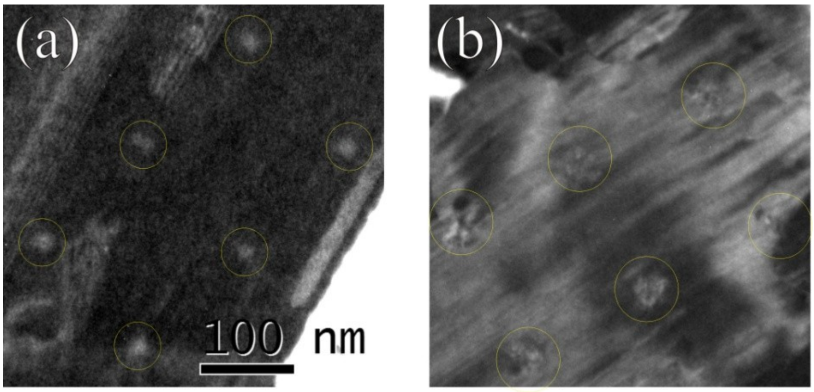

Figure 51 Plan-view TEM micrographs (dark field) of 20 nm-wide dot surrounded by hcp phase (a) as prepared (amorphous) and (b) after 2h at 75°C. In (b) the area is crystallized.

In Figure 51, an array of 20 nm amorphous regions embedded in hcp phase, before (a) and after an annealing at 75°C is shown. The isothermal annealing was 2 hours long. According to the velocity estimation in Figure 50, the growth rate at this temperature should be 0.58 pm/s during the faster regime, and so after the annealing a reduction of about 8.4 nm should occurs for the diameter of the spot. This should permit the re-crystallization of the smallest dot (9 nm wide according to Figure 47). However every dot appears crystalline after the annealing (Figure 51b) and this could mean that a size dependent growth rate occurs during re-crystallization.

Also, since the steady state re-crystallization velocity, measured in a 100nm amorphous regions at the same temperature, is about 0.14 pm/s (Figure 47), the estimated amorphous region should crystallize in about 8 hours. It is relevant the investigation of retention in a small system with dimension and in structures similar to that one present in a real device.

In Figure 52 we have reported the growth velocity measurements performed on 100nm amorphous regions embedded in the fcc crystalline phase at 180°C. At each time, the radius value has been measured for the same dots, indicated in the figure as dot 1, dot 2 and dot 3. By circular area approximation, growth velocities of $1.1 \pm 0.5\, pm/s$, $9.0 \pm 1.0\, pm/s$ and $10 \pm 2\, pm/s$ have been obtained for annealing at 90°C, 100° and 110 °C respectively.

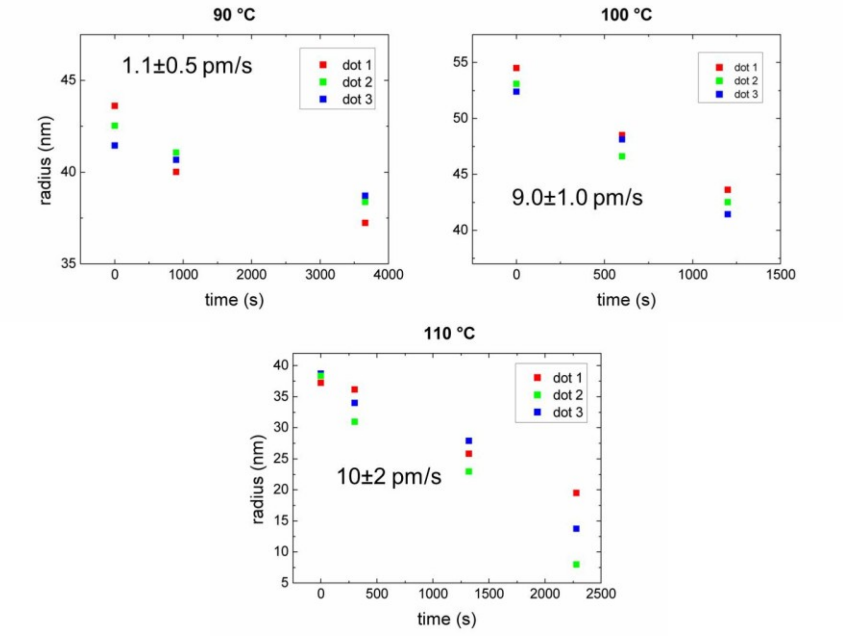

Figure 52 Time dependence of the average radius of several 100nm-wide amorphous regions at 90°C, 100°C and 110°C, embedded in fcc phase. The fcc phase was obtained by an amorphous GST film annealed at 180°C for 10 minutes.

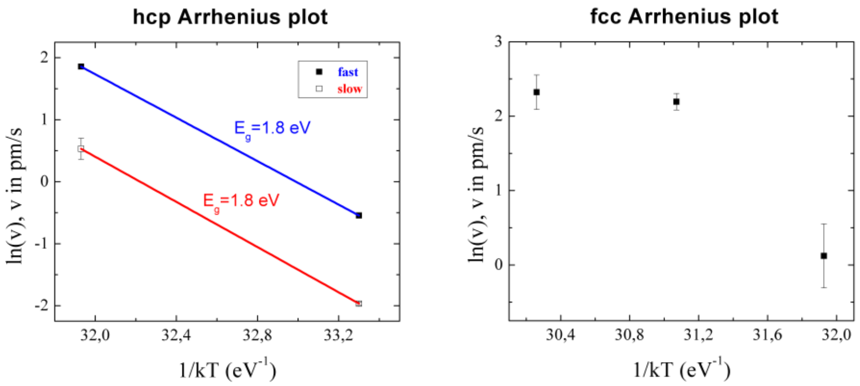

Figure 53 Arrhenius plot of the growth velocity of the amorphous-crystalline interface for 100nm amorphous region embedded in hcp crystalline phase (left) or in fcc crystalline phase (right). The two crystalline films had been obtained annealing an amorphous GST film at 180°C (fcc) and 350°C (hcp).

In Figure 53 the Arrhenius plot of the growth velocity for 100nm amorphous region either embedded in hcp or in fcc crystalline is shown. For the hcp phase, the same activation energy $E_g = 1.8\,eV$ has been found for the growth velocity measured in the initial faster regime and in the subsequent slower one.

We have also fabricated amorphous 100 nm wide regions in a polycrystalline fcc GST film. This sample has been annealed at higher temperatures (110°C and 120°C) in order to compare their growth velocity with those measured in a as sputtered blanket amorphous film.

The film were covered with 10 nm of aSi and prepared it with the same procedure described above. The measured growth velocities were $1.1*10^{-2}$ nm/s and $6.6*10^{-2}$, at 110°C and 120°C respectively. These values are about 5 times the values obtained by Kalb et al. [13] for an as sputtered amorphous GST film annealed at the same temperatures.

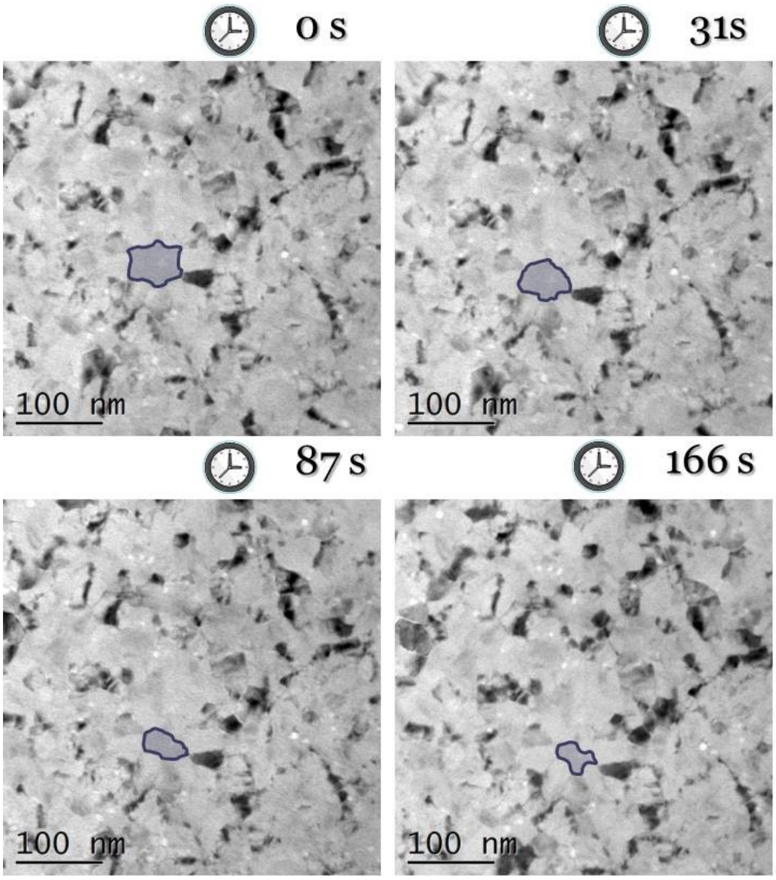

Figure 54 Plan-view TEM micrographs (bright field) of amorphized dot (100 nm) surrounded by fcc phase during in situ isothermal annealing at 120°C.

The correspondent value of 2.3 eV obtained for the activation energy of the growth process is also well comparable with that one obtained by Kalb (2.35 eV), indicating that similar mechanisms are involved in the process.

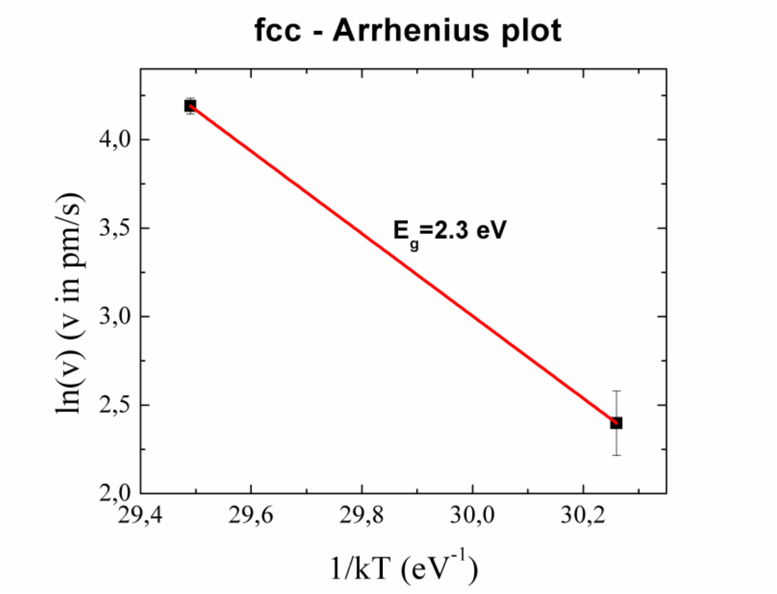

Figure 55 Arrhenius plot of the growth velocity of the amorphous-crystalline interface for 100nm amorphous region embedded in a fcc crystalline phase. The crystalline film had been obtained directly during sputtering deposition.

The difference found in the absolute value of the velocities can be ascribed to several issues. First of all, as discussed in the previous chapters, ion implanted amorphous chalcogenide characteristics are closer to melt-quenched and so its crystallization kinetics is enhanced with respect to the as deposited specimen. In addition deposition method and stoichiometry [69] and interfaces can play a relevant role. Finally, The observations so far presented are based mainly on TEM, which requires high energy electron irradiation. Particular attention should be then paid to the effect on the crystallization kinetics of exposure to electron beam.

In Figure 56, we show what happens to an amorphous blanket film of GST, after an annealing of 8 min at 145°C (a) and with the same annealing condition if the electron beam (b) was previously focalized on it. During both the annealing processes the beam was switched off.

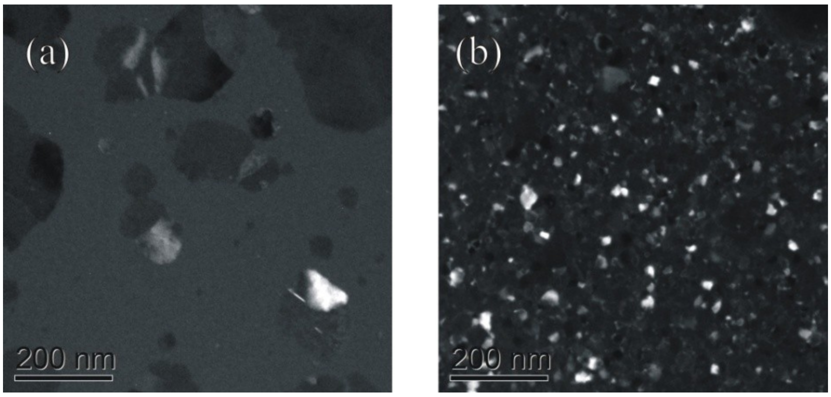

Figure 56 Dark Field: GST samples annealed for 8 minutes at 145°C (a) without any previous TEM observation (b) focalizing the electron beam before the observation. In both cases, electron beam was switched off during annealing.

Crystallization kinetics enhancement for the effect of electron beam irradiation is clear from the comparison of images (a) and (b). In (a) nucleation and growth are taking place and the crystal phase (high contrast) partially covers the surrounding amorphous phase (grey flat contrast). In (b) crystalline phase covers the whole surface. Also the size distribution of the crystalline grains is very different in the two case, being the average grain size in (a) much larger than (b), although in (a) crystallization process is not yet completed.

We can approximate the nucleation rate in Figure 56a as

$$I = \frac{N}{A \cdot t \cdot s} \qquad (2.1)$$

where N is the grain number, A is the observed Area, t is the annealing time and s is the film thickness. Since the crystallization fraction is quite small, $\chi \approx 0.3$, we can neglect the reduction of the amorphous region during the annealing. Substituting $N = 53$, $A = 0.648\ \mu m^2$, $t = 480\ s$ and $s = 20\ nm$ we obtain $I = 8.5 \cdot 10^{12}\ cm^{-3}s^{-1}$, that corresponds to a temperature of about 137°C for an as sputtered GST film [14]. The difference in temperature (145°C vs. 137°C) may be due to calibration, to the incubation time not considered in this estimation and finally to the absence of free surfaces in the present observation (amorphous silicon layer could reduce the nucleation rate with respect to a free surface film). Also, if we assume, as an estimation, that the number of crystalline grains doubles at the end of the crystallization process, the final grain concentration ($160\ grains/\mu m^2$) is the same of an annealing at 145°C for an as sputtered sample [33]. In the case of the electron beam irradiated sample, instead, the grain concentration at the complete crystallization was $2030\ grains/\mu m^2$, which corresponds to an annealing at $\approx 215\ °C$ for an as sputtered samples.

Exposure to the electron beam, therefore, clearly influences GST crystallization behavior. For this reason, during *in situ* annealing we have always switched off the electron beam. Moreover, observations have been performed avoiding beam focalization. If possible, after annealing we have analyzed unexposed specimen region, using a statistical approach to elaborate our data.

Nevertheless, focused electron beam can be used to produce, separately and in a controlled way, nucleation or growth in chalcogenide specimens.

Figure 57a shows a 100nm wide amorphous region surrounded by the crystalline phase before focalizing the electron beam (≈4 nm) for about 300 s on its center. (b) After this exposure, crystalline grains appear in the irradiated area (indicated by the blue circle) while the external region is only slightly affected. Again, using Equ. (2.1), assuming that the electron beam produces only a thermal effect on the sample, a lower limit for the local temperature of 170°C can be estimated, based on the nucleation rate of an as sputtered film.

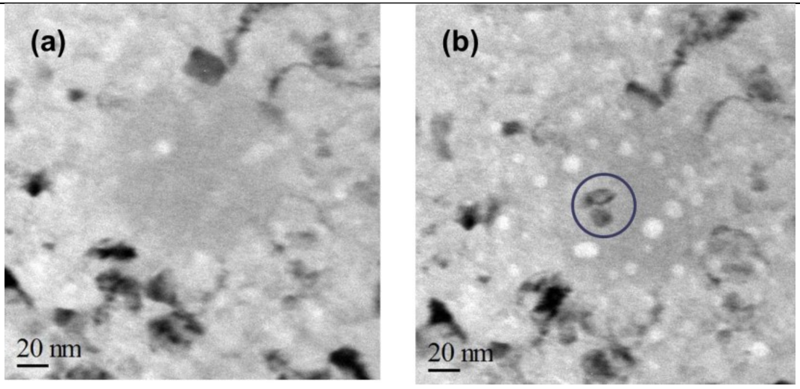

Figure 57 Amorphous dot in a fcc sample (a) and (b) after irradiation with an electron beam spot of about 4 nm on the central region. The presence of crystalline grains in the electron irradiated area is evidenced by the circle.

In Figure 58a shows a 100nm wide amorphous region surrounded by its hcp crystalline phase before irradiation with a focused electron beam (≈4 nm) for about 300 s on its boundary. (b) After this exposure, crystalline surrounded phase growth at expense of the amorphous phase (emphasized by the blue circle) while no nucleation process takes place inside the amorphous region. One can also note that, while in the case of isothermal annealing in the same condition the crystallization begins with the creation of a defective crystalline layer (Figure 49), in this case there is no evidence of defects, the crystallization growth seems to proceed in a epitaxial way. The growth boundary region in the figure is about 40nm, which justifies an average velocity of $\approx 1.3 \cdot 10^{-7} cm/s$. This value, compared with that measured in as sputtered GST films, indicates a temperature of $\approx 147\ °C$. Since the irradiated area was only 4nm wide, a factor ten smaller than the crystallized area, the calculated temperature represents a lower estimation.

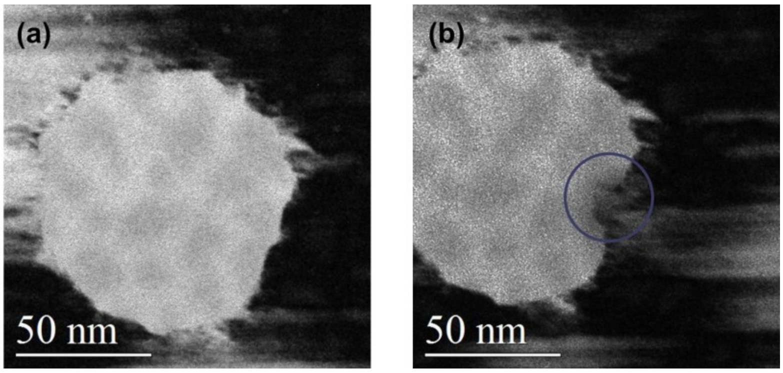

Figure 58 TEM micrographs of amorphous dot in a hcp crystal (a) and (b) the same area after 30s of focused electron beam (about 4 nm) exposure at the a-c interface. The epitaxial growth from the interface is evidenced by the circle.

2.3.1.3 Amorphization of nano regions: future perspective

In the latest section we have discussed the use of ion implantation to create nano amorphous regions in GST, establishing a condition close enough to that one present in the active regions of most devices. This procedure permits the study *in situ* of the crystallization of small structures, hardly accessible in other way. Although the size of the fabricated regions is comparable to the smallest active areas in the present device further improvements can be applied to the experimental setup to produce smaller amorphous areas.

As an example, the use of Focused Ion Beam (FIB) permits the maskless amorphization (by Ga^+ ion implant) of thin films in micron (submicron) regions. In particular, the absence of resist eliminates the beam spreading due to electron-resist interactions and any residual resist, affecting the TEM observation. Ar/O_2 plasma etching is, in fact, hardly able to entirely remove the PMMA resist and residuals can remain in the TEM sample noising the imaging contrast and producing undesirable carbonization during electron beam exposure.

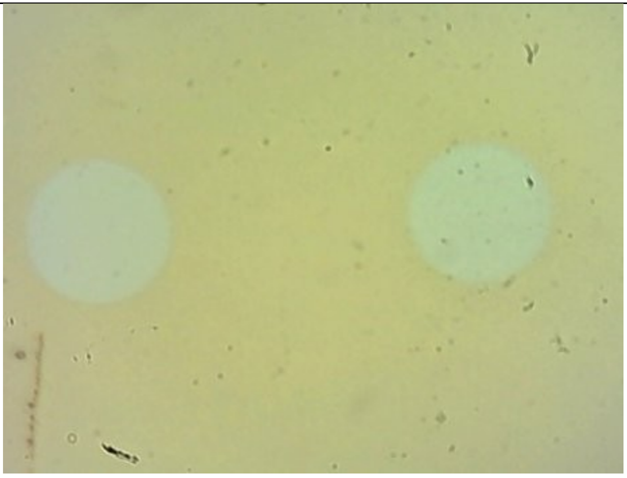

Figure 59 Optical Microscopy of two 20 μm amorphous dots produced by a FIB 200DE FEI with Ga^+ at an energy of 30 keV and fluence 10^{14} ions/cm^2. Optical observation is possible due to the huge optical contrast between amorphous and crystalline phases.

In Figure 59 shows two 20 μm amorphous dots produced by a FIB 200DE FEI with Ga^+ at an energy of 30 keV and fluence 10^{14} ions/cm^2. The implanted regions are well-visible by optical microscopy due to the high optical contrast between amorphous and crystalline phases.

By Atomic Force Microscopy (AFM) we can distinguish amorphous areas by their density change with respect to the crystalline phase. As shown in Figure 60, for dots of 1 μm in diameter, the change in thickness is about 1 nm on a 20 nm thick crystalline film corresponding to 5% of density change, well in agreement with the data reported in the literature [68].

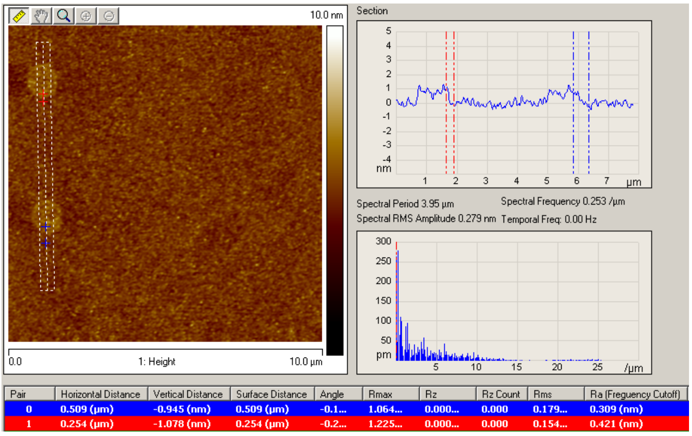

Spectral Period 3.95 µm
Spectral Frequency 0.253 /µm
Spectral RMS Amplitude 0.279 nm
Temporal Freq: 0.00 Hz

Pair	Horizontal Distance	Vertical Distance	Surface Distance	Angle	Rmax	Rz	Rz Count	Rms	Ra (Freguency Cutoff)
0	0.509 (µm)	-0.945 (nm)	0.509 (µm)	-0.1...	1.064...	0.000...	0.000	0.179...	0.309 (nm)
1	0.254 (µm)	-1.078 (nm)	0.254 (µm)	-0.2...	1.225...	0.000...	0.000	0.154...	0.421 (nm)

Figure 60 AFM of 1 µm wide circular dot. The enhancement in thickness is about 1 nm on a 20 nm thick crystalline film

Finally, in Figure 61, we report a 1 µm wide FIB amorphized spot. The flat grey contrast in the circular area clearly indicates its amorphous phase with respect to the surrounding (hcp) crystalline environment.

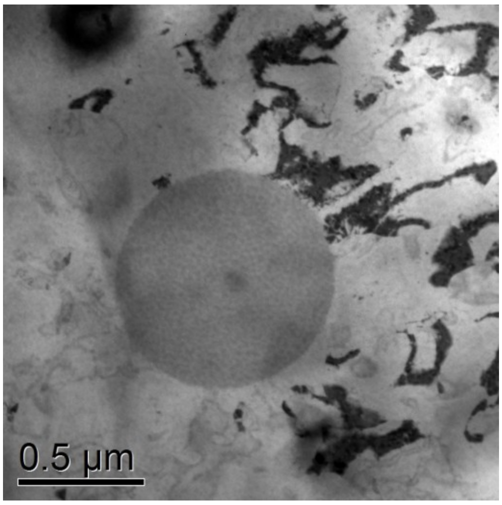

Figure 61 TEM Micrograph (bright field) of 1µm amorphous region produced by Focused Ion Beam with 10^{14} Ga^{+}/cm^{2} at an energy of 30 keV.

2.3.2 Isolated nano amorphous pillar

After GST patterning described in (2.1.2) samples have been prepared followed the TEM procedure at room temperature presented for the nano-apertures (i.e. ciano-acrylate attachments, CP4 final etching). However, since the HSQ e-beam lithography requires a bake and a pre-bake in a temperature range between 120°C and 150°C, after patterning the sample is completely crystallized (Figure 62).

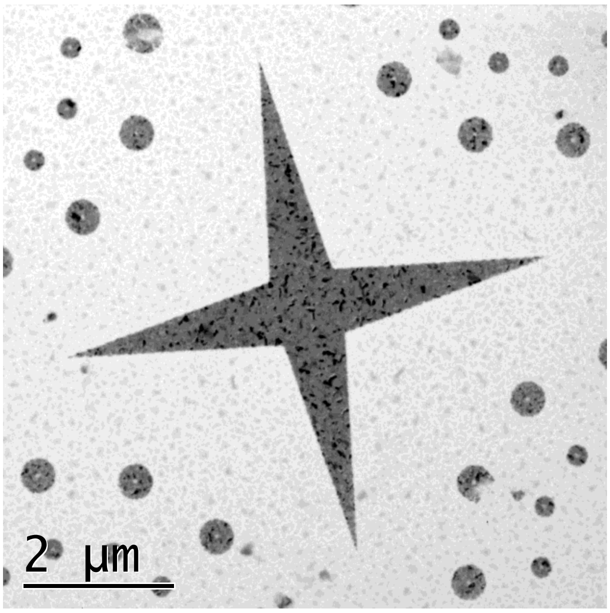

Figure 62 Plan-view TEM micrographs (bright field) of the star-shaped structure without performing ion implantation. Sample manipulation for HSQ-EBL patterning requires annealing processes over the crystallization temperature of GST.

Since we want to study the crystallization of these isolated structures an amorphization step is required. As in the previous case we perform ion implantation to amorphize the GST.

Comparing the AFM images, before and after etching, we can assume, as a conservative estimation, that the etching leaves 30nm of HSQ and 10nm of amorphous Silicon over the GST pillar (compare Figure 42). To amorphize GST with a nearly homogeneous energy loss across the interested thickness, implants were performed with 10^{14} at/cm^2 of Ge^+ at an energy of 130 keV.

As shown in Figure 63, after implantation micrograph presents a totally flat grey contrast, indicating the complete amorphization the structures, as confirmed by Selected Area Diffraction (SAD).

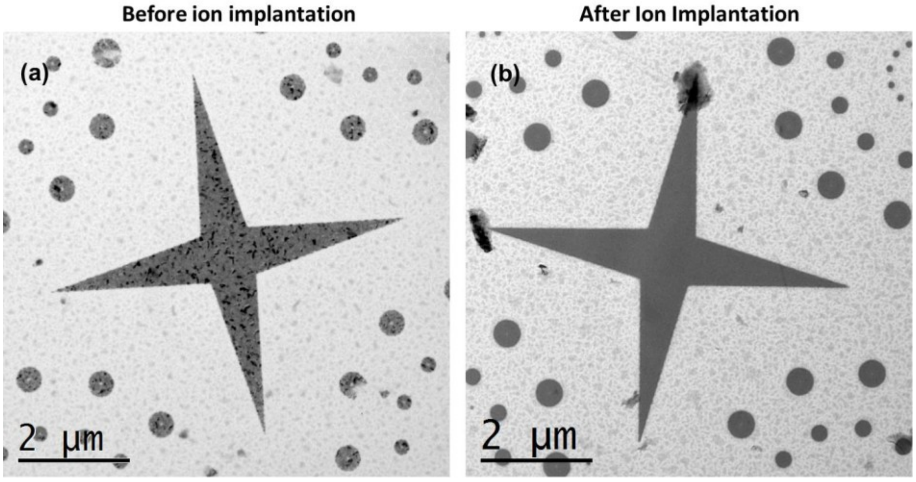

Figure 63 Plan-view TEM micrographs (bright field) of the star-shaped structure (a) before performing ion implantation.and (b) after. In (b)the GST regions present a totally flat grey contrast, typical of amorphized structures.

Isochronal annealing temporal steps of 10 min were performed, from 90°C to 150°C with temperature steps of 5°C. At the end of each step, TEM observation was performed in a large region of the sample, including tens of dots, by means of bright and dark filed images and SADs.

Crystalline grains appear already at 130°C (Figure 64), but they cannot be attributed to $Ge_2Sb_2Te_5$ because in the following annealing steps they don't show any evident growth. Therefore, they probably arised from different stoichiometry alloys produced locally, at the edge of each structure, by the plasma etching.

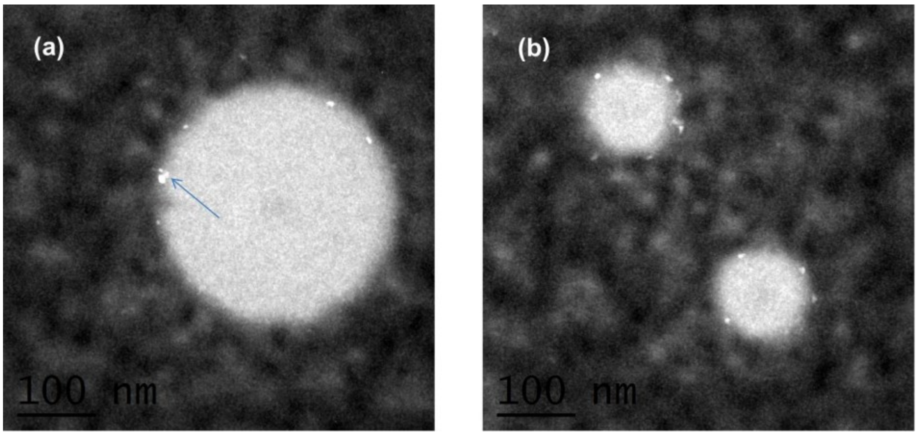

Figure 64 non-GST Crystalline grains in the boundary of the isolated dot, observed after annealing 130°C (dark field) in (a) a 500nm wide structure and (b) in two 100nm wide ones.

While not evident crystallization of GST has been observed until 140°C, at 145°C nucleation and growth from the boundary of the structures (both dots and stars) take place (Figure 65). In particular in Figure 65b we show the growth from the boundaries of crystalline phase towards the center of the circular areas for 500nn and 300nn wide regions. Smaller dots are suddenly completely crystallized.

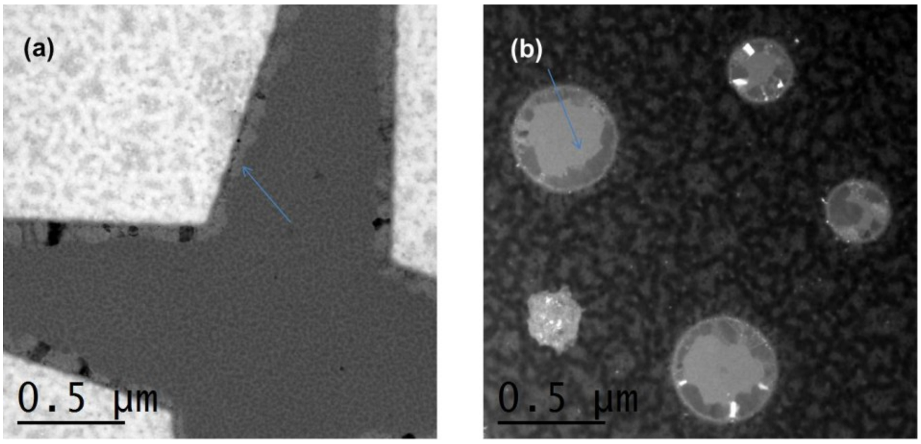

Figure 65 Plan-view TEM micrographs of (a) the star-shaped structure (bright field) and (b) 500nm and 300nm dots (dark field) annealed for 10 min at 145°C.

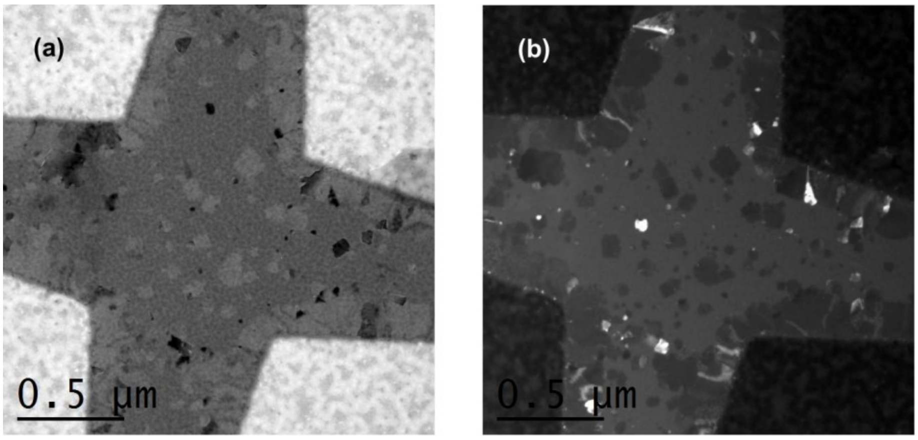

Figure 66 Plan-view TEM micrographs of the star-shaped structure: annealed for 10 min at 150°C: (a) bright field and (b) dark field

2.4 Comparison between present results and device configuration

The crystallization kinetics of nano amorphous dots embedded in fcc or hcp crystalline phase has been investigated at relative low temperature (75°C and 90°C).

The crystallization of the hcp/amorphous system seems to start by the rearrangement of the a/c interface in a defective crystalline layer. This initial step proceeds with a fast growth velocity, with a rate about four times higher than that one measured in the subsequent steps.

In the remaining process, the growth velocity is quite similar to that one observed in the fcc/amorphous system. This result suggest that particular attention should be addressed in the data retention of sub-50nm GST based phase change memories, when their active regions are surrounded by the crystalline phase.

Observations performed on amorphous 100nm dots embedded in a polycrystalline fcc GST film, annealed at higher temperature (110°C and 120 °C) present recrystallization velocities comparable to that ones measured for as sputtered amorphous films, with rates a factor 5 higher for both the temperatures, and a good agreement for the activation energies (2.35 eV in the case of as sputtered film, 2.3 eV in the present work). The enhancement in the growth velocity is also related to the different local order of the amorphous structure caused by ion implantation.

Isolated amorphous regions of different sizes and shapes has been observed after isochronal annealing from 90°C to 150°C. Crystallization occurs at 145 °C from the boundaries of the structures, while nucleation from the bulk of the star-shaped regions takes place at 150°C. The higher crystallization temperature observed in this structures suggests to use similar systems to improve data retention.

Finally we have demonstrated a new procedure to fabricate amorphous region using a controlled Ga^+ beam at low energy (30 keV) and low fluencies (10^{14} ions/cm^2). This procedure allows to potentially reach feature sizes below conventional lithography and selective amorphization and to eliminate the presence of resist residuals during TEM observation.

Chapter 3

Fabrication and characterization of Phase Change Memory test structures

Phase Change Materials are routinely used in the optical memories (DVDs, CDs, Blu-Rays, etc.) for their relevant optical contrast between the amorphous and crystalline phases. The correspondent change in resistivity amounts up to six orders of magnitude. This property, together with the high switching velocity, data retention properties, and threshold voltage switching, etc. has been known since the first studies about PCMs in 1960s. However, while optical memories were widely developed in the following years, electronic memories remained proof of concepts or merely used to very particular, restricted field.

The reason is simple: to produce SET-RESET switching a certain quantity of material should be melted. This amount of material and then the required electrical power depends on the feature size of the adopted lithographic technology. Since in 1960 the technological node was several microns (10 μm) the power required to melt a PCM-dome is about 200000 times greater than that needed to melt a dome of 180 nm.

Only recently, with technological nodes of a few tens of nanometers, the PC-Memories becomes competitive to the other technologies of the CMOS-based market.

Reducing the feature size to the 32nm node several problems involve Flash memories (tunnel oxides, quantum effects, etc.) while the possibility of memories using phase change layers has been demonstrated until 2-3nm for films and about 20nm for nanostructures. Several prototypal PC memory devices have been developed in the last years with technological node up to 45nm [76].

The most frequently used memory layouts for commercial fabrication derive by the Lance cell concept. It can be easily integrated in a CMOS addressing system and also it can be fabricated in high-density geometries, essential for the storage requirement.

Together with a full addressing CMOS compatibility and with commercial requirements, however, it is fundamental to understand what problems are involved in the present and in the future technological nodes. Therefore a better understanding of the ultimate scalable memory cell requires test structures, with simpler design. With this aim we have fabricated, by EBL, some patterns with a feature size as small as 25nm.

Starting from Lankhorst's line cell design [46], a simplified flow chart has been adopted. The test structures use crystalline GST as electrical contacts and an active region patterned with a sub-lithographical area (Figure 67).

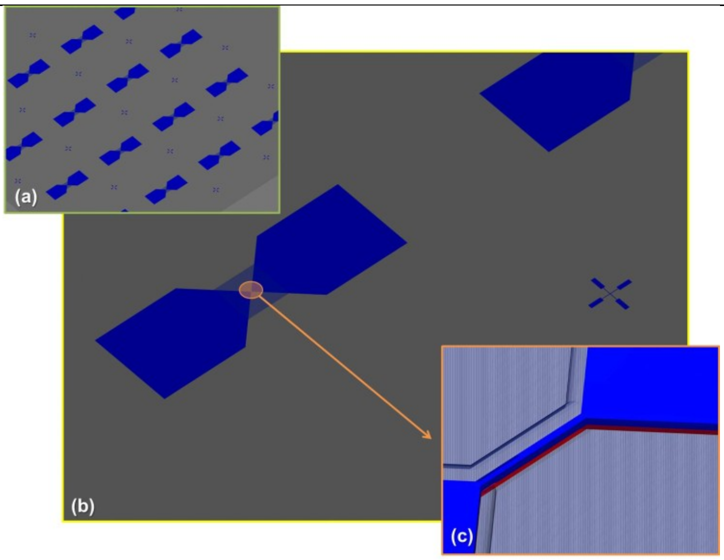

Figure 67 Different views of line devices. We show in red the GST alloy, in blue the HSQ hard-mask and transparent the HSQ for passivation. The crosses are used for masks alignments. (a) Array of line devices; (b) Details of a single device; (c) line active region.

The fabrication procedure is schematically described in Figure 68. An amorphous 20nm thin film of GST, deposited on 100nm SiO_2, is annealed at different temperature to obtain crystalline phase (a). The sample is then patterned by Electron Beam Lithography (b) and Inductively Coupled Plasma (c), using HSQ as resist and hard mask during etching. In these steps one dimension of the line cross section is defined by EBL, while the other one by the sputtered film thickness. Finally, the device is passivated by a further mask of HSQ patterned by EBL, covering the active region of the device (d).

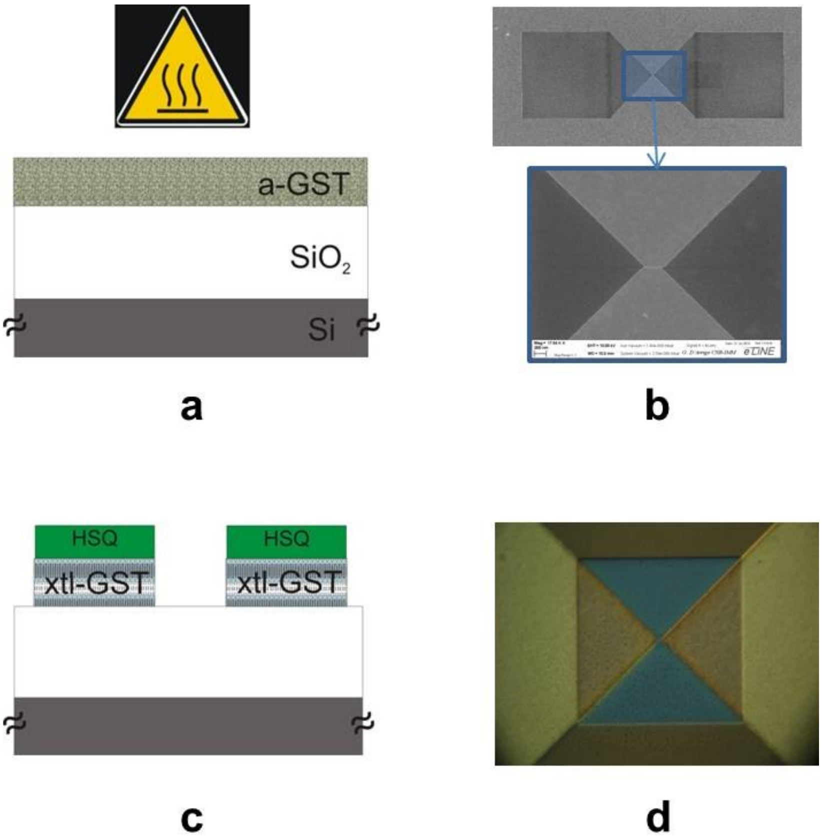

Figure 68 Flow chart of device fabrication: (a) crystallization of the chalcogenide amorphous film; (b) Electron Beam Lithography on HSQ hard-mask; (c) Transfer of the mask from HSQ to GST by Inductively Coupled Plasma; (d) Passivation (square) of the active region of the device with HSQ.

3.1 $Ge_2Sb_2Te_5$ thin film annealing for device fabrication

The first step of device fabrication is crystallization of the chalcogenide film. This step is required because the access resistance to the active region of the device should be as low as possible. It is important to perform this transition before patterning. Density increases of about 5% during the phase transition causing a film shrinkage that eventually breaks a very tight nanometric wire.

To reduce the access resistance it is convenient that the film crystallize in the hcp GST phase, at about 310°C [18] (Figure 69), which has the lower resistivity.

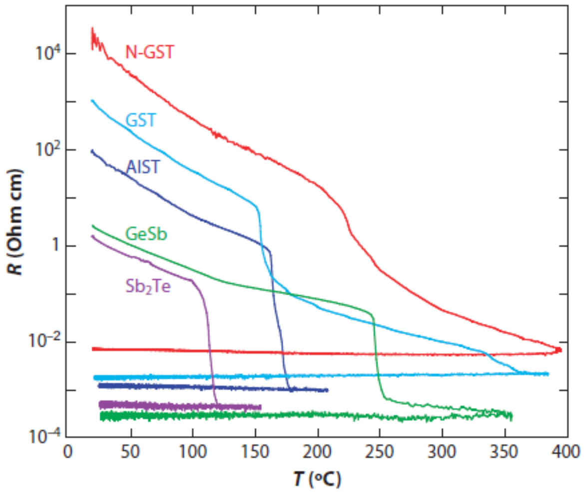

Figure 69 [26] Resistivity as a function of temperature for several 50-nm-thick as-deposited chalcogenide alloys. For $Ge_2Sb_2Te_5$ (GST), resistivity decreases about one order of magnitude when it crystallizes in the hcp phase, above 310°C.

The sample were annealed in the range between 150°C and 330°C. The annealing was performed in N_2 at 1 atm, with a 1” hotplate PID controlled.

Figure 70 shows the morphological analysis performed at the higher temperature. The darker areas in the images obtained by Scanning Electron Microscopy (SEM) are voids in the chalcogenide film produced by the annealing, as shown in TEM cross section.

One should note that even at the lower of 250°C, where no evident void formation occurs, the film roughness increase remarkable with respect to the as deposited film.

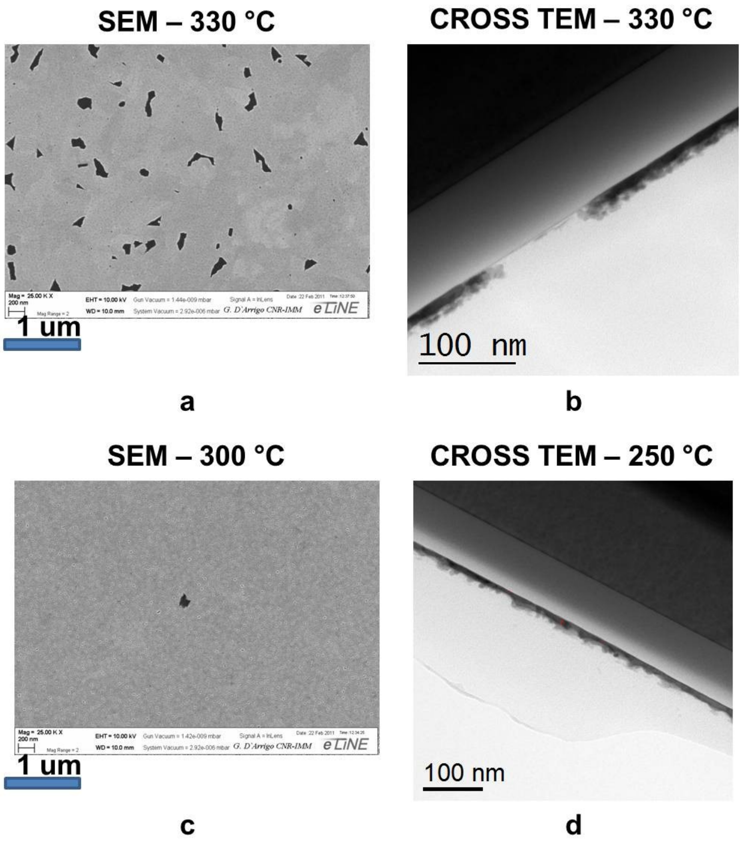
SEM – 330 °C

CROSS TEM – 330 °C

SEM – 300 °C

CROSS TEM – 250 °C

Figure 70 Scanning Electron Micrographs (a and c) and cross view Transmission Electron Micrographs (b and d) of 20nm thick GST film annealed at different temperatures. As the temperature decreases the amount of voids reduces.

To reduce this roughness, therefore, we have further decreased the annealing temperature to 180°C. In this condition the film thickness is about 22nm with some thinner regions of about 12 nm (Figure 71).

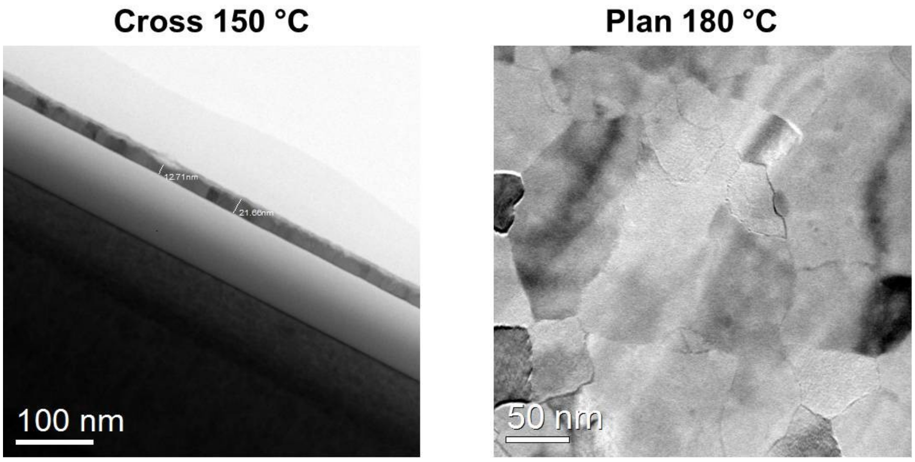

Figure 71 Cross and plan views of GST annealed at low temperatures. With respect to the high temperature annealed specimens, shown in Figure 70, no voids are present and the surface roughness is greatly reduced.

However, this temperature is not enough to reach the hcp phase, the film remains in the fcc state maintaining resistivity about 30 times higher than that in the hcp phase. (Figure 72).

To avoid the influence of voids and roughness on the behavior of the line structure we fabricate our test device in GST annealed at 180°C.

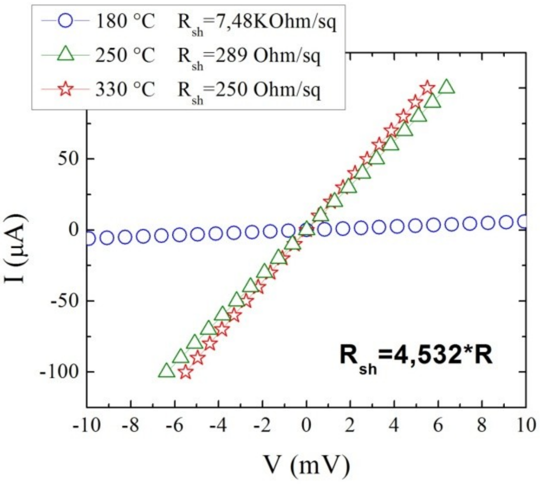

Figure 72 Sheet resistance of GST annealing at different temperature. At 180°C the sample is in the fcc phase, without voids, but with a resistivity about 30 times higher than hcp phase.

3.2 $Ge_2Sb_2Te_5$ lithography and patterning

After crystallization by thermal annealing, the film was covered with about 55nm of HSQ by spin coating, following the procedure described in paragraph (2.1.2). We then proceed with electron beam lithography.

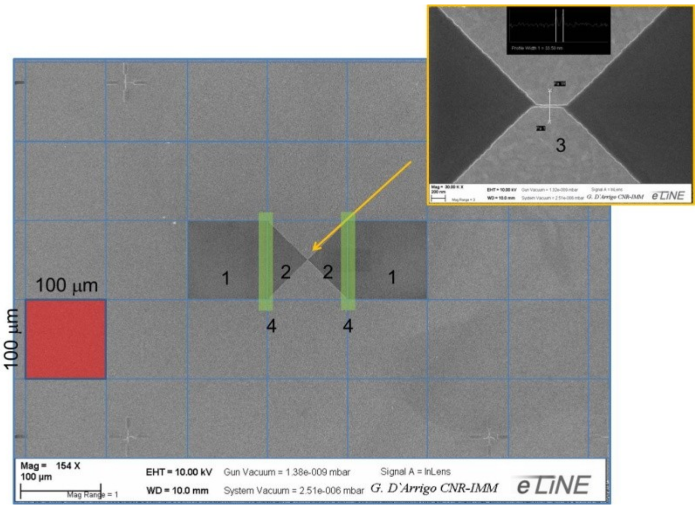

Figure 73 SEM micrograph of HSQ patterned by EBL. The working area is organized in writing field of 100 µm x 100 µm (for istance the red square. Two writing fields are used to pattern the pad masks (Area 1). In the central field, two triangle shapes (2) were written. Between the two triangles is established a gap of about 400 nm filled by a line (3) about 30nm wide. To avoid detachment between contiguous areas (Figure 74) two rectangular areas have been patterned overlapping the square-triangles areas (4).

For the EBL the sample area was organized in writing field of 100 µm x 100 µm. Two writing fields are used to pattern the pad masks (Area 1). In the central field, two triangle shapes was written. Each triangle is isosceles, half a square patterned in 1. Between the two triangles is established a gap of about 400 nm. The cuspidor shape given by the 90° angle vertexes of the triangles prevents any charge proximity effects. A line bridging the two triangles is then written (step 3). In principle, these lithographic steps are enough to fabricate a line structure electrically connected with the pads. However, charge accumulation, in the proximity of the writing fields boundaries, can produce beam deviation and, therefore, square (1) and triangle (2) detachments (Figure 74). For this reason we have introduced a further step, patterning two rectangular shapes overlapping square and triangle fields (4: green area in Figure 73).

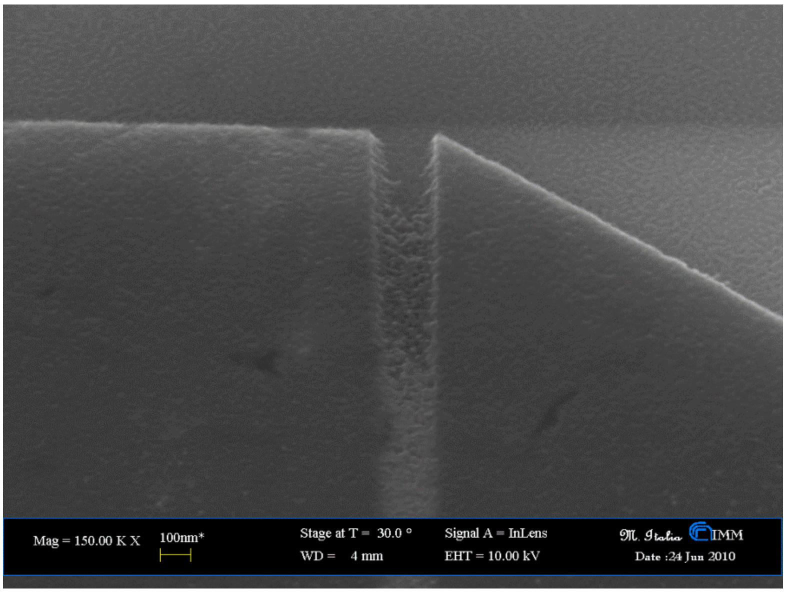

Figure 74 By proximity effects between different EBL patterned regions, detachment between contiguous areas can occur. Once they are transferred, by dry etching, to the GST underlayer, they can cause electrical failures.

After EBL, the samples are developed in TMAH for one minute and then washed in IPA. To further cross-linking the bonds in HSQ, the sample is annealed in N_2 at 180°C for 30 min.

The mask is then transferred to the GST layer by Inductively Coupled Plasma Etching (see 2.1.2). The result of the etching is showed in Figure 75.

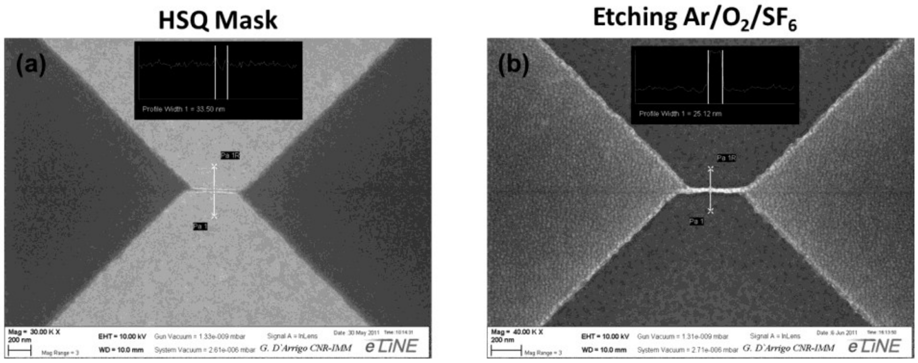

HSQ Mask

Etching Ar/O_2/SF_6

Figure 75 (a) Lithographed HSQ resist in which a line ≈400nm long and ≈34nm wide was patterned. (b) after Ar/O_2/SF_6 dry etching, the line width is reduced to ≈25nm.

In Figure 76 we show a plan TEM micrograph of the active part of the device after Plasma etching (test structure, without passivation). The grain contrast shows clearly the crystalline phase, also confirmed by Electron Diffraction, in which polycrystalline rings can be straightforwardly attributed to the fcc phase.

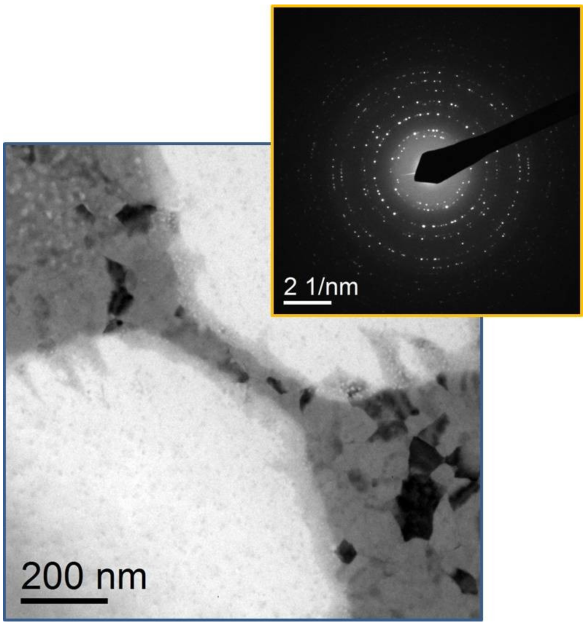

Figure 76 Transmission Electron Micrograph (bright field) of a line cell memory (test structure without HSQ passivation layer). The high contrast grain clearly indicates the crystalline state, such as the Selective Electron Diffraction in the inset. Circular rings position confirm a fcc polycrystalline phase.

In Figure 77 we show a tilted SEM view of the line active area. Darker region corresponds to the GST material while brighter one refer to the covering HSQ hard mask. The high surface roughness is produced by the plasma etching.

The active line region is then passivized: an overlayer of 55nm of HSQ is spinned on the sample and prepared for the EBL following the previous procedure. A square region of 50 mm x 50 mm is patterned over the line of GST. The sample is developed with TMAH 4% in H_2O, washed in IPA, and then annealed at 180°C for 30 min in N_2 at 1 atm.

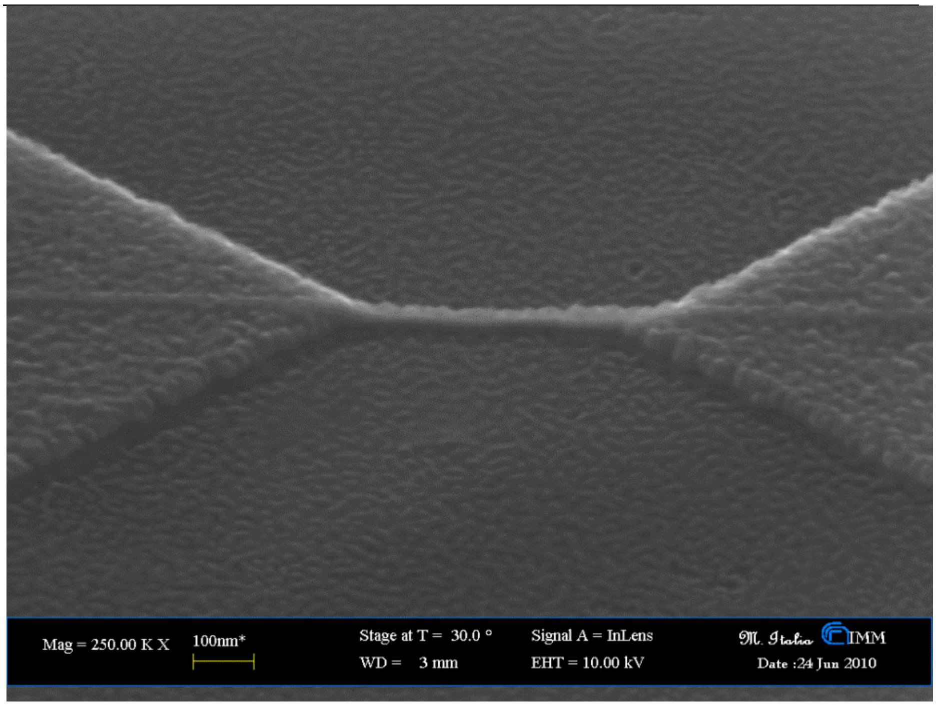

Figure 77 Scanning Electron Micrograph of a line memory cell (dark region) covered by the HSQ resist mask. The high surface roughness is produced by the plasma etching.

To test the HSQ breakdown voltage, a series of 19 MOS are fabricated and tested, in which an HSQ layer, annealed in N_2 (1 atm) at 300°C, is sandwiched between an As heavy doped Silicon and Pt square pads, 100 nm thick and 100 μm wide, patterned on HSQ by Optical Lithography and lift-off process. The MOS are then electrically tested with a slow (≈1 s) ramp from 0 to 100V in the MOS accumulation regime.

The majority of the MOS break downs at about 50 V. Even in the worst case, however, in which one MOS breaks down at 3V, the value is good for our 400 nm long line, in which the correspondent breakdown voltage is then about 12 V. As showed in the next chapter, in fact, the programming voltage is always below 3V.

In Figure 79, finally, we show the device at the end of the process by optical microscope. Note the optical contrast produced by the HSQ passivation square.

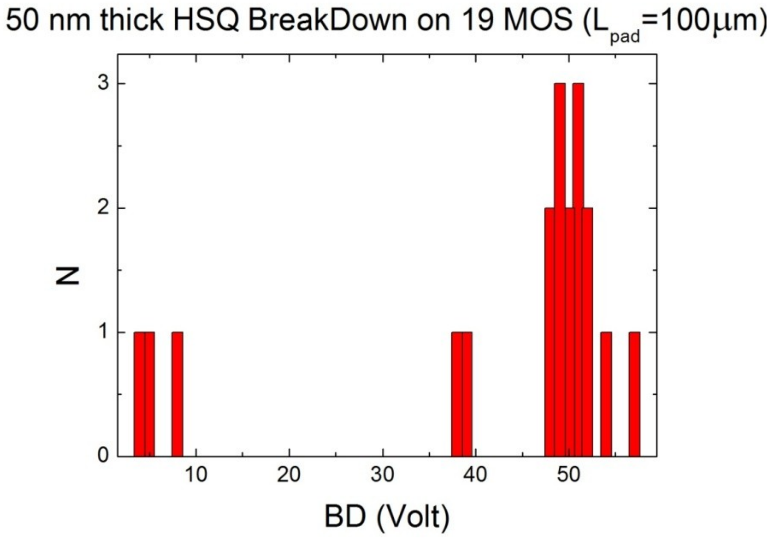

Figure 78 Breakdown voltage measured for MOS in which the dielectric is made by a 50nm thick HSQ film. The peak at 50V corresponds to a breakdown filed of 10 MV/cm, comparable to that of a thermally grown silicon dioxide [77].

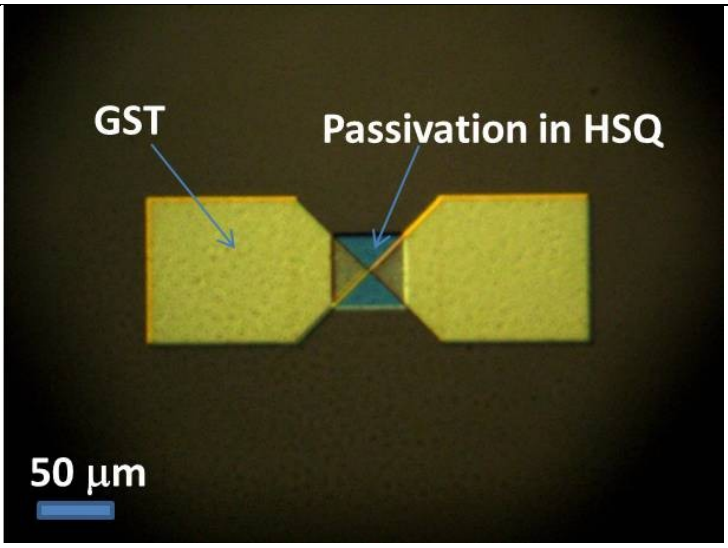

Figure 79 An optical image of the device we have fabricated in this thesis. The large GST square areas (l=100µm) work as pad for the electrical access to a shrunk line region (w=25nm, L=410nm, th=20nm), in the inset, that is the active memory part of the device. Over it, Hydrogen silsesquioxane (HSQ) is deposited for passivation.

3.3 *Electrical Characterization*

3.3.1 Bench setup

Electrical characterization of a PCM device regards both programming and resistivity measurements.

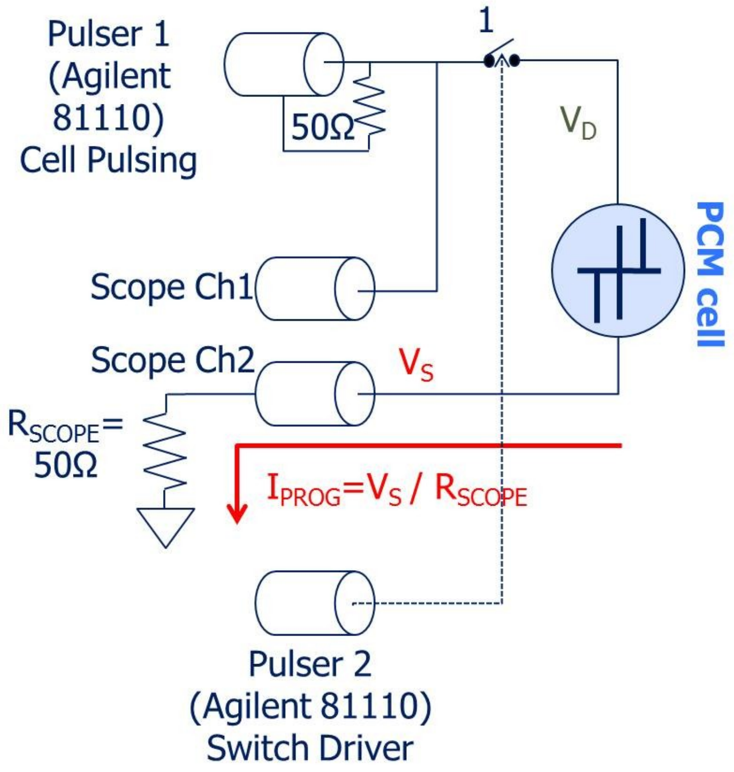

Figure 80 Typical programming circuit for phase change memory cells. A pulse generator (Agilent 81110A) is used to deliver fast (≈100ns) voltage pulse (Pulser 1). The I-V trace of the cell is obtained by a fast oscilloscope. The scope Ch1 measures the potential V_D provided by the generator. The Scope Ch2 measures a potenzial Vs, dropping on the resistance $R_{scope} = 50\Omega$ of the probe, giving a measurements of the current $I_{prog} = V_s/R_{scope}$. The trigger signal of the pulse generator (Pulser 2) can be used to actuate a switches (1) to enable/disable the circuit.

The first one concerns AC fast pulses, at least in the ≈100ns range, while the second are high-sensitive slower measurements, usually several ms long. In Figure 80 it is reported the system used for programming the cell.

The programming system should satisfy the following requirements:

- Since the RESET operation is usually shorter than 100 ns, the I-V response should be measured with a time resolution of at least of this order.
- Since the SET operation can be achieved with pulses as short as tens of nanoseconds [47], the rise and fall time of the pulses should be as short as possible. This is also a fundamental requirement to obtain rapid quenching and, therefore, amorphization.
- The current delivered by the single pulse to the device, considering SET and RESET operation, should range from ≈1μA to ≈1mA.

The first condition is fulfilled measuring voltage and current with a GHz oscilloscope. Voltage dropping in device, V_D, is measured by Scope 1 while current is obtained by the ratio V_S/R_{scope}, where V_S is the voltage measured by Scope 2 and $R_{scope} = 50\Omega$. However parasitic RC can reduce time resolution up to 75ns [78] therefore isolation and cables should be properly chosen and impedance matching between device, pulser and oscilloscope channels must be carefully considered if nanosecond resolution is needed [47]. The requirements about voltage and current essentially depend on the characteristics of the pulser. Width, rise and fall time of the delivered pulse are ≈ns for the most used pulser generators. Again, however, the signal on the cell depends on the other factors aforementioned. In the system shown, based on the oscilloscope signals, the RC characteristic time has been estimated ≈5ns.

The electrical resistance of the device usually ranges from several KOhm, in the SET state, to several MOhm, in the RESET state. Bench characterization of these two states should be performed accurately. At this purpose a DC

Measurement system is needed, usually a parameter analyzer or an equivalent setup. In , we show the DC measurement system used during characterization of the memory cell fabricated in this work. It consist on a Keithley 236, performing a Kelvin resistivity measurement on the cell under test. After each programming pulse, V_{force} forces a tension of 0.2V until V_{meter} reads this value.

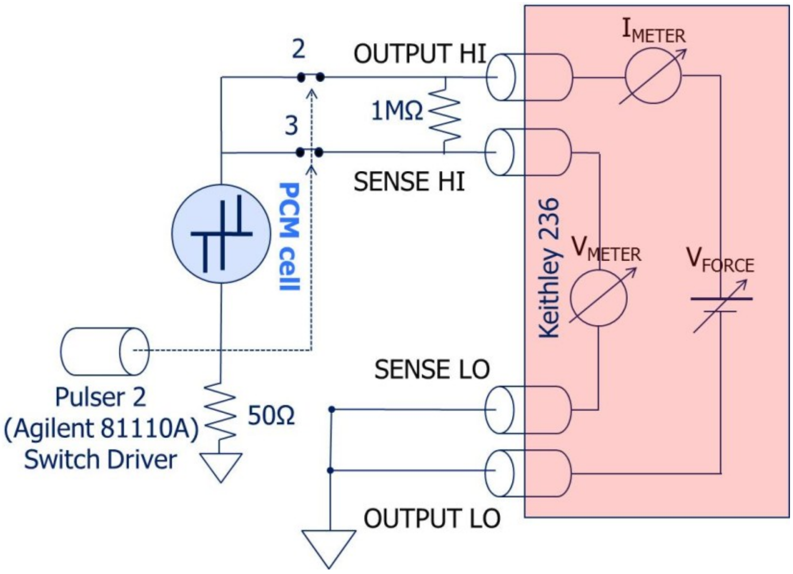

Figure 81 Typical DC measurement circuit for phase change memory cells. A keithley 236 is used to perform Kelvin resistivity measurement. A high resistance of 1 MΩ connects force and sense probes, in order to protect the keithley 236 in the case of switching failures. The trigger signal (Pulser 2) of the pulse generator can be used to actuate a switches (2 and 3) to enable/disable the circuit.

Note that, by this way, measurement on V_{meter} is not affected by the resistivity of switches 2 and 3. The resistivity of the PCM cell is then $\frac{V_{meter}}{I_{meter}} - 50\Omega$.

Programming pulse and DC measurement systems can be used together (Figure 86), synchronizing them, by using switches (1, 2 and 3 in figures) actuated by the trigger signal of the pulser. This merging is essential for extensive cycling characterization, in which programming pulses and DC measurements must be continuatively alternated. During programming operations switch 1 is closed, while switches 2 and 3 are opened, enabling AC pulse system. After each programming pulse the resistance of the cell is measured by a Keithley 236 Source-Measure Unit, opening switch 1 and closing switches 2 and 3. To avoid any problem related to switching failures, an high resistance (1 MΩ) connects OUTPUT HI and SENSE HI terminals, to protect the keithley 236. If switches 2 and 3 was opened during cell readout, indeed, the Source-Measure Unit enhanced the forced tension, in order to try to deliver the required value to V_{meter}; when switches close, therefore, an uncontrolled amount of tension (and the related current) is provided by the unit, potentially damaging the whole system.

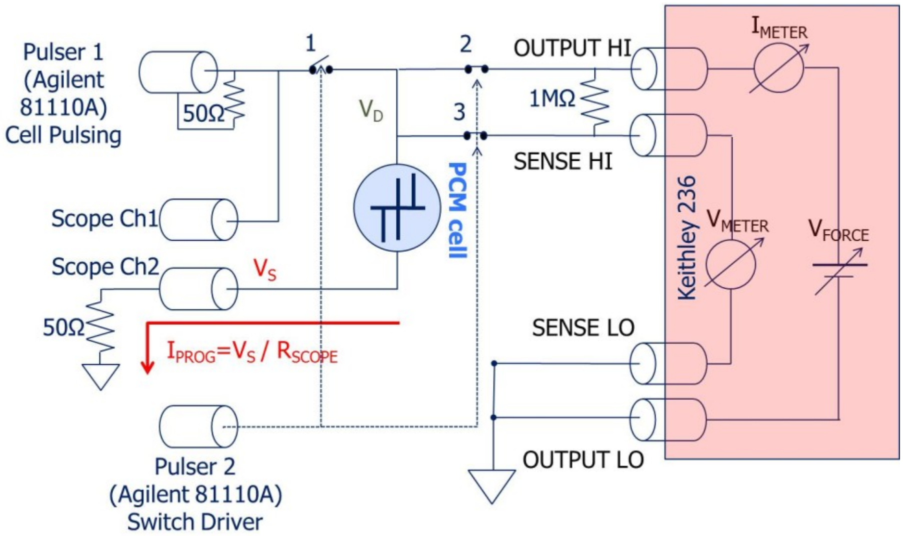

Figure 82 Electrical characterization bench scheme for programming AC pulses and DC measurements. For cell programming, electrical voltage pulses, several hundred ns long, were delivered by an Agilent 81110A pulse generator connected to the device (switch 1 closed, switches 2 and 3 opened). After each programming pulse the resistance of the cell is measured by a keithley 236 (switch 1 opened, switches 2 and 3 closed) in a Kelvin

configuration. Switches position are established by the trigger signal of the pulse generator.

3.4 *Programming and sensing of bridge cell memory*

The electrical measurements shown in the present section has been performed by Andrea Cattaneo at the Politecnico di Milano.

Figure 83 shows a typical programming sequence performed on the device. From the initial setting of the device (set crystalline state) sweeps up (blue dots) and down (red dots) have been delivered. Each sweep is accomplished by 25 voltage pulses, 300 ns long, from 0 to 2.7 Volt in the case of sweep up; the viceversa (maintaining pulse number and width) holds for sweep down. The sweeps on Figure 83-Figure 85 refer to the third sweep up/sweep downs cycle.

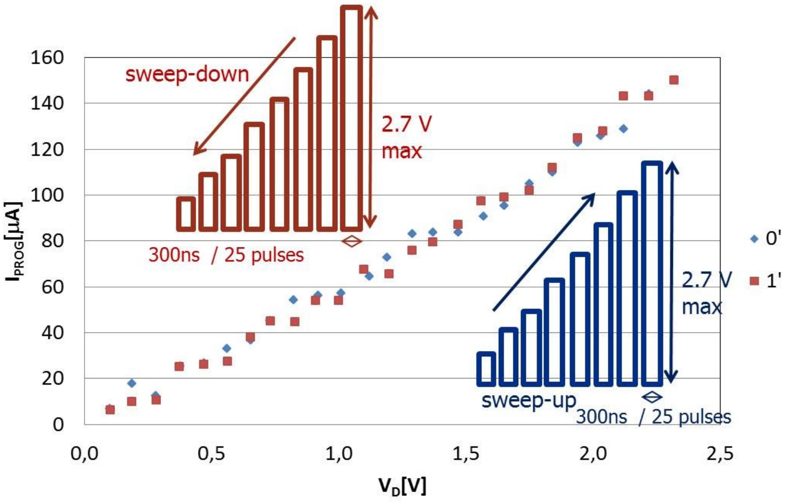

Figure 83 I-V sweeps performed on an initial SET state. Each sweep consist of 25 pulses, 300ns long, from 0V to 2.7V for sweep up (blue dots) and from 2.7V to 0V for sweep down (red dots).

Figure 84 shows an R-V plot that underlines the phase change transition at about 160 µA for RESET operation and 100 µA for SET operation. A change in resistivity of about three order of magnitude is observable between this two states.

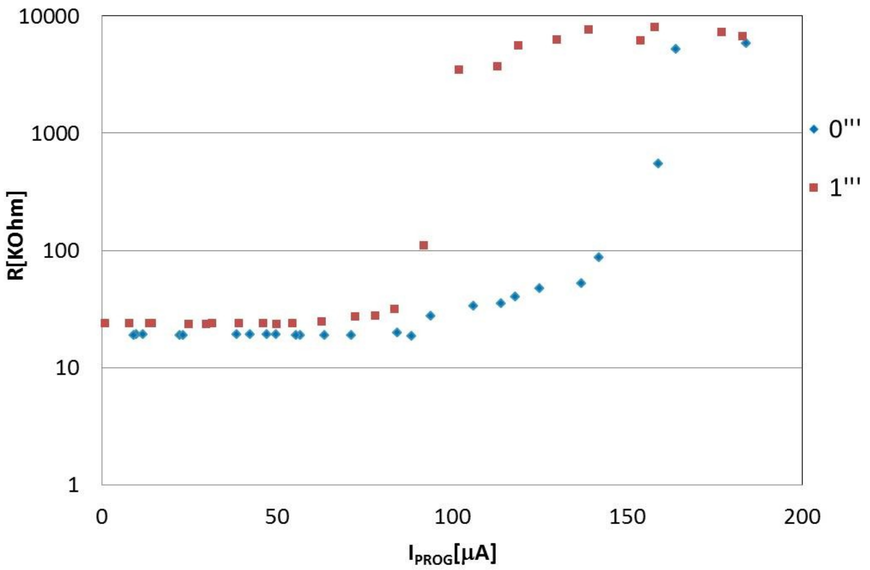

Figure 84 Resistance of the cell measured after each pulse of sweep up (blue dots) and sweep down (red dots) in function of the current I_{PROG}.

In Figure 85 we plot the same resistivity curve as a function of power in the cell, during sweep up and sweep down. A power of about 380 μW is required to bring the cell in the high-resistivity state, while crystallization occurs when the sweep down reaches ≈150 μW. The hysteresis in this curve can be ascribed to different causes. First, the thermal conductivity of crystalline GST is about a factor three higher than the correspondent value for amorphous phase [79]. As a consequence, heat dissipation is reduced when RESET state holds, and the power addressed to the memory cell must be heavily decreased to avoid the melting and, therefore, to permit crystallization.

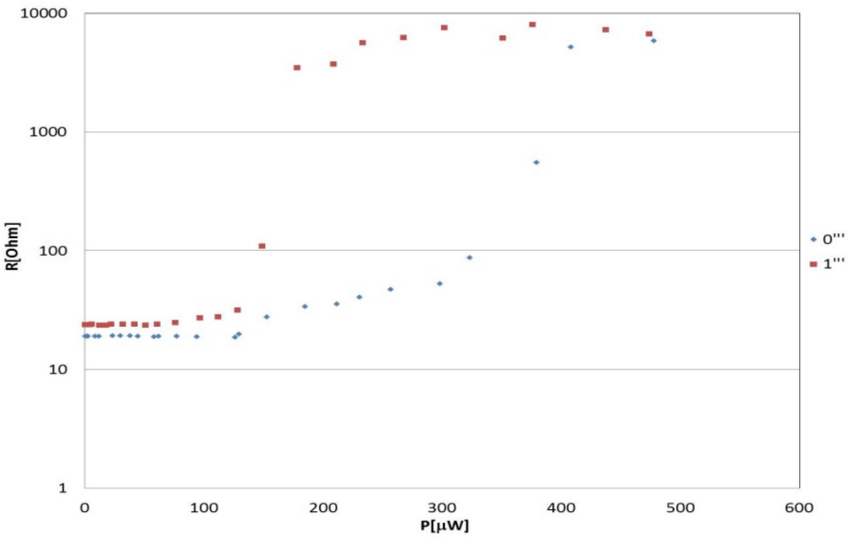

Figure 85 Resistance of the cell measured after each pulse of sweep up (blue dots) and sweep down (red dots) in function of the power dissipated by the memory cell.

Second, as we have shown in the previous chapter, crystallization kinetics is influenced by surrounding environment: when we consider the RESET operation melt must solidify in a crystalline environment, so a significant amount of liquid phase (high power) is required to avoid complete regrowth of the surrounding crystalline grains. However, since a relevant drift of the R-P curves has been observed with the programming cycle (Figure 86), a crucial role should be played by modification in the material local stoichiometry. This phenomenon can be ascribed to incongruent melting and electromigration [80].

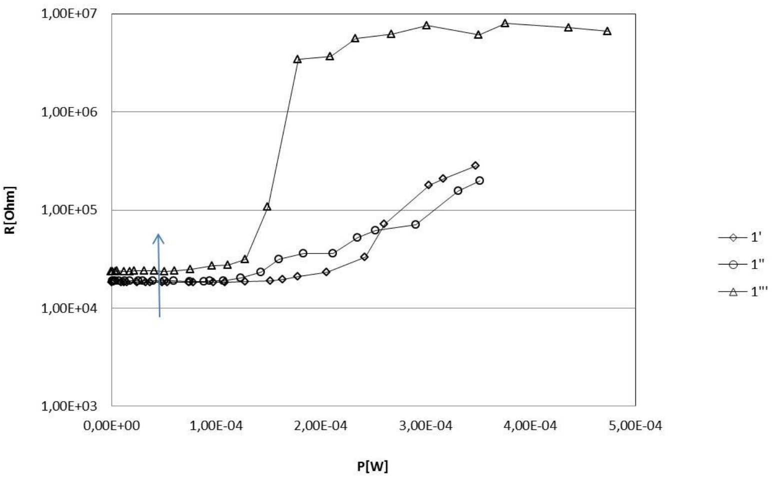

Figure 86 R-P curve for the first (1'), the second (1'') and the third (1''') sweep down from the amorphous phase. An evident hysteresis is observed with the cycles, indicating probably incongruent melting and/or electromigration phenomena.

In Figure 87, we compare a sweep up from SET state (triangles) and a sweep up from RESET state (squares). Sweep up from crystalline phase amorphizes the cell at about 160 μA as shown in Figure 84. However this effect, in the I-V curve, is masked by threshold switching and it is only visible sensing the cell resistance. In the case of a sweep up from amorphous phase, instead, the threshold switching phenomenon brings suddenly the cell in a (amorphous) high conductively state, enhancing the current flowing on the cell. The amorphous region in the line reaches a high conductivity state that does not play a significant role in the total series resistance. As a consequence the dynamic resistances of amorphous cell and crystalline one over the threshold switching region are very close, as it is evident in Figure 87. The high joule power dissipated by a RESET cell in the threshold switching regime permits an high enhancement of the local cell temperature in a voltage regime very low with respect to that one compatible with the high resistivity state of the amorphous phase in the DC, under threshold, measurements.

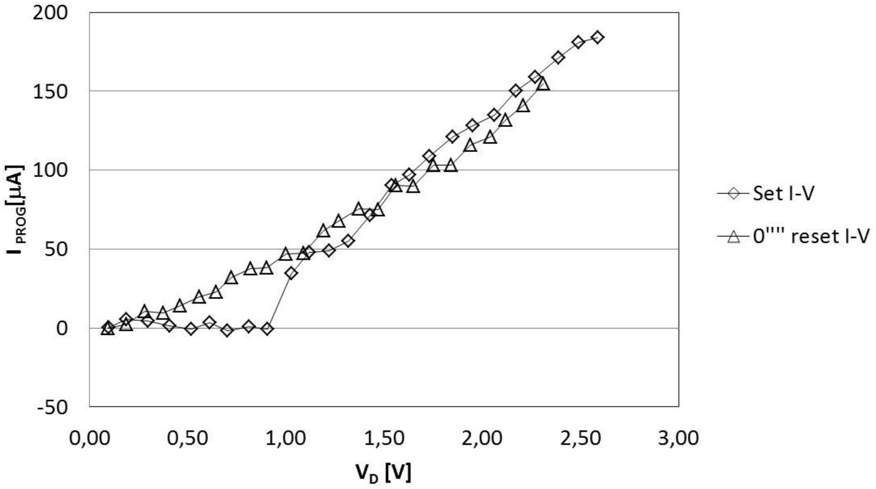

Figure 87 I-V curves of SET (squares) and RESET (triangles) states during programming pulses in sweep up. A threshold switching at about 1 V is clearly visible.

In Figure 88 we show a cycle-endurance test. The memory cell is continuously switched from RESET to SET and vice versa. In the case reported in the figure, after about 100 cycles, a *stuck reset fail* occurs, i.e. no high resistivity state occurs after a reset pulse.

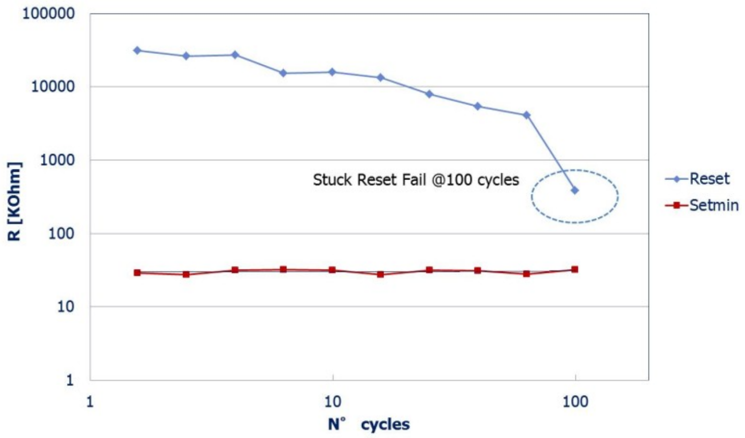

Figure 88 Typical result of a cycle-endurance test. The cell is cycled continuously with alternating RESET and SET pulses. After each programming pulse, the D.C. cell-resistance is measured. In the case shown, a *stuck reset fail*, i.e. no high resistivity state is obtained after a RESET pulse, occurs after 100 cycles.

On the contrary one can obtain during RESET/SET cycling a *stuck set fail*, i.e. no low resistivity state is recovered after a SET pulse (Figure 89). Cycling produces electrical and mechanical stress along the line memory. In particular, since amorphous phase is about 5% less in density than fcc crystalline one, a pressure of about 2 GPa can be applied to the active region when it is amorphized. With the change of density back and forth between the two bit states, any void can emerge and, as a consequence, we observe the stuck set fail.

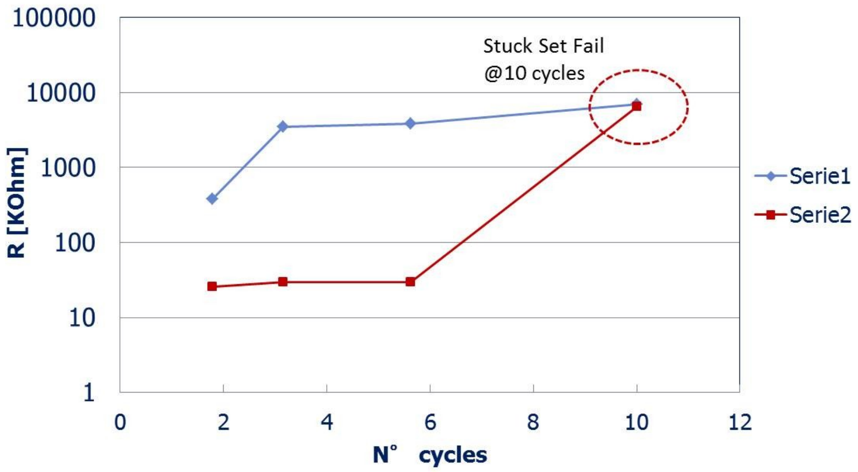

Figure 89 Typical result of a cycle-endurance test. The cell is cycled continuously with alternating RESET and SET pulses. After each programming pulse, the d.c. cell-resistance is measured. In the case shown, a *stuck set fail*, i.e. no low resistivity state is obtained after a SET pulse, occurs after 10 cycles.

Fortunately, a stuck set fail can be easily recovered by a suitable DC sweep. In Figure 90, we show the I-V curve correlated with a current sweep from 0 to 50 μA during a ≈10 ms long sweep. In the first part of the curve the response of the failed device is exponential (indicated by the green fit line in the semilog scale) in according with the formation of a void along the line cell. Then the current abruptly increases (red area). The large amount of current in this last region is a signature of a probably melting of the chalcogenide around the void. After the quenching void is annihilated and the switching characteristics of the device are fully restored.

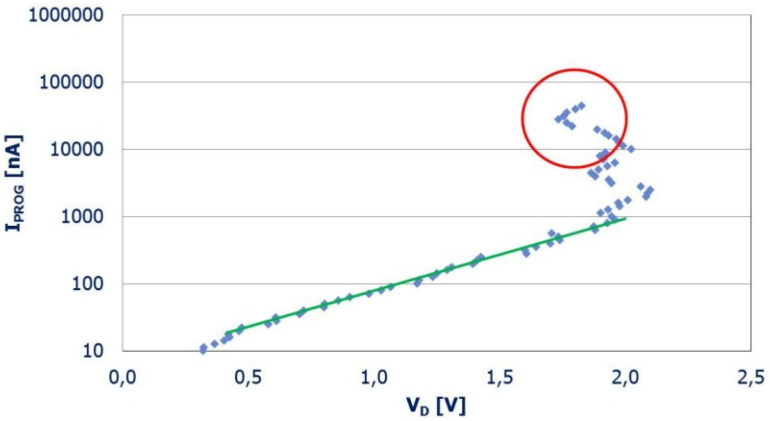

Figure 90 DC sweep up applied to a cell suffering a set stuck fail. In the first region of the ramp (green) the I-V curve reflects an exponential behavior, typical of vacuum tunneling current. In the second part of the ramp current enhances permitting an high Joule heating producing melting near the void. As a consequence possible voids can be reassembled by the melt.

It has also been observed that cells can easily be switched from a reset stuck state to a set stuck state just slightly enhancing the RESET voltage. In Figure 91 it is shown a device programmed (a) with SET pulses 1.5V for 500ns and RESET pulses 3V for 300 ns. After reaching failure at about 70 cycles, the memory cell is brought to a reset stuck set changing only the RESET voltage to 3.5V.

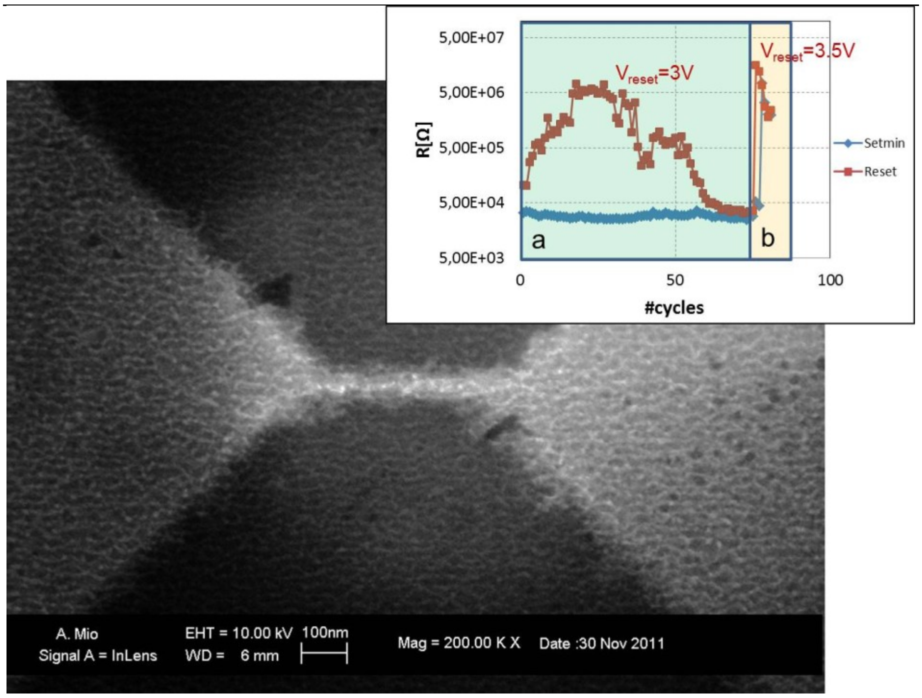

Figure 91 Cycling-endurance test. The cell is subjected to a reset Voltage at 3V (t=300ns) until it falls in a stuck reset fail. After that, reset pulses at 3.5V (same duration) brought it in a stuck set fail. The SEM shows the cell morphology after the test.

Other cells present an higher threshold switching voltage of the order of 3÷4 V. These cell required a longer SET time to recrystallize, about 20 µs (maintaining however a RESET time of 300 ns). Also in these cases we estimate cell ciclability, that was about 170 cycles (Figure 92).

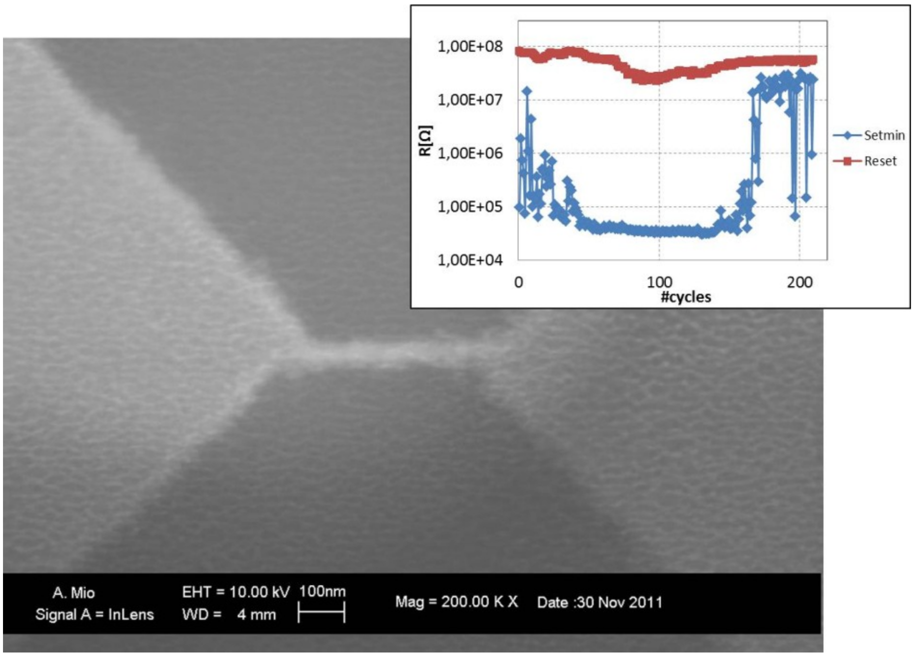

Figure 92 Cycling-endurance test for a cell requiring long SET pulses to crystallize (≈20 µs). The cell is cycled continuously with alternating RESET and SET pulses. After each programming pulse, the D.C. cell-resistance is measured. In the case shown, a *stuck set fail*, i.e. no high resistivity state is obtained after a RESET pulse, occurs after 170 cycles. The SEM shows the cell morphology after the test.

3.5 Discussion and Future Perspective

In this chapter we have presented a simplified approach to fabricate and characterize a phase change test structure memory with reduced active size. By short pulses, as fast as 300 ns, cells has been successful switched between SET and RESET states. Moreover, programming current has been found to be very low, in the 100 µA range. In most cases a cyclability of 100÷200 has been measured. Although this result must be improved, a mechanism to recover the cell from a stuck reset fail has been shown, giving an important perspective about enhancing the endurance of the PCRAM. A non-negligible drift has been observed in cell morphology, in particular on its wideness. At this purpose, several improvements has been introduced in the flow chart, involving the optimization of the parameter of the lithography and of the plasma etching, and new optimized structures has now under electrical tests.

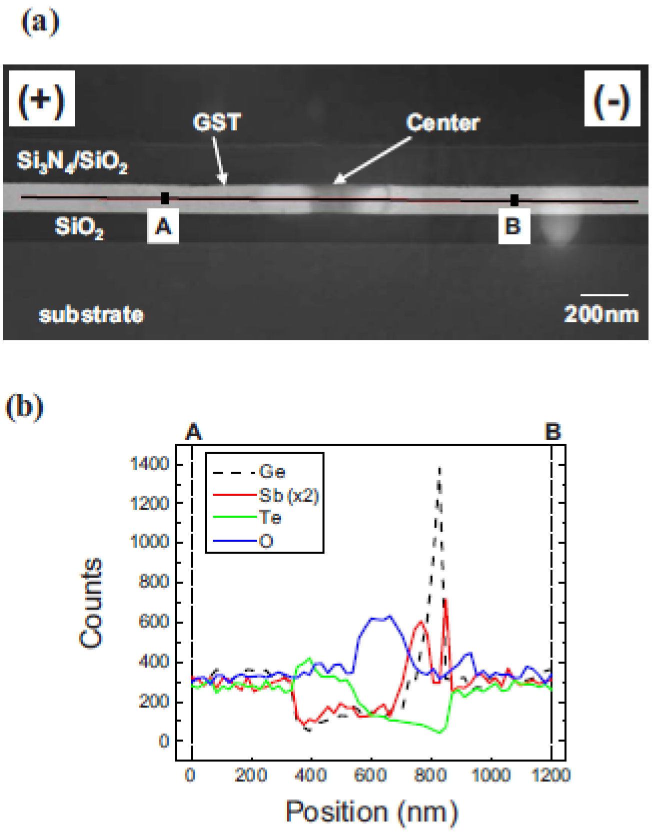

Figure 93 [80] (a) Cross-sectional TEM image of a GST line cell (100nm thick, 100nm wide and 130nm long). The cell is TEM prepared after 10^3 cycles, well below the endurance presented by the authors (≈10^5 cycles). (b) EDS line profile along the line A-B. For clarity, the intensity of Sb is doubled.

Any drifts in the electrical behavior can be ascribed both to morphological deviation and to dynamical variation in material stoichiometry during programming. The first one should regard mainly the amount of energy required to switch the material (current amplitude and pulse duration). The second should involve mainly its switching and resistivity characteristics [81, 82]. Both aspects can change the endurance.

Material stoichiometry variation has been recently pointed out by several studies, performed both on bridge cell and on lance cell [80, 83]. In particular, for line cell layout, it has been found that, probably for electromigration process, that Ge and Sb atoms migrate towards the cathode while Te atoms towards anode. As been pointed, this observation cannot be affected by eventually asymmetry of the hottest point in the line, determined by Thompson effect, since the consequential thermal stress should produce a unique behavior for the drift direction of the GST atoms.

Kim et al. also noticed their line structure memories fail for void formation, with Ge segregation around the void. They connect Ge precipitation to the different mobility of Sb liquid phase and Ge solid phase, that separate each other by incongruent melting. However line structure they study was 100nm thick, 100nm wide and 130nm long, with a cross section well above that one presented in the present work. With the aid of both plan and cross TEM, using TEM-EDS, it will be possible, therefore, to study eventual element migration in the line cell fabricated in this work.

Conclusions

In this thesis we have studied the crystallization behavior of amorphous samples at different scales, pointing towards layouts similar to those ones occurring in PCM-based devices. In the first part we have clarified the relevance of the amorphous local structures produced by ion implantation and we have detailed the crystallization kinetics of GeTe thin film. Nucleation and growth phenomena have been observed by optical microscopy in a large region and corresponding rates and velocities have been found. From these data, the activation energies of each process have been calculated and compared with those obtained by a JMAK analysis of independent TRR measurements. The nucleation rate and growth velocity of the implanted films increased by a factor ten and three, respectively, with respect to the as deposited samples, suggesting the occurrence, during implantation, of a local atomic arrangement which enhances the crystallization kinetics. This evidence is in agreement with Raman spectroscopy data, suggesting that implantation, proving kinetics energy by collision cascades, produce a reduction of wrong bonds formed during sputter deposition.

In the second part we have analyzed the crystallization of amorphous nanostructures of GST obtained by ion implantation, both isolated or embedded in its crystalline environment (fcc or hcp). Hcp Embedded nano amorphous dot (100nm in diameter) crystallization has been observed to start by the rearrangement of the a/c interface in a defective crystalline layer. At 90°C, this initial step proceeds with a fast growth velocity of 6.4 pm/s, about four times higher than that one measured in the subsequent steps. The slower rate is very similar to that one measured in the fcc embedded nanostructures. A similar behavior has been observed for annealing at 75°C, with an initial faster rate of 0.58 pm/s. We have also observed the behavior of the smaller nanostructures (20nm) that completely crystallize very fast, after only two hours at 75°C. Since the active amorphous region in most devices is surrounded by the hexagonal phase this result suggests that particular attention should be addressed to the data retention characteristics of sub-50nm GST based phase change memories. Isolated amorphous regions of different sizes and shapes has been observed after isochronal annealing from 90°C to 150°C. Crystallization has been observed to occur at 145 °C from the boundaries of the structures, while nucleation from the bulk of star-shaped regions takes place at 150°C. The higher crystallization temperature observed in this isolated structures suggests that similar systems could be used to improve data retention. Finally we have demonstrated a new procedure to fabricate maskless amorphous region using a controlled Ga^+ beam at low energy (30 keV) and low fluencies (10^{14} ions/cm^2). This procedure allows to eliminate the presence of resist residuals during TEM observation.

In the third part we have presented a simplified approach to fabricate and characterize a phase change test-structure memory with reduced active size. By fast pulses, as short as 300 ns, cells has been successful switched between SET and RESET states. Moreover, programming current has been found to be very low, in the 100 μA range. In most cases a cyclability of 100÷200 has been obtained. Although this result must be improved, a mechanism to recover the cell from a stuck reset fail has been shown, giving an important perspective about enhancing the endurance of the PCRAM. The cell fabricated permits direct morphological, structural and chemical analyses, because of the easy access to the active region of the device (that is under a unique passivation film, instead of several layers). Correlation of these analyses to the electric characteristics of the test-structures (and their variations) could represent a key point in understanding the behavior of PCRAM.

Bibliography

[1] G. E. Moore, “Cramming More Components onto Integrated Circuits,” Electronics, pp. 114–117, April 19 (1965).

[2] M. L. Cohen, M. Y. Chou, W. D. Knight, W.A. de Heer, *J.Phys. Chem.* 91, 3141 (1987).

[3] C.R.C. Wang, S. Pollack, T. A. Dahlseid, G. M. Koretsky, M. Kappes, *J. Chem. Phys.* 96, 7931 (1992).

[4] C. Ellert, M. Schmidt, C. Schmitt, T. Reiners, H. Haberland, *Phys. ReV. Lett.* 75, 1731 (1995).

[5] S. Lai. Non-volatile memory technologies: the quest forever lower cost. In *IEDM 2008*, pages 01-02, (2008).

[6] K. Kim and S. Y. Lee. Memory technology in the future. *Microelectronic Engineering*, 84(9-10):1976-1981 (2007).

[7] S. K. Lai. Flash memories: Successes and challenges. *IBM Journal of Research and Development*, 52(4/5):529-533 (2008).

[8] W. Hutsell, J. Bowen, and N. Ekker. Flash solid-state disk reliability. *Texas Memory Systems White paper*, avaible on http://www.texmemsys.com/ les/f000252.pdf (2008).

[9] G. W. Burr, B. N. Kurdi, J. C. Scott, C. H. Lam, K. Gopalakrishnan, and R. S. Shenoy. Overview of candidate device technologies for storage-class memory. *IBM Journal of Research and Development*, 52(4/5):449-464, (2008).

[10] I. S. Kim, S. L. Cho, D. H. Im, E. H. Cho, D. H. Kim, G. H. Oh, D. H. Ahn, S.O. Park, S. W. Nam, J. T. Moon, C. H. Chung, "High performance PRAM cell scalable to sub-20nm technology with below 4F2 cell size, extendable to DRAM applications," *VLSI Technology (VLSIT), 2010 Symposium on* , vol., no., pp.203-204, (15-17 June 2010)

[11] The International Technology Roadmap for Semiconductors (2010). Available on: http://www.itrs.net/

[12] S. Privitera, S. Lombardo, C. Bongiorno, E. Rimini, A. Pirovano, *J. Appl. Phys.* 102, 013516 (2007).

[13] J. Kalb, F. Spaepen, M. Wuttig, *Appl. Phys. Lett.* 84, 5240 (2004).

[14] J. A. Kalb, C. Y. Wen, F. Spaepen, H. Dieker, M. Wuttig, *J. Appl. Phys.* 98, 054902 (2005).

[15] A.V. Kolobov, J. Haines, A. Pradel, M. Ribes, P. Fons, J. Tominaga, Y. Katayama, T. Hammouda, and T. Uruga, *Phys. Rev. Lett.* 97, 035701 (2006).

[16] S. Caravati, M. Bernasconi, T. D. Kühne, M. Krack, M. Parrinello, *Phys. Rev. Lett.* 102, 205502 (2009).

[17] D. Krebs, Electrical Transport and Switching in Phase Change Materials. *Ph. D. Thesis*, RWTH Aachen (2010).

[18] I. Friedrich, V. Weidenhof, W. Njoroge, P. Franz, and M. Wuttig, *J. Appl. Phys.* 87, 4130 (2000).

[19] T. Y. Lee, S. S. Yim, D. Lee, M. H. Lee, D. H. Ahn, and K. B. Kim, *Appl. Phys. Lett.* 89, 163503 (2006).

[20] A. Pirovano, A. L. Lacaita, A. Benvenuti, F. Pellizzer, A. Pirovano and R. Bez, *IEEE Trans. Electron Devices* 51, 452 (2004).

[21] V. Weidenhof, I. Friedrich, S. Ziegler and M. Wuttig, *J. Appl. Phys.* 89, 3168 (2001).

[22] T. Matsunaga, N. Yamada and Y. Kabota, *Acta Crystallogr. Sect. B* 60, 685 (2004).

[23] A. Kolobov, P. Fons, A. Frenkel, A. Ankudinov, J. Tominaga, T. Uruga, *Nature Mater.* 3, 703-708 (2004).

[24] S. Kohara, K. Kato, S. Kimura, H. Tanaka, T. Usuki, K. Suzuya, H. Tanaka, Y. Moritomo, T. Matsunaga, N. Yamada, Y. Tanaka, H. Suematsu, and M. Takata, *Appl. Phys. Lett.* 89, 201910 (2006).

[25] J. Akola and R. O. Jones, *Phys. Rev. B* 76 (2007) 235201;

[26] S. Raoux, *Annu. Rev. Mater. Res.* 39:25–48 (2009).

[27] S. Caravati, M. Bernasconi, T. D. Kühne, M. Krack, and M. Parrinello, *Appl. Phys. Lett.* 91, 171906 (2007).

[28] D. Lencer, M. Salinga, B. Grabowski, T. Hickel, J. Neugebauer, M. Wuttig, *Nature Mater.* 7, 972 - 977 (2008)

[29] S. Raoux, C. T. Rettner, J. L. Jordan-Sweet, V. R. Deline, J. B. Philipp, H.-L. Lung, “Scaling properties of phase change nanostructures and thin films”, *Epcos* (2006).

[30] WEI Xiaoqian, SHI Luping, CHONG Tow Chong, ZHAO Rong, and LEE Hock Koon, *Jpn. J. Appl. Phys.* 46 (4B), pp. 2211–2214 (2007).

[31] G. W. Burr, M. J. Breitwisch, M. Franceschini, D. Garetto, K. Gopalakrishnan, B. Jackson, B. Kurdi, C. Lam, L. A. Lastras, A. Padilla, B. Rajendran, S. Raoux, R. S. Shenoy, *J. Vac. Sci. Technol. B* 28, 223 (2010).

[32] A. Pirovano, A. Redaelli, F. Pellizzer, F. Ottogalli, M. Tosi, D. Ielmini, A. L. Lacaita, R. Bez, *IEEE Transactions on device and materials reliability* 4 (3) (2004).

[33] J. A. Kalb, Crystallization kinetics in antimony and tellurium alloys used for phase change recording, *Ph. D. Thesis*, RWTH Aachen (2006).

[34] J. Akola, J. Larrucea, R. O. Jones, *Phys. Rev. B* 83, 094113 (2011).

[35] R. De Bastiani, A. M. Piro, M. G. Grimaldi, E. Rimini, G. A. Baratta, G. Strazzulla, *Appl. Phys Lett*. 92, 241925 (2008).

[36] R. De Bastiani, E. Carria, S. Gibilisco, M. G. Grimaldi, A. R. Pennisi, A. Gotti, A. Pirovano, R. Bez, E. Rimini, *Phys. Rev. B* 80, 245205 (2009).

[37] S. Raoux, G. M. Cohen, R. M. Shelby, H.Y. Cheng, and J. L. J. Sweet, *Mater. Res. Soc. Symp. Proc.* 1251, H02-06 (2010).

[38] D. Krebs, S. Raoux, C. T. Rettner, G. W. Burr, R. M. Shelby, M. Salinga, C. M. Jefferson, M. Wuttig, *J. Appl. Phys.* 106, 054308 (2009).

[39] Y.-T. Kim, K.-H. Lee, W.-Y. Chung, T.-K. Kim, Y.-K. Park, J.-T. Kong, *Simulation of Semiconductor Processes and Devices*, pp. 211-214 (2003).

[40] J.-B. Park,1 G.-S. Park, H.-S. Baik, J.-H. Lee, H. Jeong, K. Kim, J. Electrochem. Soc., Volume 154, Issue 3, pp. H139-H141 (2007).

[41] S. R. Ovshinsky, *Phys. Rev. Lett.* 21, 1450 (1968).

[42] D. Ielmini, Y. Zhang, J. Appl. Phys. 102, 054517 (2007).

[43] A.M. Mio, E. Carria, G. D´Arrigo, S. Gibilisco, M. Miritello, M.G. Grimaldi, E. Rimini, *J. Non-Cryst. Solids* 357, 2197–2201 (2011).

[44] Y.H. Shih, J.Y.Wu, B. Rajendran, M.H. Lee, R. Cheek, M. Lamorey, M. Breitwisch, Y. Zhu, E. K. Lai, C.F. Chen, E. Stinzianni, A. Schrott, E. Joseph, R. Dasaka, S. Raoux, H.L. Lung, and C. Lam. Mechanisms of retention loss in

Ge2Sb2Te5-based phase-change memory. In IEDM Technical Digest, pages 9-01 (2008).

[45] A. Redaelli, D. Ielmini, U. Russo, and A. L. Lacaita, IEEE Trans. Electron Devices 53, 3040 (2006).

[46] M. H. R. Lankhorst, B. W. S. M. M. Ketelaars, R. A. M. Wolters, *Nature Mater.* 4, 347 (2005).

[47] G. Bruns, P. Merkelbach, C. Schlockermann, M. Salinga, M. Wuttig, T. D. Happ, J. B. Philipp, and M. Kund, *Appl. Phys. Lett.* 95, 043108 (2009).

[48] J. Lindhard, A. Winter, *Mat. Fys. Medd. Dan. Vidensk. Selsk.* 34 (4), 1 (1964).

[49] J. F. Ziegler, J. P. Biresack, and U. Littmark, *The Stopping and the Range of Ions in Solids* Pergamon, New York, (1985).

[50] R. De Bastiani, A.M. Piro, M.G. Grimaldi, E. Rimini, *Nuclear Instruments and Methods in Physics Research B* 257, 572–576 (2007).

[51] D. Kim, F. Merget, M. Laurenzis, P. H. Bolivar, and H. Kurz, *J. Appl. Phys. 97*, 083538 (2005).

[52] M. Volmer and A. Weber, *J. Phys. Chem.* 119, 277 (1926).

[53] R. Becker and W. Doring, *Ann. Phys. ~Leipzig!* 24, 719 (1935).

[54] A. N. Kolmogorov, *Izv. Akad. Nauk SSR Ser. Fiz. Mat. Nauk* 3, 355 (1937 in Russian).

[55] Selected Works of A. N. Kolmogorov, edited by *A. N. Shiryayev, Kluwer Academic, Dordrecht*, Vol. II. (1992).

[56] W. A. Johnson and R. F. Mehl, *Trans. Am. Crystallogr. Assoc.* 135, 416 (1939).

[57] M. Avrami, *J. Phys. Chem.* 7, 1103 (1939).

[58] M. Avrami, *J. Phys. Chem.* 8, 212 (1940).

[59] M. Avrami, *J. Phys. Chem.* 9, 177 (1941).

[60] G. Ruitenberg, A. K. Petford-Long, and R. C. Doole, *J. Appl. Phys.* 92, 3116 (2002).

[61] M. Libera and M. Chen, *J. Appl. Phys.* 73, 2272 (1993).

[62] V. Weidenhof, I. Friedrich, S. Ziegler, and M. Wuttig, *J. Appl. Phys.* 89, 3168 (2001).

[63] A. Cros, K. N. Tu, D. A. Smith, and B. Z. Weiss, *Appl. Phys. Lett.* 52, 1311 (1988).

[64] A.V. Kolobov, P. Fons, J. Tominaga, A.L. Ankudinov, S. N. Yannopoulos and K.S. Andrikopoulos, *J. Phys.: Condens. Matter* 16, S5103 (2004).

[65] R. Mazzarello, S. Caravati, S. Angioletti-Uberti, M. Bernasconi, and M. Parrinello, *Phys. Rev. Lett.* 104 (2010) 085503.

[66] A.S. Pine and G. Dresselhaus, *Phys. Rev. B* 4 (1971) 356.

[67] Q.M. Lu and M. Libera, *J. Appl. Phys.* 77 (1995) 517.

[68] W. Wełnic, M. Wutting, *Materials Today* 11, 20 (2008).

[69] Y. Saito, Y. Sutou and J. Koike, *Mater. Res. Soc. Symp. Proc.* Vol. 1160 H12-05 (2009).

[68] E. Carria, A.M. Mio, S. Gibilisco, M. Miritello, M.G. Grimaldi and E. Rimini, *Electrochem. Solid-State Lett.* 14 (2011) H124.

[69] K. S. Andrikopoulos, S. N. Yannopoulos, G. A. Voyiatzis, A. V. Kolobov, M. Ribes, and J. Tominaga, *J. Phys.: Condens. Matter* 18 (2006) 965.

[70] C. Spinella, A. Battaglia, F. Priolo and S. U. Campisano, *Europhys. Lett.* 16 (1991) 313.

[71] B.C. Johnson, P.Gortmaker, J.C. McCallum, *Phys. Rev. B* 77 (2008) 214109.

[72] J. Goldak, C.S. Barrett, D. Innes and W. Youdelis, *Jour. Chem. Phys.* 44 (1966) 3323.

[73] A. V. Kolobov, J. Tominaga, P. Fons and T. Uruga, *Appl. Phys. Lett* 82, 382 (2003).

[74] S.-W. Nam, T.-Y. Lee, J.-S. Wi, D. Lee, H.-S. Lee, K.-B. Jin, M.-H. Lee, H.-M. Kim and K.-B. Kim, *J. Electrochem. Soc*. 154, (9), H844-H847 (2007).

[75] D. B. Williams, C. B. Carter, *Transmission Electron Microscopy - A Textbook for Materials Science* (Springer, 2009).

[76] G. Servalli, A 45nm generation Phase Change Memory technology, *Electron Devices Meeting (IEDM)*, IEEE International (2009).

[77] C. M. Osburn and D. W. Ormond*, J. Electrochem. Soc*. 119 (5), pp. 591-597 (1972).

[78] A. Redaelli, A. L. Lacaita, A. Benvenuti, A. Pirovano, A., Comprehensive numerical model for Phase-Change Memory simulations, *Simulation of Semiconductor Processes and Devices*, SISPAD (2005).

[79] H. K. Lyeo, D. G. Cahill, B. S. Lee, J. R. Abelson, M. H. Kwon, K. B. Kim, S. G. Bishop, B. K. Cheong, *Appl. Phys. Lett.* 89, 151904 (2006).

[80] C. Kim, D. Kang, Tae-Yon Lee, K. H. P. Kim, Y.-S. Kang, J. Lee, S.-W. Nam, K.-B. Kim, Y. Khang, Appl. Phys. Lett. 94, 193504 (2009).

[81] P. Zhou, Y. C. Shin, B. J. Choi, S. Choi, C. S. Hwang, Y. Y. Lin, H. B. Lv, X. J. Yan, T. A. Tang, L. Y. Chen, B. M. Chen, *Electrochem. Solid-State Lett.* 10 (9) H281-H283 (2007).

[82] S. O. Ryu, S. M. Yoon, K. J. Choi, N. Y. Lee, Y. S. Park, S. Y. Lee, B. G. Yu, J. B. Park, W. C. Shin, *J. Electrochem. Soc*. 153 (3), G234-G237 (2006).

[83] A. Padilla, G. W. Burr, K. Virwani, A. Debunne, C. T. Rettner, T. Topuria, P. M. Rice, B. Jackson, D. Dupouy, A. J. Kellock, R. M. Shelby, K. Gopalakrishnan, R. S. Shenoy, and B. N. Kurdi, Voltage polarity effects in GST-based Phase Change Memory: Physical origins and implications, *Electron Devices Meeting (IEDM)*, IEEE International (2010).

List of publications

- *Nucleation and grain growth in as deposited and ion implanted GeTe thin films,* **A.M. Mio**, E. Carria, G. D´Arrigo, S. Gibilisco, M. Miritello, M.G. Grimaldi, E. Rimini, Journal of Non-Crystalline Solids, 357, 2197–2201 (2011)
- *Crystallization of nanometer $Ge_2Sb_2Te_5$ amorphous regions embedded in the hexagonal close packed structure*, **A.M. Mio**, G. D'Arrigo, E. Carria, C. Bongiorno, S. Rossini, C. Spinella, M.G. Grimaldi, E. Rimini, *submitted*
- *Polymorphism of amorphous $Ge_2Sb_2Te_5$ probed by EXAFS and Raman spectroscopy,* E. Carria, **A.M. Mio**, S. Gibilisco, M. Miritello, F. D'Acapito, M. G. Grimaldi, E. Rimini, Electrochemical and Solid-State Letters, 14 (12), H480-H482 (2011)
- *Tuning the Crystallization Temperature of Amorphous $Ge_2Sb_2Te_5$ by O and Si Recoil Implantation* E. Carria, **A.M. Mio**, S. Gibilisco, M. Miritello, M.G. Grimaldi, E. Rimini, Electrochemical and Solid-State Letters, 14 (3), H124-H127 (2011)
- *Crystallization of ion amorphized $Ge_2Sb_2Te_5$ thin films in presence of cubic or hexagonal phase.* R. De Bastiani, E. Carria, S. Gibilisco, G. Nicotra, **A. Mio**, C. Bongiorno, E. Rimini, M.G. Grimaldi, C. Spinella. Journal Of Applied Physics, 107, 113521 (2010)
- *Local order and crystallization of laser quenched and ion implanted amorphous Ge_xTe_{1-x} thin films*. E. Carria, **A. Mio**, M. Miritello, S. Gibilisco, R. De Bastiani, A.R. Pennisi, C. Bongiorno, M.G. Grimaldi, E. Rimini. Electrochemical and Solid-State Letters, 13 (9), H317-H320 (2010)

Conferences

Italian Physical Society XCVII National Congress. L'Aquila, ITALIA, 26 - 30 September, 2011

- Nanostrutture amorfe di $Ge_2Sb_2Te_5$ inglobate in ambiente cristallino, **A.M. Mio**, G. D'Arrigo, E. Carria, C. Bongiorno, S. Rossini, A. Gotti, A. Pirovano, R. Bez, C. Spinella, M.G. Grimaldi, E. Rimini, *oral presentation*
- Impiantazione ionica di $Ge_2Sb_2Te_5$ depositato su cantilever di Si_3N_4, G. D'Arrigo, **A.M. Mio**, E. Carria, M. Miritello, M.G. Grimaldi, C. Spinella, E. Rimini, *oral presentation*

Material Research Society, Spring Meeting 2011. San Francisco, USA, 25-29 April 2011.

- Manipulation of amorphous $Ge_2Sb_2Te_5$ nano-structures in isolated and crystalline environment. **A.M. Mio**, G. D'Arrigo, E. Carria, C. Bongiorno, M. Miritello, C. Spinella, M. G. Grimaldi, E. Rimini, Symposium R, *oral presentation and proceeding,* Mater. Res. Soc. Symp. Proc. Vol. 1338, 1338-R06-08 (2011)
- Ion irradiation on phase change materials, E. Rimini, E. Carria, **A. M. Mio**, M. Miritello, S. Gibilisco, C.Bongiorno, G. D'Arrigo, M. G. Grimaldi, Symposium II, *oral presentation and proceeding*, Mater. Res. Soc. Symp. Proc. Vol. 1354, 1354-II06-06 (2011)
- Local order and crystallization of laser quenched and ion implanted amorphous $Ge_{1-x}Te_x$ thin films, E. Carria, R. De Bastiani, S. Gibilisco, **A. Mio**, M. Miritello, A. R. Pennisi, C. Bongiorno, M. G. Grimaldi, E. Rimini, *oral presentation and proceeding*, Mater. Res. Soc. Symp. Proc. Vol. 1251, 1251-H02-08 (2011)

European\ Phase Change and Ovonics Symposium 2010. Milano, Italia, 6-7 September 2010.

- Phase transitions in $Ge_{1-x}Te_x$ alloys. E. Carria, **A. Mio**, M. Miritello, S. Gibilisco, A. R. Pennisi, C. Bongiorno, M. G. Grimaldi, E. Rimini.

European\ Phase Change and Ovonics Symposium 2010, *poster session.*

Material Research Society, Spring Meeting 2010. San Francisco, USA, 5-8 April 2010.

- Local order and crystallization of laser quenched and ion implanted amorphous Ge1-xTex thin films, E. Carria, R. De Bastiani, S. Gibilisco, **A. Mio**, M. Miritello, A.R. Pennisi, C. Bongiorno, M.G. Grimaldi, E. Rimini, *oral presentation and proceeding*, Mater. Res. Soc. Symp. Proc. Vol. 1251-H02-08 (2010).
- Crystallization of ion amorphized $Ge_2Sb_2Te_5$ in nano-structured thin films. **A. Mio**, E. Carria, R. De Bastiani, M. Miritello, S. Gibilisco, C. Bongiorno, G. D’Arrigo, C. Spinella, M.G. Grimaldi, E. Rimini., *oral presentation and proceeding,* Mater. Res. Soc. Symp. Proc. Vol. 1251-H02-03 (2010).

European\ Phase Change and Ovonics Symposium 2009. Aachen, Germania, 6-8 September 2009

- Investigation of the structural order in amorphous GeTe-based alloys. R. De Bastiani, E.Carria, **A. Mio**, M.G. Grimaldi, C. Bongiorno, C. Spinella, G. D’Arrigo and E.Rimini. European\ Phase Change and Ovonics Symposium 2009, Proceedings.

Acknowledgements

Alla fine di questo lavoro di tesi desidero innanzitutto ringraziare la mia famiglia, ed in particolare i miei genitori. Possono sembrare dei ringraziamenti scontati, ma non lo sono. Mi hanno visto nascere, crescere, ma soprattutto mi hanno visto preparare e scrivere 5 lavori di tesi in 9 anni, sopportandomi ed aiutandomi nonostante le mie inevitabili negligenze: GRAZIE!

La mia più profonda gratitudine va al Prof. Emanuele Rimini, il quale ha seguito questo lavoro con una passione ed una costanza che mai avrei immaginato potesse essere elargita con tanta generosità. Egli è stato, prima ancora che una fonte inesauribile di idee e spunti, un esempio straordinario di dedizione alla ricerca e al proprio lavoro. Nonostante la quantità di nozioni, il metodo e l'esperienza che mi ha messo a disposizione, penso sia stata questa la vera lezione che mi ha impartito in questi anni e soprattutto per questo desidero ringraziarLo di cuore.

Un sincero grazie alla Prof.ssa Maria Grazia Grimaldi per aver seguito questo lavoro e per averlo continuamente migliorato, condividendo i Suoi suggerimenti e la Sua esperienza.

Un ringraziamento speciale al Dott. Giuseppe D'Arrigo che mi ha seguito giorno per giorno in questi tre anni, insegnandomi innumerevoli concetti di fisica e tecnica, mettendomi a disposizione il Suo laboratorio e sopportando il mio noto disordine. Grazie, perché le cose che mi ha insegnato in questi anni sono molte di più di quante abbia potuto scrivere in questo lavoro.

Un grazie sentito al Dott. Corrado Spinella, che oltre ad avermi consentito di svolgere il presente lavoro all'interno dei laboratori dell'Istituto per la Microelettronica e Microsistemi del Consiglio Nazionale per le Ricerche, ha contribuito significativamente alla comprensione ed alla realizzazione dei fenomeni osservati, condividendo essenziali spunti, modelli ed idee.

Desidero inoltre profondamente ringraziare il Dott. Salvo Lombardo, per aver letto con pazienza la prima bozza completa di questo lavoro, ed avermi suggerito numerosi miglioramenti formali e sostanziali.

Un ringraziamento di cuore a Corrado Bongiorno, per aver passato settimane e settimane (divise in turni da 4 a 8 ore circa) ad analizzare i campioni TEM, con la pazienza, la razionalità e la curiosità che lo contraddistingue. Grazie, soprattutto, per il tempo speso per mettermi a disposizione la Sua considerevole conoscenza ed esperienza circa la microscopia elettronica.

Un sincero grazie ad Egidio, con il quale ho condiviso questo periodo di studio sui calcogenuri, per tutte le discussioni, i chiarimenti, l'aiuto e la collaborazione scaturiti in questi anni. Il ringraziamento si estende naturalmente a Gabriella, con la quale abbiamo condiviso il laboratorio e gli insegnamenti del Dott. D'Arrigo.

Desidero quindi ringraziare l'intero staff dell' IMM-CNR di Catania, nella persona dei Ricercatori, Assegnisti, Tesisti, Tecnici e Amministrativi che mi hanno messo a disposizione la loro competenza e la loro strumentazione. Vorrei in particolare ringraziare la Dott.ssa Silvia Scalese, per le analisi SEM, e il Dott. Filippo Giannazzo, per le analisi AFM, eseguite sui campioni durante la messa a punto dei vari flow chart.

Desidero quindi particolarmente ringraziare Salvo Pannitteri per tutti gli utili suggerimenti sulla preparazione campioni e sulla parte tecnica del TEM. Un ringraziamento speciale sento inoltre di dover indirizzare a Salvo Di Franco per l'assistenza paziente in clean room e per gli attacchi in plasma.

Un grazie sentito quindi a tutto il personale del MATIS-IMM-CNR, con cui ho interagito durante questo periodo di studio. Un grazie speciale alla Dott.ssa Maria Miritello, per averci messo a disposizione lo sputter, insegnandoci numerose nozioni circa il suo utilizzo. Grazie di cuore alla Dott.ssa Simona Boninelli, che mi ha messo a disposizione il SEM per gli studi morfologici sui dispositivi programmati.

Grazie infinitamente al Prof. Andrea Lacaita, per aver seguito la parte di caratterizzazione elettrica di questi dispositivi prototipali ed ad Andrea Cattaneo per aver eseguito le misure presso il Politecnico di Milano. Un sincero ringraziamento ad entrambi, inoltre, per le proficue discussioni a riguardo, con le quali ho potuto apprendere una notevole quantità di nozioni a me nuove ed utilissime.

Grazie di cuore a i miei Amici, che non elenco qui perché sono tanti e potrei in questa sede dimenticarne facilmente qualcuno, ma che non si dimenticano di me e mi vengono a cercare nonostante le mie mancanze.

Il mio ringraziamento più caro va quindi a te, Claudia, che non mi hai fatto mai mancare il Tuo affetto, nonostante il mio essere frequentemente sovrappensiero e le innumerevoli serate passate davanti al PC.

Catania, 10 Dicembre 2011